

---

MODELLING CALCIUM SIGNALLING AND ITS  
COUPLING WITH MECHANICS

---



Abhishek Chakraborty  
School of Mathematics  
Cardiff University

September 2020

**A thesis submitted for the degree of**  
*Master of Philosophy*

# Abstract

Calcium ( $\text{Ca}^{2+}$ ) signalling is one of the most important mechanisms of information propagation in the body (M. J. Berridge et al., 2000). Recently, experiments have shown that the coupling between  $\text{Ca}^{2+}$  signalling and mechanical forces plays a crucial role in fertilisation, embryogenesis, wound healing, and cancer. However, this mechanochemical coupling is poorly understood and few mechanochemical models exist to date.

We first study the Atri et al. (1993) model - a nonlinear, excitable system of two ODEs, neglecting  $\text{Ca}^{2+}$  diffusion effects. As the  $\text{IP}_3$  concentration increases, this model exhibits action potentials and limit cycles ( $\text{Ca}^{2+}$  oscillations). Subsequently, we study the Atri model with  $\text{Ca}^{2+}$  diffusion, in one spatial dimension. This system consists of a reaction-diffusion PDE for  $\text{Ca}^{2+}$  and generates an interesting repertoire of behaviours – solitary waves and periodic wavetrains.

To study the mechanochemical coupling of  $\text{Ca}^{2+}$ , we begin with the mechanochemical model by Kaouri et al. (2019). The Atri model is coupled with a force balance equation for embryonic tissue, which is modelled as a linear, viscoelastic material. The mechanics equation includes a  $\text{Ca}^{2+}$ -dependent traction term. This has been modelled with a Hill function in Kaouri et al. (2019), reflecting the saturation effect that has been observed in some experiments (Christodoulou & Skourides, 2015). However, in other experiments (Ajduk et al., 2011), there is evidence that the actomyosin network in the cytosol solates at high  $\text{Ca}^{2+}$  levels. Hence, we model a traction term that rises and then falls with the  $\text{Ca}^{2+}$  level. Upon increasing the width of the traction function, we find that the frequency of contractions decreases whereas the frequency of  $\text{Ca}^{2+}$  oscillations remains unaltered. We then incorporate  $\text{Ca}^{2+}$  diffusion and study the system's behaviour in one spatial dimension.

Finally, we return to the Atri model and solve it on a disc, obtaining solitary waves and periodic wavetrains.

# Acknowledgements

First and foremost, I would like to thank my supervisor Dr. Katerina Kaouri who made all of this possible. From helping with my application process to polishing up my thesis, she has been with me every step of the way. As I was a newcomer to both mathematics and academic research, I can imagine that it must have been taxing to guide me and would like to thank her for her patience. Because of her guidance, I have been able to grow as a researcher.

I would like to thank my supervisor Prof. Tim Phillips for his guidance and wisdom. His advice greatly helped in shaping the scope and direction of the project and his suggestions allowed me improve the overall quality of this thesis. I am very grateful for his support.

I would like to express my gratitude towards my friends, Gautam and Pranav. My time at Cardiff wouldn't have been so enjoyable if it wasn't for them. I will miss our late night chats and long walks.

I would like to honour my parents who have stood by me through thick and thin. Their unconditional love and unwavering faith in me renders even me speechless at times. I will forever be in their debt.

And, finally, I would like to offer obeisance to Ma Kali, the Divine Mother of the Universe. It is Her blessing that helps me see the light in the darkest of times.

# Contents

<b>1</b>	<b>Introduction</b>	<b>1</b>
1.1	Calcium Signalling in Fertilisation and Embryogenesis . . . . .	1
1.2	Interplay of Calcium Signalling and Mechanics . . . . .	5
1.3	Mathematical Models of Calcium Signalling . . . . .	7
1.4	Project Aims . . . . .	12
1.5	Thesis Overview . . . . .	12
<b>2</b>	<b>The Atri model</b>	<b>14</b>
2.1	Atri model . . . . .	15
2.2	Model assumptions . . . . .	16
2.3	Nondimensionalising the model . . . . .	19
2.4	Linear stability analysis . . . . .	20
2.5	Simulations . . . . .	23
<b>3</b>	<b>The Atri model with diffusion (1D)</b>	<b>26</b>
3.1	The Atri model with diffusion . . . . .	27
3.2	Nondimensionalising the model . . . . .	28
3.3	Simulations . . . . .	29
<b>4</b>	<b>Calcium signalling and mechanics: a mechanochemical model</b>	<b>37</b>
4.1	A mechanochemical model based on the Atri model . . . . .	38
4.1.1	Force balance equation for a viscoelastic material . . . . .	39
4.1.2	Nondimensionalising the ODE model . . . . .	40
4.1.3	Modelling the Traction stress . . . . .	40
4.1.4	Linear stability analysis: The Hopf curve . . . . .	44
4.1.5	Hopf curves for various Traction terms . . . . .	45
4.2	Simulations . . . . .	48

<b>5</b>	<b>The Mechanochemical model with diffusion (1D)</b>	<b>56</b>
5.1	Adding $\text{Ca}^{2+}$ diffusion to the mechanochemical model . . . . .	56
5.2	Simulations . . . . .	57
<b>6</b>	<b>The Atri model on a disc (2D)</b>	<b>74</b>
6.1	Nondimensionalising the model . . . . .	75
6.2	Simulations . . . . .	75
<b>7</b>	<b>Summary, Conclusions and Future Work</b>	<b>89</b>
	<b>References</b>	<b>92</b>
	<b>A1 Model parameters</b>	<b>103</b>
	<b>A2 MATLAB codes</b>	<b>104</b>

# Chapter 1

## Introduction

### 1.1 Calcium Signalling in Fertilisation and Embryogenesis

Calcium ( $\text{Ca}^{2+}$ ) is a universal and versatile signal. It is the most important second messenger in the body and  $\text{Ca}^{2+}$  signalling is an indispensable method of information transfer within the human body (M. J. Berridge et al., 2000). In this project, we focus on the role of  $\text{Ca}^{2+}$  signalling in fertilization and embryogenesis, and its interplay with mechanical forces.

In a typical cell, the intracellular concentration of  $\text{Ca}^{2+}$  ( $\approx 100\text{nM}$ ) is kept relatively low with respect to the extracellular fluid by an approximate magnitude of 20000 (Clapham, 2007). Due to the extremely low intracellular  $\text{Ca}^{2+}$  concentration, the entry of minute quantities of  $\text{Ca}^{2+}$  ions from the Endoplasmic Reticulum (ER) - the major store of  $\text{Ca}^{2+}$  in the cell, or from the extracellular fluids cause rapid, distinctive and readily reversible changes in the concentration of these ions in the cytosol which manifest as oscillations and waves. This enables  $\text{Ca}^{2+}$  to serve as a potent intracellular signal, a secondary messenger, for various functions e.g. muscle contraction, blood clotting, wound healing, fertilization, embryogenesis and cancer (M. J. Berridge et al., 2000). Figure 1.1 depicts  $\text{Ca}^{2+}$  oscillations in various types of cells.

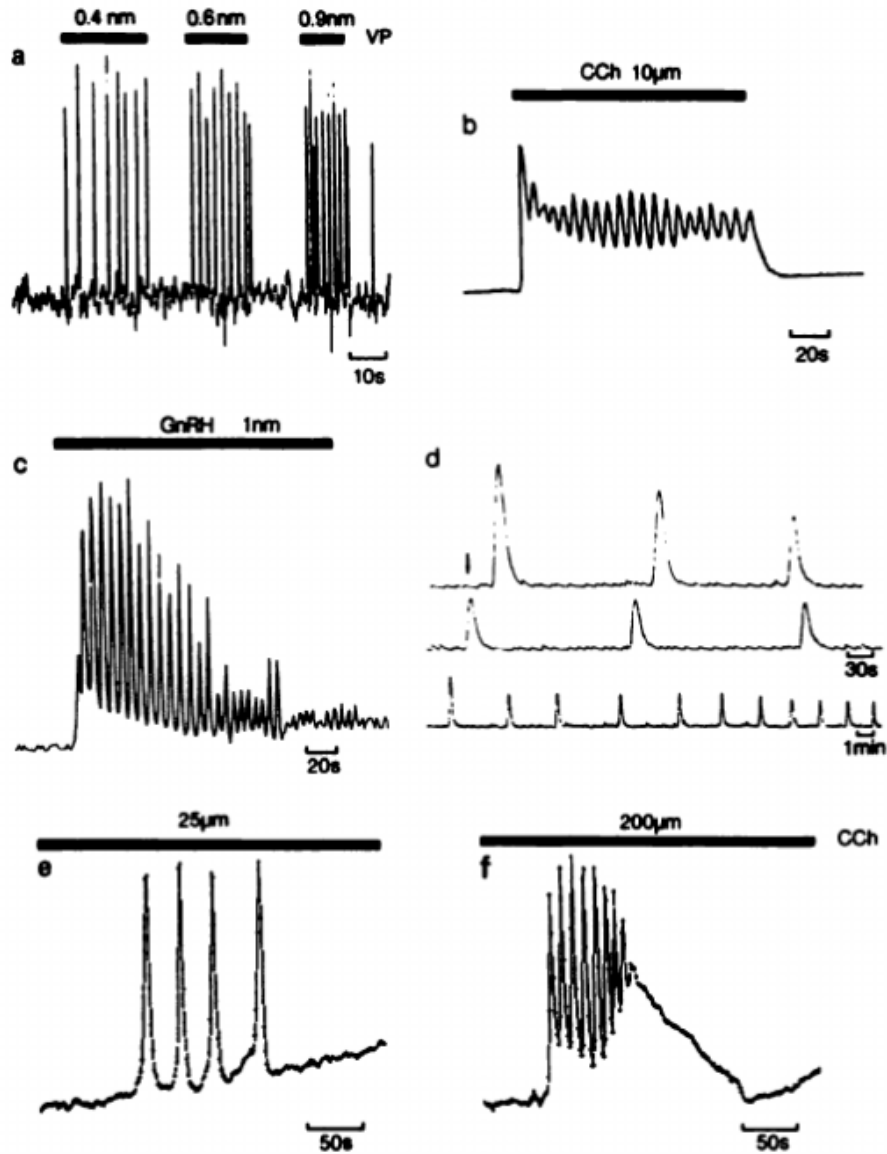


Figure 1.1:  $\text{Ca}^{2+}$  oscillations in different types of cells: (a) Hepatocyte, (b) Rat parotid gland cell, (c) Gonadotrope, (d) Hamster egg after fertilization, (e) and (f) Insulinoma cells. Source: (M. J. Berridge & Galione, 1988)

The  $\text{Ca}^{2+}$  signalling process is initiated when the cytosolic concentration of  $\text{Ca}^{2+}$  rises. When  $\text{Ca}^{2+}$  acts as the primary messenger, the process is triggered when  $\text{Ca}^{2+}$  enters the cell through plasma membrane ion channels. When  $\text{Ca}^{2+}$  acts as the secondary messenger, the cell is stimulated to release  $\text{Ca}^{2+}$  ions from intracellular stores e.g. the ER, when an agonist binds to a receptor on the plasma membrane (Clapham, 2007).

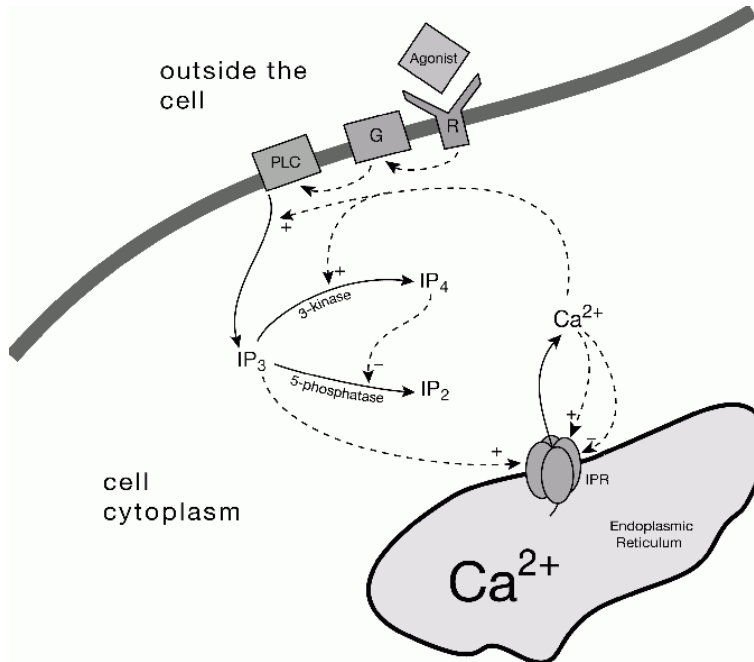


Figure 1.2: The PLC pathway for Ca<sup>2+</sup> signalling. Source: (Sneyd, 2007)  
R - Receptor, G - GPCR

The most common signalling pathway that leads to an increase in the concentration of cytoplasmic Ca<sup>2+</sup> is the phospholipase-C (PLC) pathway (Figure 1.2), which is activated as follows (Alberts et al., 2013):

1. Upon stimulation i.e. agonist-receptor binding, the receptor (located on the plasma membrane) activates the PLC enzyme via the G protein-coupled receptors (GPCR).
2. PLC hydrolyses the membrane phospholipid phosphatidylinositol 4,5-biphosphate (PIP<sub>2</sub>) to form the water soluble inositol 1,4,5-triphosphate (IP<sub>3</sub>), and lipid soluble diacylglycerol (DAG).
3. IP<sub>3</sub> diffuses to the ER and binds to an IP<sub>3</sub> receptor.
4. The IP<sub>3</sub> receptor (IPR) then activates and begins to serve as a channel to release Ca<sup>2+</sup> from the ER into the cytosol.

In most cell types, release of Ca<sup>2+</sup> through the IPR can stimulate the release of additional Ca<sup>2+</sup> from the ER, often by binding to the IPR and increasing its open probability. This leads to the autocatalytic release of Ca<sup>2+</sup> from the ER, in a process usually called Ca<sup>2+</sup>-induced Ca<sup>2+</sup> release, or CICR (Sneyd, 2007).

In all species that exhibit  $\text{Ca}^{2+}$  waves, the inositol 1,4,5-triphosphate receptor (IPR)/ $\text{Ca}^{2+}$  channel governs the mechanism of  $\text{Ca}^{2+}$  release from the ER. Since  $\text{Ca}^{2+}$  itself is an activator of the IPR (Furuichi et al., 1994), the rate of  $\text{IP}_3$ -induced  $\text{Ca}^{2+}$  release (IICR) was shown to be enhanced when intracellular  $\text{Ca}^{2+}$  concentration is within a certain range. However, if the  $\text{Ca}^{2+}$  concentration exceeds the upper bound of this range, the rate of IICR will be suppressed e.g. for smooth muscle cells, this value is between 100 nM (at rest state) and 300 nM (Iino & Endo, 1992). It is important to note this bell-shaped dependence of IICR on  $\text{Ca}^{2+}$  concentration (Mak et al., 1998).

The importance of  $\text{Ca}^{2+}$  signalling in fertilization and embryogenesis has been suspected for quite some time (Heilbrunn, 1928); however, experimental investigation gained traction from 1972 onward, when an ionophore antibiotic A23187 was demonstrated to behave as a freely mobile carrier of  $\text{Ca}^{2+}$  (Reed & Lardy, 1972). Employing this tool, subsequent experiments showed that an increase in  $\text{Ca}^{2+}$  was sufficient to induce many of the processes markedly associated with fertilization (Chambers et al., 1974; Steinhardt & Epel, 1974; Steinhardt et al., 1974). Indeed, in some cases of fertilization failure that might occur during Intra-Cytoplasmic Sperm Injection (ICSI) cycles, oocyte activation may be artificially facilitated by  $\text{Ca}^{2+}$  (Kashir et al., 2010).

Starting from the  $\text{Ca}^{2+}$  waves manifesting in the egg during fertilization (Deguchi et al., 2000),  $\text{Ca}^{2+}$  plays a vital role in every stage of embryonic development. In all animal species examined to date, intracellular  $\text{Ca}^{2+}$  rises dramatically at the time of fertilization (Stricker, 1999; Miyazaki, 2006). This serves as a crucial signal that marks the commencement of oocyte activation. The rise in  $\text{Ca}^{2+}$  is due to the release of  $\text{Ca}^{2+}$  from the ER. This rise in the level of intracellular  $\text{Ca}^{2+}$  concentration takes the form of a “ $\text{Ca}^{2+}$  wave” that originates at the site of sperm-egg fusion and propagates over the entirety of the egg.

Gilkey et al. (1978) obtained the first images of a  $\text{Ca}^{2+}$  wave that started from the sperm-egg fusion site and travelled across the *Medaka* egg (diameter  $\approx$  1mm) at an approximate velocity of  $10\mu\text{m}/\text{s}$ . Because the  $\text{Ca}^{2+}$  wave was unaffected by the extracellular concentration of  $\text{Ca}^{2+}$ , it was taken as an indication that the rise in the level of  $\text{Ca}^{2+}$  was only due to the discharge from the cell’s internal stores (Gilkey et al., 1978). Subsequent experiments have clearly demonstrated that the  $\text{Ca}^{2+}$  wave propagation in deuterostome animal eggs (echinodermata e.g. starfish and chordata e.g. vertebrate species) arises due to intracellular  $\text{Ca}^{2+}$  release (Stricker, 1999).

At the time of fertilization and during the initial stages of embryogenesis,  $\text{Ca}^{2+}$  signals primarily exert a chemical influence on the evolution of the embryo by triggering the release of, activating, or impeding the activity of chemical species within the egg. It has been reported that the amplitude and frequency of the  $\text{Ca}^{2+}$  oscillations at the time of fertilization

affect the processes occurring in the later stages of embryonic development. In a study involving fertilized eggs implanted in surrogate rabbit mothers, it was observed that the morphology of the developing embryos depended upon the stimulating  $\text{Ca}^{2+}$  wave patterns of the initial hours following fertilization (Swann & Ozil, 1994).

The importance of  $\text{Ca}^{2+}$  in the later stages of embryonic development is also well known and backed by empirical evidence -  $\text{Ca}^{2+}$  waves in convergent extension movements during gastrulation (Wallingford et al., 2001),  $\text{Ca}^{2+}$  transients regulating Neural Tube Closure (NTC) (Christodoulou & Skourides, 2015), morphological patterning in the brain (Sahu et al., 2017; Webb & Miller, 2007), and apical-basal cell thinning in the enveloping layer cells (Zhang et al., 2011) either in the form of  $\text{Ca}^{2+}$  waves or through Wnt/ $\text{Ca}^{2+}$  signalling (Christodoulou & Skourides, 2015; Wallingford et al., 2001; Herrgen et al., 2014; Hunter et al., 2014; Kühl, Sheldahl, Malbon, & Moon, 2000; Kühl, Sheldahl, Park, et al., 2000; Narciso et al., 2017; Slusarski, Corces, & Moon, 1997; Slusarski, Yang-Snyder, et al., 1997; Suzuki et al., 2017). Crucially, it was observed that pharmacological inhibition of  $\text{Ca}^{2+}$  led to defects in the embryo (Wallingford et al., 2001; Christodoulou & Skourides, 2015).

In particular, during the development of the central nervous system, cells undergo a dramatic shape change, called Apical Constriction (AC), which generates a mechanical force and triggers the neural plate to form a tubular structure during NTC. Tissue contractions play a crucial role in AC and are  $\text{Ca}^{2+}$ -driven (Christodoulou & Skourides, 2015). When NTC fails, it results in embryo malformations e.g. Spina Bifida, the second most commonly occurring embryo malformation in the world (NIH, 2019).

Throughout fertilization and embryogenesis,  $\text{Ca}^{2+}$  signals evoke mechanical responses in the cells and tissue. The propagation of  $\text{Ca}^{2+}$  waves evoke a mechanical response from the cell, which can lead to a change in cell shape (Wallingford et al., 2001; Ajduk et al., 2011; Christodoulou & Skourides, 2015). This influences morphogenesis and, ultimately, impacts organogenesis. This interplay of  $\text{Ca}^{2+}$  and cell mechanics will be discussed in the following section.

## 1.2 Interplay of Calcium Signalling and Mechanics

Investigating the biomechanics of fertilization and embryogenesis and its coupling with the cellular biochemical pathways is essential for elucidating many open questions. During embryogenesis (which we also address as morphogenesis), tissues are remodelled by coordinated cell rearrangements and migrations, and cell shape changes are driven by forces generated by cytoskeletal reorganization.  $\text{Ca}^{2+}$  transients “accrue” clearly and more intensely in tissues undergoing rearrangement (Markova & Lenne, 2012), it is, thus, of great interest and

importance to study the mechanical effects of  $\text{Ca}^{2+}$  signals.

During embryogenesis, internally generated forces produce changes in cell shape and behaviour, which can aggregate at the level of tens to hundreds of cells to produce macroscopic tissue movements or tissue rearrangements (Lecuit et al., 2011). Convergent extension is one example of such movement (Nikolopoulou et al., 2017). During convergent extension, the tissue narrows in one direction and elongates in the other. Another example is tissue invagination that takes place during gastrulation in flies and neural tube formation in vertebrates.

There is ample evidence to indicate that  $\text{Ca}^{2+}$  might play a role in driving these morphogenetic changes (Markova & Lenne, 2012). For instance, experimentally induced changes in intracellular  $\text{Ca}^{2+}$  concentration perturb the elongation of the egg chamber in *Drosophila* (He et al., 2010), convergent extension movements during gastrulation in *Xenopus* (Wallingford et al., 2001) and zebrafish (Lam et al., 2009), epiboly progression in zebrafish (Cheng et al., 2004; Popgeorgiev et al., 2011) and newt (Takano et al., 2011), cell rearrangements during somitogenesis in zebrafish (Leung et al., 2009) and chicken (Chernoff & Hilfer, 1982), tissue folding during sea urchin gastrulation (M. C. Lane et al., 1993) and neural fold formation in *Xenopus* (Moran & Rice, 1976).

In many experiments actomyosin-based contractions have been documented in response to  $\text{Ca}^{2+}$  release in both embryonic and cultured cells (Christodoulou & Skourides, 2015; Herrgen et al., 2014; Hunter et al., 2014; Suzuki et al., 2017; Wallingford et al., 2001) and it has become clear that  $\text{Ca}^{2+}$  is responsible for contractions in both muscle and non-muscle cells, albeit through different mechanisms (Cooper et al., 2000). In striated muscle cells, cell contraction is mediated by the binding of  $\text{Ca}^{2+}$  to troponin but in non-muscle cells (and in smooth muscle cells), contraction is mediated by phosphorylation of the regulatory light chain of myosin. This phosphorylation promotes the assembly of myosin into filaments, and it increases myosin activity. Myosin light-chain kinase (MLCK), which is responsible for this phosphorylation, is itself regulated by calmodulin, a well-characterized and ubiquitously expressed protein regulated by  $\text{Ca}^{2+}$  (Scholey et al., 1980). Elevated cytosolic  $\text{Ca}^{2+}$  promotes binding of calmodulin to MLCK, resulting in its activation, subsequent phosphorylation of the myosin regulatory light chain and then contraction.

In some tissues, these contractions give rise to well defined changes in cell shape. One such example is Apical Constriction (AC), an intensively studied morphogenetic process central to embryonic development in both vertebrates and invertebrates (Vijayraghavan & Davidson, 2017). In AC, the apical surface of an epithelial cell constricts, leading to dramatic changes in cell shape. Such shape changes drive epithelial sheet bending and invagination, and are indispensable for tissue and organ morphogenesis including gastrulation in *C. elegans*

and *Drosophila* and vertebrate neural tube formation (Christodoulou & Skourides, 2015; Rohrschneider & Nance, 2009; Sawyer et al., 2010). So, it can be concluded that cytosolic  $\text{Ca}^{2+}$  elevation is a ubiquitous signal for cell contraction which manifests in various ways (Cooper et al., 2000).

On the other hand, the ability of cells to sense and respond to forces by elevating their cytosolic  $\text{Ca}^{2+}$  concentration is well established. Mechanically stimulated  $\text{Ca}^{2+}$  waves have been observed propagating through ciliated tracheal epithelial cells (M. J. Sanderson et al., 1990, 1988; M. Sanderson & Sleight, 1981), rat brain glial cells (Charles et al., 1993, 1991, 1992), keratinocytes (Tsutsumi et al., 2009), developing epithelial cells in *Drosophila* wing discs (Narciso et al., 2017) and many other cell types (Bereiter-Hahn, 2005; Tsutsumi et al., 2009; Yang et al., 2009; Young et al., 1999). Furthermore, Wallingford et al. (2001) reported dramatic intercellular  $\text{Ca}^{2+}$  waves in cells undergoing convergent extension in explants of gastrulating *Xenopus* embryos, which were often accompanied by a wave of contraction within the tissue. Thus, different types of mechanical stimuli, from shear stress to direct mechanical stimulation, can elicit  $\text{Ca}^{2+}$  elevation (although the sensing mechanism may differ in each case). Therefore, since mechanical stimulation elicits  $\text{Ca}^{2+}$  release and  $\text{Ca}^{2+}$  elicits contractions, which are sensed as mechanical stimuli by the cell, it can be inferred that there must exist a two-way mechanochemical feedback between  $\text{Ca}^{2+}$  and cell contraction.

### 1.3 Mathematical Models of Calcium Signalling

The non-linear  $\text{Ca}^{2+}$  oscillations and waves appear over diverse timescales and lengthscales and pose many interesting mathematical questions. Furthermore,  $\text{Ca}^{2+}$  signalling is an inherently stochastic process and this makes the analysis of  $\text{Ca}^{2+}$  signals even more complicated. A multitude of deterministic and stochastic  $\text{Ca}^{2+}$  signalling models have been presented in the literature, for various cell types and at various scales (Falcke, 2003; Keener & Sneyd, 2009; Dupont et al., 2016). While designing mathematical models of  $\text{Ca}^{2+}$  oscillations, there are two key points to focus on (Sneyd, 2007):

- Although the exact mechanisms that govern  $\text{Ca}^{2+}$  oscillations might differ from one cell type to another, there exist many similarities between the cell types so generalizations can be made while constructing the models.
- While constructing a model, the goal shouldn't be to simply write a system of equations that mimic the empirical data, but rather to reveal new information about the cellular physiology or predict novel behaviour. The aim is to go beyond the data.

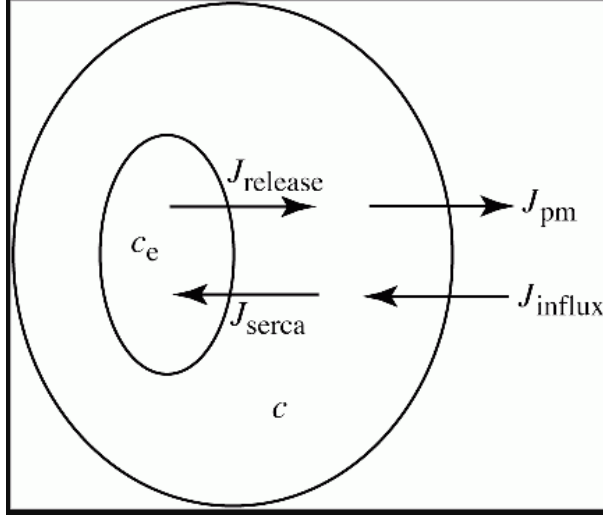


Figure 1.3: A schematic diagram for  $\text{Ca}^{2+}$  dynamics. Source: (Sneyd, 2007)

A typical  $\text{Ca}^{2+}$  dynamics schematic (Figure 1.3) describes the various  $\text{Ca}^{2+}$  fluxes into and from the cytoplasm. Using the conservation of  $\text{Ca}^{2+}$ , a simple model could be constructed as follows (Sneyd, 2007):

$$\frac{dc}{dt} = J_{\text{release}} - J_{\text{serca}} + J_{\text{influx}} - J_{\text{pm}} \quad (1.1)$$

$$\frac{dc_e}{dt} = \gamma(J_{\text{serca}} - J_{\text{release}}) \quad (1.2)$$

where  $c$  denotes the cytosolic  $\text{Ca}^{2+}$  concentration and  $c_e$  denotes the  $\text{Ca}^{2+}$  concentration in the ER. In these equations,  $J_{\text{release}}$  and  $J_{\text{serca}}$  denote  $\text{Ca}^{2+}$  flow from the ER to the cytosol and  $\text{Ca}^{2+}$  flow from the cytosol to the ER, respectively.  $J_{\text{pm}}$  and  $J_{\text{influx}}$  denote  $\text{Ca}^{2+}$  outflow from and inflow to cytosol across the plasma membrane, respectively, and  $\gamma$  denotes the ratio of the cytoplasmic volume to the ER volume.

The pair of equations (1.1) and (1.2) simply equate the temporal rates of change of  $c$  and  $c_e$  to the inflow and outflow of cytosolic  $\text{Ca}^{2+}$  and  $\text{Ca}^{2+}$  in the ER, respectively. Additional  $\text{Ca}^{2+}$  fluxes such as mitochondrial and buffer fluxes can be added in the same manner. Also, the conservation equations for  $c$  and  $c_e$  can be coupled to other equations that describe, for example, the cytosolic  $\text{IP}_3$  concentration, the fraction of active  $\text{IP}_3$  receptors on the ER, and the states of the ATPase pumps or  $\text{Ca}^{2+}$  buffers (Atri et al., 1993; Goldbeter et al., 1990; De Young & Keizer, 1992; Dupont et al., 1991).

In some cell types,  $\text{Ca}^{2+}$  oscillations occur practically uniformly across the cell i.e. at any time, measurement of the  $\text{Ca}^{2+}$  concentration at any point of the cell would yield the same

value (Sneyd, 2007). More often, however, the  $\text{Ca}^{2+}$  signal takes the form of a wave moving across the cell. To account for  $\text{Ca}^{2+}$  diffusion, the model must include a diffusion term. It is frequently assumed that  $\text{Ca}^{2+}$  diffuses with constant diffusion coefficient,  $D_c$ , and that the cellular cytoplasm is isotropic and homogeneous.

Adding the diffusion term to (1.1), the resulting reaction-diffusion equation for  $\text{Ca}^{2+}$  is

$$\frac{\partial c}{\partial t} = D_c \nabla^2 c + J_{\text{release}} - J_{\text{serca}}. \quad (1.3)$$

In this case, the fluxes  $J_{\text{pm}}$  and  $J_{\text{influx}}$  are omitted (Sneyd, 2007).

Before starting our analysis of  $\text{Ca}^{2+}$  signalling models, we summarize some of the works that shaped the field.

The Goldbeter model (Goldbeter et al., 1990) is based on CICR, from intracellular stores, and shows how sustained oscillations of cytosolic  $\text{Ca}^{2+}$  may arise as a result of a rise in  $\text{IP}_3$ , triggered by external stimulation. The model contains only two variables (concentrations of free  $\text{Ca}^{2+}$  in the cytosol and in the ER) and predicts the occurrence of periodic  $\text{Ca}^{2+}$  spikes in the absence of  $\text{IP}_3$  oscillations, indicating that repetitive  $\text{Ca}^{2+}$  spikes do not necessarily require the concomitant, periodic variation of  $\text{IP}_3$  and can be induced by external stimulation.

The model developed by Atri et al. (1993) expresses oscillations of free cytosolic  $\text{Ca}^{2+}$  and is based on  $\text{Ca}^{2+}$  release via the  $\text{IP}_3$  receptor/ $\text{Ca}^{2+}$  channel. Taking into account experimental evidence, the model encapsulates the fact that cytosolic free  $\text{Ca}^{2+}$  modulates the  $\text{IP}_3$  receptors in a biphasic manner -  $\text{Ca}^{2+}$  release is inhibited by low and high  $\text{Ca}^{2+}$  concentrations and facilitated by intermediate  $\text{Ca}^{2+}$  concentration, and that channel inactivation occurs on a slower time scale than activation. The model produces  $\text{Ca}^{2+}$  oscillations for a constant value of  $\text{IP}_3$  concentration and reproduces a number of crucial experiments (Lechleiter & Clapham, 1992; Finch et al., 1991; Parker & Ivorra, 1990; Iino & Endo, 1992; Girard & Clapham, 1993). The model produces circular, planar, and spiral waves of  $\text{Ca}^{2+}$ . The model is

$$\frac{\partial c}{\partial t} = D_c \nabla^2 c + J_{\text{channel}} - J_{\text{pump}} + J_{\text{leak}}, \quad (1.4)$$

$$\tau_h \frac{dh}{dt} = \frac{k_2^2}{k_2^2 + c^2} - h, \quad (1.5)$$

where

$$J_{\text{channel}} = k_{\text{flux}} \mu(p) h \frac{bk_1 + c}{k_1 + c}, \quad J_{\text{pump}} = \frac{\gamma c}{k_\gamma + c}, \quad J_{\text{leak}} = \beta.$$

In Equations (1.4) and (1.5), the variables  $c$  and  $h$  represent the cytosolic  $\text{Ca}^{2+}$  concentration and the fraction of  $\text{IP}_3$  receptors that have not been inactivated within the *Xenopus laevis* oocyte. Note that the parameter  $\mu$  (fraction of  $\text{IP}_3$  receptors with bound  $\text{IP}_3$ ) is taken to be a function of  $p$  (cytosolic  $\text{IP}_3$  concentration). For the models studied in this project,  $\mu$  will be taken as a *bifurcation parameter*.

The Atri model is an example of a gating model - where the open probability of the ‘gate’ (in this case, the IPR channel) is a function of the gating variables. It is assumed that the transition times of these variables are fast enough to be considered at quasi-steady state. The Atri model will be discussed in greater depth in Chapter 2 and used throughout this work.

The De Young-Keizer model (De Young & Keizer, 1992) investigated the properties of the  $\text{IP}_3$  receptor/ $\text{Ca}^{2+}$  channel. The rate constants in the equations were tuned to fit kinetic and equilibrium data and it was found that the model successfully reproduced a variety of *in vivo* and *in vitro* experiments (M. Berridge, 1989; Mouillac et al., 1990; Smrcka et al., 1991; Taylor & Exton, 1987). The model incorporates a positive-feedback mechanism of  $\text{Ca}^{2+}$  on  $\text{IP}_3$  production by the phospholipase-C (PLC) pathway. This was noted to enrich the properties of the oscillations and led to  $\text{Ca}^{2+}$  oscillations accompanied by  $\text{IP}_3$  oscillations.

The Li-Rinzel model (Li & Rinzel, 1994) reduces the nine-variable De Young-Keizer model to a two-variable system. The variables represent cytosolic  $\text{Ca}^{2+}$  concentration and the percentage of  $\text{IP}_3$  receptors that have not been inactivated, respectively. This was achieved by using the *method of multiple scales* to solve the equations of the De Young-Keizer model on a succession of faster time scales to reduce it to a 2D system. The reduced system is analogous in form to the Hodgkin-Huxley equations for plasma membrane electrical excitability (Hodgkin & Huxley, 1952). Like the Atri model, the Li-Rinzel model is also a gating model.

We have briefly reviewed some seminal models of  $\text{Ca}^{2+}$  signalling above. In this work, we are interested in the interplay of  $\text{Ca}^{2+}$  signalling and mechanics, so we also summarize some mechanochemical models for  $\text{Ca}^{2+}$  signalling below.

The model developed by Kaouri et al. builds on early models that couple  $\text{Ca}^{2+}$  dynamics to the cell mechanics and replaces the hypothetical bistable  $\text{Ca}^{2+}$  release (J. Murray, 2001; J. D. Murray et al., 1988; Murray & Oster, 1984; Oster & Odell, 1984) with the modern, experimentally validated  $\text{Ca}^{2+}$  dynamics of the Atri model. Embryonic cells and tissue are assumed to be a linear, viscoelastic material. The  $\text{Ca}^{2+}$ -induced contraction stress is modelled with a Hill function, assuming that the mechanical responsiveness of the cytosol to  $\text{Ca}^{2+}$  saturates for high  $\text{Ca}^{2+}$  levels. A key feature of this model is that it demonstrates that mechanical effects, which are frequently ignored, can significantly affect  $\text{Ca}^{2+}$  signalling i.e. mechanical effects can cause  $\text{Ca}^{2+}$  oscillations to vanish (implying information loss),

resulting in the failure of key processes during embryogenesis, like AC (Kaouri et al., 2019).

In 2015, Narciso et al. studied the relationship between the spatiotemporal properties of  $\text{Ca}^{2+}$  transients and the mechanical characteristics of the underlying tissues (C. Narciso et al., 2015). They adapted the Atri model, which was originally developed for *intracellular*  $\text{Ca}^{2+}$  dynamics, to study *intercellular*  $\text{Ca}^{2+}$  dynamics. This was made possible by incorporating the passage of  $\text{Ca}^{2+}$  and  $\text{IP}_3$  into neighbouring cells via gap junctions, as in Wilkins & Sneyd (1998). The diffusion coefficient  $D_c$  (see Equation (1.4)) was replaced by a diffusion coefficient tensor, derived using homogenization techniques. The results showed that intercellular  $\text{Ca}^{2+}$  transients follow lines of mechanical tension and, in doing so, reflect the mechanical state of the underlying tissue.

In a study conducted on *Drosophila* wing discs, Narciso et al. (2017) demonstrated that the release of mechanical loading, rather than its initial application, is sufficient to trigger intercellular  $\text{Ca}^{2+}$  waves. The mechanically induced  $\text{Ca}^{2+}$  waves rely on IPR-mediated CICR and propagation through gap junctions. They conclude that the intercellular  $\text{Ca}^{2+}$  waves in developing epithelia may be a consequence of stress dissipation during organ growth.

In their study of *Xenopus* neural tube formation, Suzuki et al. (2017) employed a vertex model, a mathematical framework appropriate for describing multicellular tissue dynamics. In contrast to the continuum-based models discussed thus far, vertex models are cell-based models, where each cell is represented by a polyhedron (Fletcher et al., 2014). This polyhedron includes vertices and edges that are shared by neighbouring polyhedra and these structures comprise a network that represents the entire shape of the aggregate (Okuda et al., 2013). Suzuki et al. (2017) assumed that the  $\text{Ca}^{2+}$  transients occurring in each cell modify the line tension of the cellular edges which, in turn, decreases the apical surface area of the individual cells and of the tissue.

Suzuki et al. (2017) showed that there are two types of  $\text{Ca}^{2+}$  concentration changes, a single-cell and multicellular wave-like fluctuation, that drive NTC in the developing neural plate. They found that the fluctuations affecting individual cells have a greater impact on the rate at which AC and NTC occur, compared to the fluctuations at the multicellular level. Their results were found to be in agreement with the *in vivo* experimental data.

It is important to note that all models described above are deterministic. Since  $\text{Ca}^{2+}$  signalling is an inherently stochastic process, there exists a separate class of models that take into account the effect of stochastic processes like the opening and closing of  $\text{IP}_3$  receptors and ‘*stretch-sensitive calcium channels*’ (SSCCs) located on the plasma membrane. However, stochastic models are outside the scope of this project.

## 1.4 Project Aims

In this thesis, we aim to study a series of  $\text{Ca}^{2+}$  signalling models related to the Atri model. The primary aim of this project is to investigate this interplay of  $\text{Ca}^{2+}$  and cell mechanics in fertilization and embryogenesis. The goal is to simulate the cellular mechanics and its coupling with  $\text{Ca}^{2+}$  waves.

This will be achieved by analysing the behaviour of existing mechanochemical models of  $\text{Ca}^{2+}$  signalling, specifically the model developed by Kaouri et al. (2019), where the *embryonic epithelial cells and tissue* under study are assumed to be a viscoelastic continuum and  $\text{Ca}^{2+}$  dynamics are governed by the Atri model.

We simulate the Kaouri et al. (2019) model for traction stress terms of different shapes and study how the shape of the traction term affects  $\text{Ca}^{2+}$  oscillations and cell and tissue contractions. We then add  $\text{Ca}^{2+}$  diffusion and simulate the model for the same traction terms to study how the shape of the traction term affects  $\text{Ca}^{2+}$  waves and cell and tissue contractions over a one dimensional geometry.

Finally, because cells are complex three-dimensional structures, we investigate whether the qualitative behaviour displayed in simpler geometries can provide insights and predict behaviour over more complex geometries. So, we simulate the Atri model over a two dimensional geometry and compare the behaviour with that of the corresponding one dimensional model.

The ultimate aim of this project is to obtain a continuum-based model that proves to be in reasonable agreement when tested with experimental data in the future.

## 1.5 Thesis Overview

This thesis follows an incremental approach, with each chapter presenting the analysis of a single mathematical model that builds upon the model discussed in previous chapters.

Chapter 1 starts with a literature review, summarising key developments in the  $\text{Ca}^{2+}$  signalling field with emphasis on the interplay of  $\text{Ca}^{2+}$  signalling and mechanics in fertilization and embryogenesis. The review introduces the involved biological processes and terminology, presents some important experiments, and then summarizes a few key mathematical models which have been used to study these processes. In Chapter 2, we present and analyse the Atri model, neglecting  $\text{Ca}^{2+}$  diffusion effects. In Chapter 3, we incorporate  $\text{Ca}^{2+}$  diffusion effects in the Atri model, in one spatial dimension, and study the resulting PDE system. In Chapter 4, we study the mechanochemical model of Kaouri et al. (2019) which combines the  $\text{Ca}^{2+}$  dynamics of the Atri ODE model with the mechanics of a linear, viscoelastic material

under the assumption that the traction stress saturates at high enough  $\text{Ca}^{2+}$  levels. We also solve the latter model for a different experimental hypothesis - we assume that the traction stress initially increases with  $\text{Ca}^{2+}$  but, as  $\text{Ca}^{2+}$  rises further, the contractile stress decreases to zero. In Chapter 5, we incorporate  $\text{Ca}^{2+}$  diffusion effects in one spatial dimension and compare the system's behaviour for the two traction stress terms. In Chapter 6, we solve the Atri model in two spatial dimensions (over a disc), using radially symmetric initial conditions, and compare the behaviour of the system with the corresponding one dimensional model in Chapter 3. Finally, in Chapter 7, we summarize our findings and conclusions and suggest potential avenues for further work.

# Chapter 2

## The Atri model

There exist many models for  $\text{Ca}^{2+}$  signalling that are based on the  $\text{Ca}^{2+}$ -induced  $\text{Ca}^{2+}$  release (CICR) process, and they can be classified as Class I or Class II models (Dupont et al., 2016) based on the nature of the coupling between  $\text{IP}_3$  and  $\text{Ca}^{2+}$  (Sneyd et al., 2006). In all Class I models,  $\text{IP}_3$  is a control parameter and oscillations can be sustained for constant  $\text{IP}_3$  concentration. The model developed by Atri et al. (1993) is a prominent Class I model that has been validated by experimental findings (Estrada et al., 2016).

Estrada et al. (2016) used non-linear frequency analysis and non-linear amplitude analysis to compare eight  $\text{Ca}^{2+}$  signalling models against experimental data. The study examined the models of Meyer-Stryer (Meyer & Stryer, 1988), Goldbeter-Dupont-Berridge (Goldbeter et al., 1990), Sneyd-LeBeau (Sneyd et al., 2000), Atri et al (Atri et al., 1993) (Sneyd et al., 2006), and Li-Rinzel (Li & Rinzel, 1994) (Sneyd et al., 2006). The Class I Atri model and the Class I Li-Rinzel model not only displayed close agreement with experiments, but were also able to reproduce unexpected behaviour (Estrada et al., 2016).

This project will proceed with the Class I Atri model since its mathematical structure allows for a semi-analytical study of the mechanochemical models and affords easy identification of the parameter range sustaining  $\text{Ca}^{2+}$  oscillations.

It is to be noted that, in reality, the cellular substrate under study is not a smooth medium, since the cell organelles that inhabit the cytosol are dispersed throughout it irregularly. This dearth of homogeneity introduces a high degree of complexity, therefore, modellers incorporate certain assumptions into their models for the sake of simplicity. This allows the study to focus on the phenomenon of interest. Accordingly, the models in this project will assume the underlying tissue to be isotropic and homogeneous.

## 2.1 Atri model

The model developed by Atri et al. (1993) models cytosolic free  $\text{Ca}^{2+}$  oscillations in the *Xenopus laevis* oocyte. It is based on  $\text{Ca}^{2+}$  release from a single intracellular  $\text{Ca}^{2+}$  pool via the IPR channel. The model operates on experimental evidence that the cytosolic  $\text{Ca}^{2+}$  concentration modulates the IPRs in a biphasic manner, with  $\text{Ca}^{2+}$  release inhibited by low and high  $\text{Ca}^{2+}$  and facilitated by intermediate  $\text{Ca}^{2+}$  levels.

When an agonist binds to a receptor on the plasma membrane (see Figure 1.2), it triggers the production of  $\text{IP}_3$  via the PLC pathway.  $\text{IP}_3$  can then bind to the IPRs of an internal  $\text{Ca}^{2+}$  pool to release  $\text{Ca}^{2+}$  from this pool. The concentration of cytosolic  $\text{Ca}^{2+}$  can then either facilitate or inhibit further  $\text{Ca}^{2+}$  release (depending on which IPR  $\text{Ca}^{2+}$  binding domain it activates).  $\text{Ca}^{2+}$  can also be expelled from the cytosol through reabsorption by the pool or by pumping to the extracellular medium (Atri et al., 1993). The model is as follows:

$$\frac{dc}{dt} = J_{\text{channel}}(c, h, p) - J_{\text{pump}}(c) + J_{\text{leak}}, \quad (2.1)$$

$$\tau_h \frac{dh}{dt} = h_{\infty}(c) - h, \quad (2.2)$$

where

$$J_{\text{channel}}(c, h, p) = k_{\text{flux}} \mu(p) h \frac{bk_1 + c}{k_1 + c}, \quad J_{\text{pump}}(c) = \frac{\gamma c}{k_{\gamma} + c}, \quad J_{\text{leak}} = \beta,$$

and

$$h_{\infty}(c) = \frac{k_2^2}{k_2^2 + c^2}, \quad \mu(p) = \mu_0 + \frac{\mu_1 p}{k_{\mu} + p}.$$

Equations (2.1) and (2.2) describe  $\text{Ca}^{2+}$  dynamics in the *Xenopus* oocyte. The variables  $c$  and  $p$  represent the cytosolic  $\text{Ca}^{2+}$  and  $\text{IP}_3$  concentrations, respectively, and  $h$  is a dimensionless variable denoting the proportion of IPRs that have not been inactivated.

The function  $J_{\text{channel}}$  represents  $\text{Ca}^{2+}$  flux through the IPR,  $J_{\text{pump}}$  represents the  $\text{Ca}^{2+}$  being pumped out of the cytosol, and  $J_{\text{leak}}$  represents  $\text{Ca}^{2+}$  flux due to  $\text{Ca}^{2+}$  leaking into the cytosol from outside the cell. The function  $h_{\infty}$  represents the steady state of  $h$  as a function of  $c$ , and  $\mu(p)$  is the proportion of IPRs with bound  $\text{IP}_3$ .

Since  $\text{Ca}^{2+}$  oscillations occur at constant  $\text{IP}_3$  concentration,  $\text{IP}_3$  dynamics can be ignored i.e.  $p$  is not treated as a dynamic variable (Atri et al., 1993). The parameter  $\mu$  can be treated as a constant, to be held at any desired value between 0 and 1 i.e.  $\mu$  is treated as a bifurcation parameter.  $\text{IP}_3$  dynamics are of greater significance when considering the

diffusion of  $\text{Ca}^{2+}$  waves. However, the diffusion models in this project (Chapters 3, 5 & 6) will neglect  $\text{IP}_3$  dynamics to more clearly understand the coupling between  $\text{Ca}^{2+}$  dynamics and cellular mechanics.

A key feature of the model is the separation of the time scales of  $\text{Ca}^{2+}$ -dependent activation and inactivation of the IPR channel, with inactivation occurring more slowly than activation. This is supported by the work of Finch et al. (1991) who show that cytosolic  $\text{Ca}^{2+}$  rapidly activates  $\text{IP}_3$ -induced  $\text{Ca}^{2+}$  release but inactivates more slowly. Therefore, choosing a value of  $\tau_h > 1s$  accelerates the rate of activation compared to inactivation. Channel activation by  $\text{Ca}^{2+}$  is assumed to be instantaneous.

## 2.2 Model assumptions

### The single channel model

While deriving their model, Atri et al. made the following assumptions regarding  $\text{IP}_3$  (the full derivation can be found in the Appendix of Atri et al. (1993)):

1. The IPR is comprised of three independent binding domains - a single domain may correspond to multiple binding sites.
2. One  $\text{IP}_3$  binds to domain 1, one  $\text{Ca}^{2+}$  binds to domain 2, but two  $\text{Ca}^{2+}$  bind cooperatively to domain 3.
3. The IPR will conduct  $\text{Ca}^{2+}$  current only if domains 1 and 2 are active and domain 3 is inactive. Thus, activation of domains 1 and 2 increases  $\text{Ca}^{2+}$  flux but activation of domain 3 decreases it. Since,  $\text{Ca}^{2+}$  can bind to both domains, 2 and 3, it can either increase or decrease  $\text{Ca}^{2+}$  flux depending on the binding domain.
4. Even when  $c$  and  $p$  are zero, there still exists a nonzero probability that domains 1 and 2 will spontaneously activate. This can be approximated by assuming a basal current through the IPR.
5. The net  $\text{Ca}^{2+}$  flux from the internal store into the cytoplasm is regulated by the number of open channels.

Based on these assumptions, it can be shown that the open probability of an individual channel is given by  $p_1 p_2 p_3$ , where  $p_1$  and  $p_2$  are the probabilities that domains 1 and 2 are

activated, and  $p_3$  is the probability that domain 3 is inactivated. Thus, for a sample of  $N$  channels, the total steady state  $\text{Ca}^{2+}$  current through the IPRs is given by

$$I = Nip_1p_2p_3, \quad (2.3)$$

where  $i$  is the  $\text{Ca}^{2+}$  current through a single open channel. By assuming constant channel volume,  $U$ , the  $\text{Ca}^{2+}$  current can be converted to a concentration flux,  $J_{channel}$ , where

$$J_{channel} = \frac{I}{2\mathcal{F}U}, \quad (2.4)$$

where  $\mathcal{F}$  is Faraday's constant. Finally, we express  $k_{flux} = Ni/(2\mathcal{F}U)$  to get

$$J_{channel} = k_{flux}p_1p_2p_3, \quad (2.5)$$

The probabilities  $p_1$ ,  $p_2$ , and  $p_3$  are modelled as functions of  $c$  and  $p$  by assuming cooperative kinetics with Hill coefficients of 1, 1, and 2, respectively:

$$p_1 = \mu_0 + \frac{\mu_1 p}{k_\mu + p} \quad (2.6)$$

$$p_2 = b + \frac{V_1 c}{k_1 + c} \quad (2.7)$$

$$p_3 = 1 - \frac{c^2}{k_2^2 + c^2} \quad (2.8)$$

where  $\mu_0$  and  $\mu_1$  are chosen such that when  $p$  is low,  $c$  is low and nonoscillatory and when  $p$  is high,  $c$  is elevated and nonoscillatory,  $b$  denotes the proportion of IPRs that have domain 2 spontaneously activated in the absence of bound  $\text{Ca}^{2+}$  i.e. it represents the basal current through the channel, and  $V_1$  is the proportion of IPRs that are activated (at domain 2) by bound  $\text{Ca}^{2+}$ . Note that  $b + V_1 = 1$ . The parameters  $b, V_1, k_1$  and  $k_2$  were determined by fitting to the data of Parys et al. (1992). The full list of model parameters can be found in Appendix A1 (Table A1.1), the values are the same as those used in Atri et al. (1993). Finally, we obtain the following expression at steady state

$$J_{channel} = k_{flux} \left( \mu_0 + \frac{\mu_1 p}{k_\mu + p} \right) \left( b + \frac{V_1 c}{k_1 + c} \right) \left( 1 - \frac{c^2}{k_2^2 + c^2} \right) \quad (2.9)$$

where  $\mu(p) = p_1 = \mu_0 + \frac{\mu_1 p}{k_\mu + p}$  is the bifurcation parameter.

## Dynamic behaviour of the channel

Equation (2.9) expresses the steady flux through an IPR channel for a fixed value of  $c$ . However, it is of vital importance to consider the case where  $c$  is variable. This dynamic behaviour is a crucial component of the overall  $\text{Ca}^{2+}$  response. The results of Finch et al. (1991) imply that an abrupt increase in  $c$  causes the IPR channel to activate quickly and then, slowly, deactivate. Thus, it can be assumed that domains 1 and 2 rapidly attain equilibrium with  $p$  and  $c$ , but domain 3 relaxes to its steady state with time constant  $\tau_h$ .

Taking  $p_3$  as  $h$  for notational convenience, Equation (2.8) can also be expressed as

$$h = \frac{k_2^2}{k_2^2 + c^2}$$

and following from (2.9), the rate of change of  $c$  due to  $\text{Ca}^{2+}$  flux through the IPR can be written as

$$\begin{aligned}\frac{dc}{dt} &= k_{\text{flux}} \left( \mu_0 + \frac{\mu_1 p}{k_\mu + p} \right) h \left( b + \frac{V_1 c}{k_1 + c} \right) \\ \tau_h \frac{dh}{dt} &= \frac{k_2^2}{k_2^2 + c^2} - h\end{aligned}$$

In addition, the  $\text{Ca}^{2+}$  flux out of the cytosol due to  $\text{Ca}^{2+}$ -dependent pumping is represented by

$$J_{\text{pump}} = \frac{\gamma c}{k_\gamma + c}$$

where  $\gamma$  is the maximal rate at which  $\text{Ca}^{2+}$  is pumped out of the cytosol, and  $k_\gamma$  is the value of  $c$  for which the rate of  $\text{Ca}^{2+}$  pumping is at half-maximum. By including a term for the constant  $\text{Ca}^{2+}$  leak from the extracellular space into the cytoplasm (i.e.  $J_{\text{leak}} = \beta$ ), we finally complete the derivation of the model (Equations (2.1) and (2.2)).

## Additional constraints

The models simulated in this project will be based on the Equations (2.1) and (2.2) (which will henceforth be referred to as the Atri Model), but will operate under some additional constraints:

- i There is no influx of  $\text{Ca}^{2+}$  from outside the cell i.e.  $J_{\text{leak}} = 0$ .
- ii Boundary effects between adjacent cells are neglected.

To investigate intercellular  $\text{Ca}^{2+}$  waves over a tissue culture, Wilkins & Sneyd (1998) applied the Atri model to simulate  $\text{Ca}^{2+}$  dynamics within a single cell. However, at the cell boundaries, they assumed the  $\text{Ca}^{2+}$  flux across the cell membrane to be proportional to the difference in  $\text{Ca}^{2+}$  concentration across the membrane. For this project, the effects at the cell boundaries will be ignored so that the Atri model (originally designed for a single cell) can be applied over the entirety of the embryonic epithelial tissue - a multicellular structure.

- iii The underlying tissue is isotropic and homogeneous.

## 2.3 Nondimensionalising the model

Nondimensionalisation is a useful technique that allows for the removal of units from an equation involving physical quantities, by applying a suitable substitution of variables. This is particularly useful for complex systems of equations involving multiple parameters, as it drastically reduces the number of parameters present in the dimensional model to a key set of aggregate parameters that govern the system dynamics (Hall, 2012).

The nondimensionalised model can provide insight into the scale of the parameters i.e. if a model parameter is small compared to the others, it may be neglected to simplify analysis of the model. This is particularly useful in those cases where the system only yields numerical solutions, where nondimensionalisation can greatly reduce the computation time for extensive simulations which fully explore the parameter space.

To nondimensionalise the Atri model (equations (2.1) and (2.2)), we follow the method in Kaouri et al. (2019). Set  $c = k_1 \bar{c}$  and  $t = \tau_h \bar{t}$ , and neglect  $J_{\text{leak}}$  (as  $\beta$  is much smaller compared to the other parameters, see Appendix A1). Dropping bars for notational convenience, the following model is obtained:

$$\frac{dc}{dt} = \mu h K_1 \frac{b+c}{1+c} - \frac{\Gamma c}{K+c}, \quad (2.10)$$

$$\frac{dh}{dt} = \frac{K_2^2}{K_2^2 + c^2} - h \quad (2.11)$$

In Equation (2.10)  $K_1 = k_f \tau_h / k_1$ ,  $\Gamma = \gamma \tau_h / k_1$ , and  $K = k_\gamma / k_1$ . In (2.11)  $K_2 = k_2 / k_1$ . Using the parameter values of Atri et al. (1993) (see Appendix A1, Table A1.1), we obtain

$K_2 = 1$ ,  $\Gamma = 40/7 = 5.71$ , and  $K = 1/7$ . The parameter ‘ $\mu$ ’, the proportion of active IPRs with bound  $IP_3$ , is taken as a bifurcation parameter with which to explore the behaviour of the model.

## 2.4 Linear stability analysis

A non-linear system can be linearised in the vicinity of its equilibrium points using the system’s Jacobian. Upon evaluating the Jacobian, we obtain the system eigenvalues, which reveal the nature of system stability about the corresponding equilibrium point.

To perform stability analysis for the Atri model, we start by looking for the equilibrium points (steady states) of Equations (2.10) & (2.11). The steady states can be found at the intersections of the system nullclines. Setting

$$\frac{dc}{dt} = 0 \implies h = \frac{\Gamma}{\mu K_1} \frac{c(1+c)}{(K+c)(b+c)}, \quad (2.12)$$

$$\frac{dh}{dt} = 0 \implies h = \frac{1}{1+c^2}. \quad (2.13)$$

we obtain

$$\mu K_1 \frac{1}{1+c^2} \frac{b+c}{1+c} - \frac{\Gamma c}{K+c} = 0, \quad (2.14)$$

which can be cast as a quartic equation in  $c$ ,

$$\Gamma c^4 + \Gamma c^3 - (\mu K_1 - \Gamma)c^2 - (\mu K_1(K+b) - \Gamma)c - \mu K_1 K b = 0. \quad (2.15)$$

The qualitative behaviour of the solutions of the system can be determined by visually inspecting a plot of the nullclines (2.12) and (2.13). When the nullclines intersect, the system has a distinct steady state and when they touch, the system has a double (degenerate) steady state.

Equation (2.14) can be rearranged to express  $\mu$  in terms of  $c$ ,

$$\mu = \frac{\Gamma c(c^3 + c^2 + c + 1)}{K_1 c^2 + K_1(K+b)c + K_1 K b} \quad (2.16)$$

This expression can be evaluated over a range of values of  $c$  to generate a list of  $(c, \mu)$  value pairs, which can be used to plot the equilibrium curve in Figure 2.1. This curve depicts the number of steady states and the corresponding value(s) of  $c$ , for increasing  $\mu$ . It is to be noted that the values of  $\mu$  are specified to five decimal places because the bifurcation analysis depends sensitively on  $\mu$ .

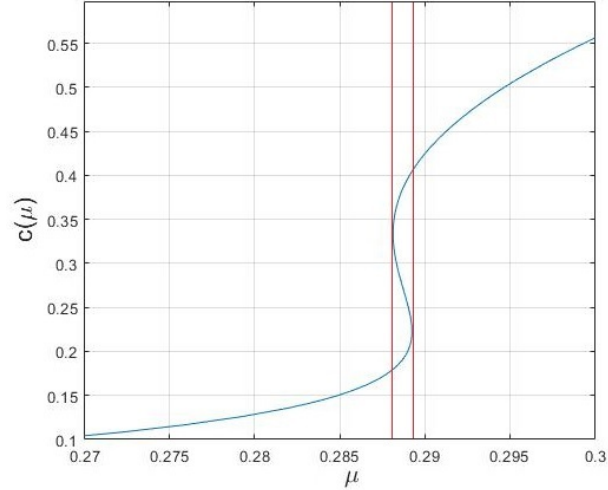


Figure 2.1: Steady states ( $c$ ) of the system v/s bifurcation parameter ( $\mu$ ).

*Software:* MATLAB

In Figure 2.1, note the small bistability window between the dashed lines. For each  $\mu$ -value within that range, two of the equilibrium points are nodes (can be either stable or unstable nodes). This range can be determined by setting  $d\mu/dc = 0$ .

$$\frac{d\mu}{dc} = 0 \implies \begin{cases} c_1 = 0.22281 \Rightarrow \mu_1 = 0.28925 \\ c_2 = 0.33374 \Rightarrow \mu_2 = 0.28814 \end{cases}$$

A bifurcation occurs when a small, smooth change to a parameter value (the bifurcation parameter) of the model results in an abrupt, ‘qualitative’ change in the system’s behaviour. There exist a wide variety of bifurcation types but the Atri model under study exhibits a particular type of bifurcation, a *Hopf bifurcation*. A Hopf bifurcation occurs when a periodic solution or a limit cycle, in the vicinity of an equilibrium point, arises or vanishes upon varying the bifurcation parameter (Lynch, 2004).

To identify the bifurcations of the Atri model, we start by linearising the system near its steady states. Recall Equations (2.10) and (2.11),

$$\begin{aligned} \frac{dc}{dt} &= F(c, h) \\ \frac{dh}{dt} &= G(c, h) \end{aligned}$$

The Jacobian of the system is given by

$$J = \begin{bmatrix} F_c & F_h \\ G_c & G_h \end{bmatrix}, \quad (2.17)$$

and the characteristic polynomial of the system is given by

$$\omega^2 - \text{Tr}(J)\omega + \text{Det}(J) = 0, \quad (2.18)$$

where  $\omega$  represents the eigenvalues and the Trace (Tr), Determinant (Det) and Discriminant (Discr) of the Jacobian are as follows

$$\begin{aligned} \text{Tr}(J) &= F_c + G_h = F_c - 1 = \frac{\Gamma}{(K+c)} \left( -\frac{K}{K+c} + \frac{(1-b)\Gamma c}{(1+c)(b+c)} \right) - 1 \\ \text{Det}(J) &= F_c G_h - F_h G_c = -\frac{\Gamma}{(K+c)} \left( -\frac{K}{K+c} + \frac{(1-b)\Gamma c}{(1+c)(b+c)} \right) + \frac{2\Gamma c^2}{(1+c^2)(K+c)} \\ \text{Discr}(J) &= (\text{Tr}(J))^2 - 4\text{Det}(J) \end{aligned}$$

The characteristic polynomial can be easily solved to determine the eigenvalues. However, it is quite taxing to identify bifurcation points using this method. The paper by Kaouri et al. (2019) utilizes a far more convenient method to identify bifurcation points, by evaluating the nature of the roots of the characteristic polynomial over a range of values for  $\mu$  (the bifurcation parameter). By monitoring when the sign changes in the expressions for  $\text{Det}(J)$ ,  $\text{Tr}(J)$  and  $\text{Discr}(J)$ , we can isolate the bifurcation points.

A full list of system bifurcations is presented in Kaouri et al. (2019):

- $0 < \mu < 0.27828$ : one stable node.
- $\mu = 0.27828$ : the stable node becomes a stable spiral (bifurcation  $\text{Discr}=0$ )
- $\mu = 0.28814$ : Stable spiral present. Also, a saddle and an unstable node (UN) emerge (bifurcation  $\text{Det}=0$ , fold point)
- $\mu = 0.28900$ : the stable spiral becomes an unstable spiral. The other two steady states are still a saddle and an unstable node. ( $\text{Tr}=0$ , Hopf bifurcation)
- $\mu = 0.28924$  the unstable spiral becomes an unstable node, and we have two unstable nodes and a saddle ( $\text{Discr}=0$ )
- $\mu = 0.28925$ : one unstable node ( $\text{Det}=0$ , fold point)
- $\mu = 0.28950$ : the unstable node becomes an unstable spiral ( $\text{Discr}=0$ )
- $\mu = 0.49500$ : the unstable spiral becomes a stable spiral. ( $\text{Tr}=0$ , Hopf bifurcation)

From the regimes identified above, the regime of relaxation oscillations is of particular interest since their amplitude and/or frequency encodes the information in  $\text{Ca}^{2+}$  signals.

Since a Hopf bifurcation arises at  $\mu = 0.28900$ , the stable spiral becomes unstable, and we expect relaxation oscillations (limit cycles) due to the non-linearity of the system. Therefore, relaxation oscillations are sustained for  $0.28900 \leq \mu \leq 0.49500$ . As  $\mu$  increases, the unstable spiral becomes a stable spiral close to  $\mu = 0.495000$  and the limit cycles eventually vanish (Kaouri et al., 2019).

## 2.5 Simulations

To observe the time evolution of the Atri model for different bifurcation regimes, Equations (2.10) & (2.11) were solved in MATLAB (MathWorks, 2020) using the `ode45` function for the system parameters specified in Table A1.1. Initial conditions taken:  $c(0) = 1$ ,  $h(0) = 1$ .

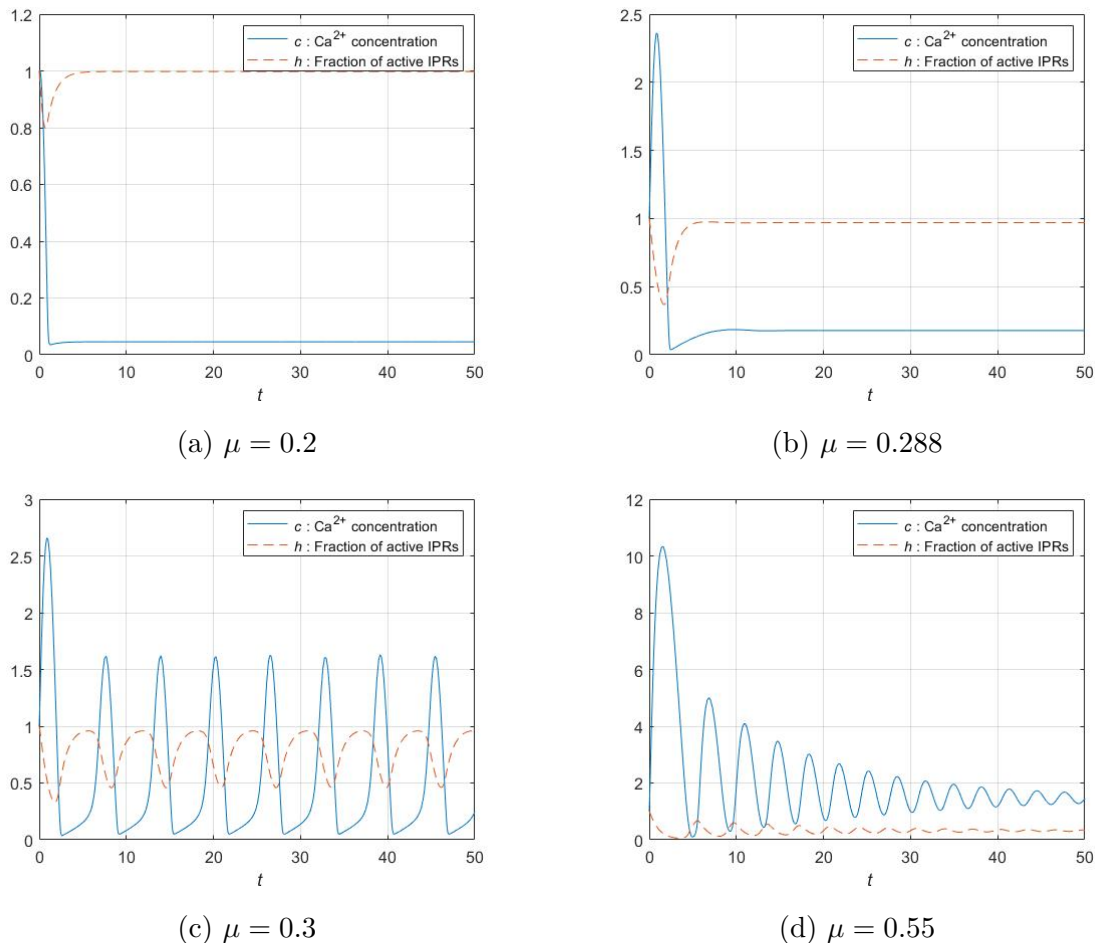
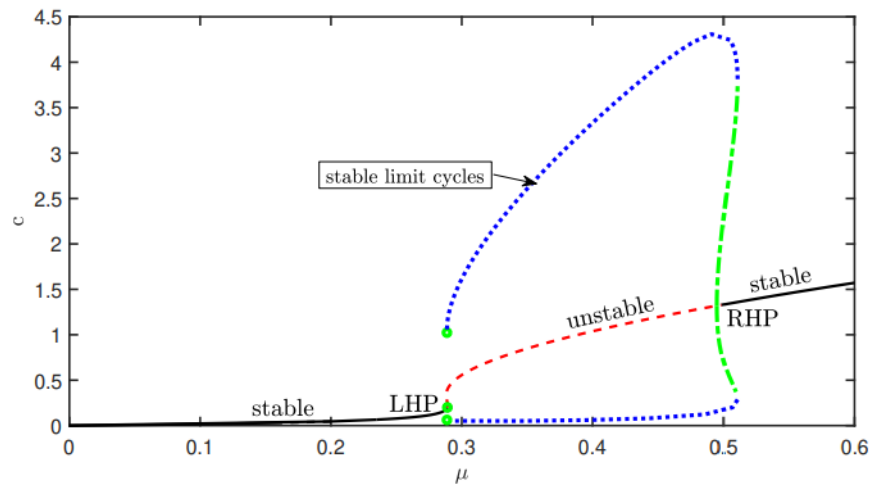
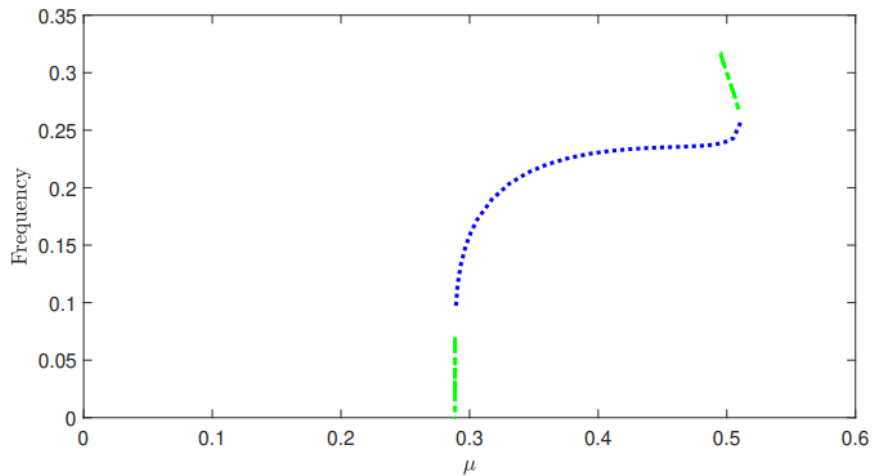


Figure 2.2: Solutions of  $c$  and  $h$  for the Atri model (2.10)-(2.11) over  $0 \leq t \leq 50$  for a range of  $\mu$ . *Software: MATLAB*

In Figure 2.2a ( $\mu = 0.2$ ): the system rapidly reaches steady state (stable node). In Figure 2.2b ( $\mu = 0.288$ ):  $c$  initially overshoots its steady state value before  $c$  and  $h$  both settle down at their respective steady state values (stable spiral). Biologically, this  $\text{Ca}^{2+}$  ‘spike’ corresponds to an action potential. In Figure 2.2c ( $\mu = 0.3$ ): the system exhibits oscillations because of its non-linear nature (limit cycles). In Figure 2.2d ( $\mu = 0.55$ ): the system oscillations are observed to die out over time (stable spiral). Thus, system behaviour is observed to be in agreement with the results of the linear stability analysis.



(a) Amplitude of  $\text{Ca}^{2+}$  oscillations (limit cycles)



(b) Frequency of limit cycles

Figure 2.3: Bifurcation diagram of the Atri model for increasing  $\mu$ . The (blue) dots represent stable limit cycles and the (green) dash-dotted part corresponds to unstable limit cycles. *Source:* (Kaouri et al., 2019)

Figure 2.3 depicts the change in the characteristics of the limit cycles with increasing  $\mu$ . Kaouri et al. (2019) used the XPPAUT continuation software to plot this bifurcation diagram. Figure 2.3a plots the amplitude of the oscillations. Both stable and unstable limit cycles are displayed. The left Hopf point (LHP) and the right Hopf point (RHP) are at  $\mu = 0.289$  and  $\mu = 0.495$  respectively. Figure 2.3b plots the frequency of the oscillations. The range of  $\mu$  for which both a stable and an unstable limit cycle are sustained is clearly visible as the double-valued part of the curve. In these figures, it can be seen that oscillations increase significantly in amplitude, but not as much in frequency, when the value of  $\mu$  is increased.

In this chapter, we reviewed the Atri model and its underlying assumptions. According to Atri et al. (1993), the following three characteristics are sufficient for producing  $\text{Ca}^{2+}$  oscillations:

- i a single  $\text{IP}_3$ -sensitive intracellular pool of  $\text{Ca}^{2+}$ ;
- ii the biphasic dependence of the IPRs on  $c$ ;
- iii the separation of time scales for IPR activation and inactivation.

Bifurcation regimes were then identified after performing linear stability analysis on the model. Finally, these regimes were used to run simulations of the Atri model.

# Chapter 3

## The Atri model with diffusion (1D)

$\text{Ca}^{2+}$  waves are believed to be an efficient means of encoding information and intracellular signal transmission (Lechleiter & Clapham, 1992). These waves are used to transmit signals both inside cells and in between cells. Intracellular waves enable individual cells to respond to a stimulus, while intercellular waves can elicit a coordinated response from an entire tissue.

After agonist stimulation triggers the release of  $\text{IP}_3$ , it diffuses through the cytoplasm and binds to the IPRs located on the ER and nuclear membrane. When  $\text{IP}_3$  binds to the IPRs, they open and start acting as  $\text{Ca}^{2+}$  channels, releasing large amounts of  $\text{Ca}^{2+}$  from the pool within the ER. The  $\text{Ca}^{2+}$  released into the cytosol then diffuses outward, activating IPRs on other ERs, and leads to further release of  $\text{Ca}^{2+}$  in an autocatalytic process called  $\text{Ca}^{2+}$ -induced  $\text{Ca}^{2+}$  release (CICR).  $\text{Ca}^{2+}$  release through the IPR is terminated when high concentrations of cytosolic  $\text{Ca}^{2+}$  inactivate the receptor (M. J. Berridge, 1993).

The general mechanism for  $\text{Ca}^{2+}$  wave propagation is as follows (Atri et al., 1993): an initial bolus of  $\text{IP}_3$  initiates  $\text{Ca}^{2+}$  release via IPRs in the region with high  $\text{IP}_3$ . As the  $\text{IP}_3$  diffuses rapidly outward, it primes other IPRs (by activating domain 1) and initiates additional  $\text{Ca}^{2+}$  release. The released  $\text{Ca}^{2+}$  has a slower diffusion rate and upon reaching the primed IPRs, initiates greater  $\text{Ca}^{2+}$  release by activating domain 2. In this way, an outwardly propagating  $\text{Ca}^{2+}$  wave is generated. When  $c$  starts to peak, it activates domain 3 on the IPRs, inhibiting  $\text{Ca}^{2+}$  release through the channel. After the inactivation of a sufficient number of channels, the rate of  $\text{Ca}^{2+}$  release drops and  $\text{Ca}^{2+}$  ATPase pumps move the cytosolic  $\text{Ca}^{2+}$  back into the intracellular pool and to the outside of the cell. As a result,  $c$  begins to decrease and a wave back is created. The region behind the wave back experiences a classic refractory period, which is enhanced by channel inactivation occurring on a slower time scale than activation.

Chapter 2 described the Atri model for  $\text{Ca}^{2+}$  oscillations, taking the  $\text{Ca}^{2+}$  distribution to be spatially homogeneous i.e. neglecting the diffusion of  $\text{Ca}^{2+}$ . In this chapter, we introduce

a diffusion term for  $c$  in the model which allows the solution to yield  $\text{Ca}^{2+}$  waves.

### 3.1 The Atri model with diffusion

Although the complex spatiotemporal behaviour of  $\text{Ca}^{2+}$  in the *Xenopus* oocyte is wavelike in nature (Lechleiter & Clapham, 1992; Girard & Clapham, 1993; Camacho & Lechleiter, 1993; Parker & Yao, 1991), J. D. Murray (1989) postulates that it must arise as a consequence of an underlying excitable, oscillatory temporal mechanism.

Therefore, in order to simulate the diffusion of  $\text{Ca}^{2+}$  waves across the oocyte, Atri et al. (1993) extended their model for  $\text{Ca}^{2+}$  oscillations (equations (2.1) and (2.2)) to two spatial dimensions and included terms for cytosolic diffusion of  $\text{Ca}^{2+}$  and  $\text{IP}_3$ , and  $\text{IP}_3$  breakdown. It is assumed that  $\text{Ca}^{2+}$  diffuses with a constant diffusion coefficient. The extended model is given by:

$$\frac{\partial c}{\partial t} = D_c \nabla^2 c + J_{\text{channel}}(c, h, p) - J_{\text{pump}}(c) + J_{\text{leak}}, \quad (3.1)$$

$$\tau_h \frac{\partial h}{\partial t} = h_\infty(c) - h, \quad (3.2)$$

$$\frac{\partial p}{\partial t} = D_p \nabla^2 p - k_p p, \quad (3.3)$$

where

$$J_{\text{channel}}(c, h, p) = k_{\text{flux}} \mu(p) h \frac{bk_1 + c}{k_1 + c}, \quad J_{\text{pump}}(c) = \frac{\gamma c}{k_\gamma + c}, \quad J_{\text{leak}} = \beta,$$

and

$$h_\infty(c) = \frac{k_2^2}{k_2^2 + c^2}, \quad \mu(p) = \mu_0 + \frac{\mu_1 p}{k_\mu + p}.$$

As was the case in Chapter 2, in equations (3.1), (3.2) and (3.3), the variables  $c$  and  $p$  represent the cytosolic  $\text{Ca}^{2+}$  and  $\text{IP}_3$  concentrations, respectively, and  $h$  is a dimensionless variable denoting the proportion of IPRs that have not been inactivated. Although  $\text{IP}_3$  dynamics influence the propagation of  $\text{Ca}^{2+}$  waves, the models in this project will not consider  $\text{IP}_3$  as a dynamic variable. Instead,  $\text{IP}_3$  will be regarded as a control parameter, giving us a simpler model. This will, eventually, allow us to more clearly understand the relationship between  $\text{Ca}^{2+}$  dynamics and cellular mechanics in Chapters 4 & 5.

In keeping with the experiments that examined the  $\text{Ca}^{2+}$  and  $\text{IP}_3$  dependence of intracellular  $\text{Ca}^{2+}$  wave propagation, Atri et al. (1993) used the intracellular release of  $\text{Ca}^{2+}$  or  $\text{IP}_3$  to generate  $\text{Ca}^{2+}$  waves. To simulate this, they elevated the concentration of  $\text{Ca}^{2+}$  or  $\text{IP}_3$

in a region of the cell and held it at a fixed value for a short amount of time (ranging from a few hundred milliseconds to a few seconds in different simulations). In addition, they set  $\beta = 0$  i.e. implying no influx of  $\text{Ca}^{2+}$  from outside the cell, to simulate the experimental conditions in which there was little to no extracellular  $\text{Ca}^{2+}$  present when the oscillations and waves were induced (Lechleiter & Clapham, 1992). No-flux conditions were chosen to simulate the boundaries of the cell.

An interesting prediction of this model is that propagating  $\text{Ca}^{2+}$  waves will not be generated unless the  $\text{Ca}^{2+}$ -dependent inactivation of the IPRs occurs on a time scale at least twice as slow as the  $\text{Ca}^{2+}$ -dependent activation of the IPRs i.e.  $\tau_h \geq 2s$ . Regardless of the method of stimulation, the  $\text{Ca}^{2+}$  waves generated by the model behave just like waves seen in any classical excitable medium. Waves initiated from different foci may fuse to form a joint wavefront and colliding waves have been observed to annihilate due to the existence of a refractory period immediately behind the wave (Atri et al., 1993).

One possible cause for the annihilation of colliding  $\text{Ca}^{2+}$  waves is that the  $\text{Ca}^{2+}$  release from intracellular stores is completely inhibited following the passage of a wave. The slow removal of this inhibition defines the refractory period (Camacho & Lechleiter, 1995). The underlying cause for the inhibition of  $\text{Ca}^{2+}$  release has yet to be identified, but there are two likely possibilities. The first explanation is that, the intracellular stores could be temporarily depleted of releasable  $\text{Ca}^{2+}$  by a passing wave. In this case, the refractory period corresponds to the time required to refill the  $\text{Ca}^{2+}$  stores (Camacho & Lechleiter, 1995). The second is that, a  $\text{Ca}^{2+}$  wave could temporarily inactivate IPR channels, until  $\text{Ca}^{2+}$  is lowered to resting levels (Watras et al., 1991). It should be noted that the Atri model operates on the basis of the latter assumption.

## 3.2 Nondimensionalising the model

Although Atri et al. (1993) extended their  $\text{Ca}^{2+}$  diffusion model to two spatial dimensions, this chapter discusses the behaviour of the Atri model in one spatial dimension only. After gathering insight from the model's behaviour in a simple geometry, the model will be extended to two spatial dimensions, in Chapter 6.

To nondimensionalise the Atri model (equations (3.2) and (3.3)), we follow the same procedure used in Chapter 2. Set  $c = k_1 \bar{c}$ ,  $t = \tau_h \bar{t}$ ,  $x = l \bar{x}$ , and neglect  $J_{\text{leak}}$  (as  $\beta$  is very small compared to the other parameters, see Appendix A1). Dropping bars for notational

convenience, the following model is obtained:

$$\frac{\partial c}{\partial t} = D_o \frac{\partial^2 c}{\partial x^2} + \mu h K_1 \frac{b+c}{1+c} - \frac{\Gamma c}{K+c}, \quad (3.4)$$

$$\frac{\partial h}{\partial t} = \frac{K_2^2}{K_2^2 + c^2} - h \quad (3.5)$$

In Equation (3.4)  $D_o = D_c \tau_h / l^2$ ,  $K_1 = k_f \tau_h / k_1$ ,  $\Gamma = \gamma \tau_h / k_1$ , and  $K = k_\gamma / k_1$ . In (3.5)  $K_2 = k_2 / k_1$ . Taking  $l = 20 \mu m$  and using the parameter values of Atri et al. (1993) (see Appendix A1, Table A1.1), we obtain  $K_2 = 1$ ,  $\Gamma = 40/7 = 5.71$ ,  $K = 1/7$ , and  $D_o = 0.1$ . Here, it is important to note that Atri et al. (1993) chose the value of  $D_c$  to be  $20 \mu m^2 \cdot s^{-1}$  for consistency with the experimental estimates of Allbritton et al. (1992). The parameter ‘ $\mu$ ’, the proportion of IPRs with bound IP<sub>3</sub>, is taken as a bifurcation parameter with which to explore the behaviour of the model.

It should be noted that, in each chapter, the simulation results were obtained by solving the non-dimensional models, so all of the plots in this report will use non-dimensional units. This will suffice because we are primarily interested in the qualitative changes in system behaviour.

### 3.3 Simulations

To observe the spatiotemporal evolution of the spatially extended Atri model for different bifurcation regimes, Equations (3.4) & (3.5) were solved numerically in COMSOL Multiphysics (COMSOL, 2019) for the system parameters specified in Table A1.1, over a domain size of  $1000 \mu m$  (i.e.  $-25 \leq x \leq 25$  in nondimensional units), applying no flux boundary conditions (Equations (3.6)-(3.9)). A typical embryonic neuroepithelial cell is  $\approx 50 \mu m$  in diameter (Qi et al., 2013). To model  $Ca^{2+}$  signalling over an epithelial tissue, we consider a  $Ca^{2+}$  wave diffusing outward over 20 cells placed side to side. Therefore, a domain size of  $1000 \mu m$  was chosen for the simulations.

$$c_x(-25, t) = 0 \quad (3.6)$$

$$c_x(25, t) = 0 \quad (3.7)$$

$$h_x(-25, t) = 0 \quad (3.8)$$

$$h_x(25, t) = 0 \quad (3.9)$$

Equations (3.10) and (3.11) are the initial conditions of the system. They represent a

perturbation in  $c$  at the centre of the domain, with all other spatial points taken to be at the steady state values of  $c$  and  $h$ ,  $c_{St}$  and  $h_{St}$  respectively.

$$c(x, 0) = c_{St} + 4 \exp(-50x^2), \quad (3.10)$$

$$h(x, 0) = h_{St} = \frac{1}{1 + c_{St}^2} \quad (3.11)$$

We can recall from Section 2.4 that  $c$  and  $h$  have different steady state values for different values of  $\mu$ . Equation (2.14) was solved in MATLAB to obtain the values of  $c_{St}$  which were then manually input into COMSOL Multiphysics.

It is to be noted that, at steady state, the concentration of  $\text{Ca}^{2+}$  in the ER is high, and thus there is a steep concentration gradient between the ER and the cytoplasm; so, the initial condition (Equation (3.10)) has been set to reflect the same. A thin, steep Gaussian pulse emulates the initial discharge of  $\text{Ca}^{2+}$ , from the intracellular stores within the ER into the cytosol. The simulations were run in COMSOL Multiphysics for the finest mesh setting. It was noted that, if the pulse size of the initial condition was too large, it would either result in divergence or unstable solutions, and if the pulse was too thin, the mesh could not detect the initial condition accurately.

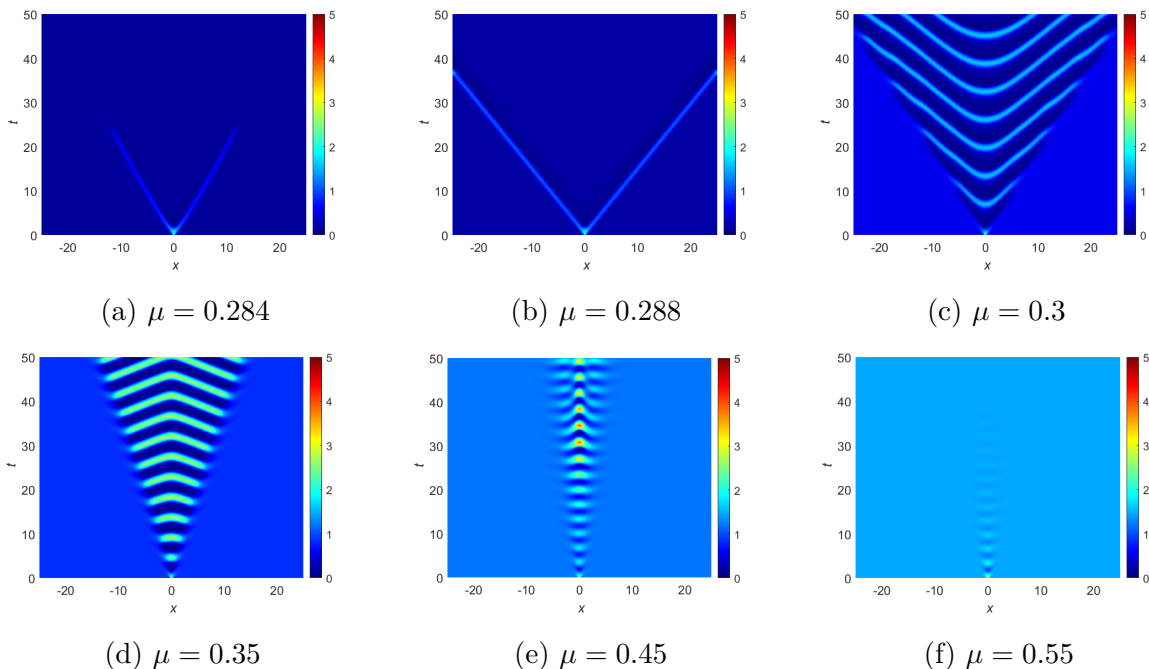


Figure 3.1:  $\text{Ca}^{2+}$  concentration ‘ $c$ ’ over the domain  $-25 \leq x \leq 25$  for  $0 \leq t \leq 50$  generated as solutions of the system (3.4)-(3.11), over a range of  $\mu$ . *Software:* COMSOL Multiphysics

Figure 3.1 depicts system behaviour over a range of values of the bifurcation parameter  $\mu$ . In Chapter 2, the linear stability analysis helped us identify the different bifurcation regimes for the Atri model. In the case of the spatially extended model, the system will experience bifurcations at *approximately* the same values of  $\mu$  due to the inclusion of the small diffusion term. Thus, the simulations were performed with various values of  $\mu$  that lie within the different bifurcation regimes so we could observe the qualitative changes in system behaviour.

- *Decay to steady state* ( $0 \leq \mu < 0.289$ )

$\mu = 0.2$ : The initial pulse simply decays to a steady state very quickly. In the Atri model, this value of  $\mu$  causes the system to rapidly reach steady state (Figure 2.2a). Thus, it is reasonable to expect the solution to decay to a steady state in the spatially extended model, as well.

$\mu = 0.284$ : In Figure 3.1a, the initial pulse triggers an action potential at  $x = 0$ . This action potential, then, induces two solitary pulses that travel in opposite directions. However, these pulses decay after travelling a short distance. In the Atri model, this value of  $\mu$  produced a solution that, again, decayed to steady state. Here, due to diffusion, we get solitary pulses which travel some distance before decaying.

$\mu = 0.288$ : In Figure 3.1b, the initial pulse triggers an action potential at  $x = 0$ , which is followed by two solitary pulses travelling in opposite directions. These pulses do not decay, they continue to propagate outward towards the boundaries without noticeable attenuation. For this value of  $\mu$ , the Atri model produced an action potential (Figure 2.2b) but here, owing to diffusion, we get travelling solitary pulses that do not decay. It is likely that, because this value of  $\mu$  is close to a bifurcation point, this behaviour corresponds to a transitory state of the system.

- *Periodic wavetrains* ( $0.289 < \mu < 0.495$ )

$\mu = 0.3$ : In Figure 3.1c, the initial pulse triggers limit cycles and two periodic wavetrains that travel outward in opposing directions.

$\mu = 0.35$ : In Figure 3.1d, the initial pulse induces waves that then move inward, toward the origin. These inward-moving, periodic wavetrains are generated at two equidistant points on either side of the origin. The wavetrains meet each other at the origin.

$\mu = 0.45$ : Over short simulation times (Figure 3.1e), the system only produces limit cycles at  $x = 0$  but, upon increasing the simulation runtime (Figure 3.8), it was observed that the system displayed some interesting wave patterns.

The Atri model produces limit cycles for each of these values of  $\mu$  (see Figure 2.2c). This behaviour corresponds to periodic wavetrains in the spatially extended model.

- *Decaying oscillations* ( $0.495 < \mu$ )

$\mu = 0.55$ : In Figure 3.1f, the initial pulse triggers oscillations at the point of origin. These oscillations are observed to die out with time. For this value of  $\mu$ , the Atri model displayed oscillations that died out with time, as well (Figure 2.2d).

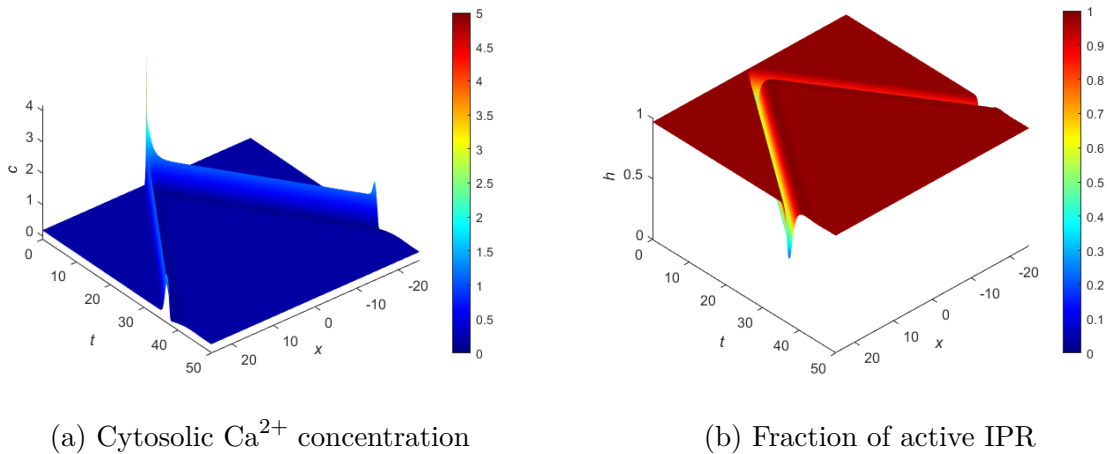


Figure 3.2: (a)  $\text{Ca}^{2+}$  concentration ‘ $c$ ’ and (b) fraction of active IPRs ‘ $h$ ’ over the domain  $-25 \leq x \leq 25$  for  $0 \leq t \leq 50$  generated as solutions of the system (3.4)-(3.11),  $\mu = 0.288$ .

*Software:* COMSOL Multiphysics

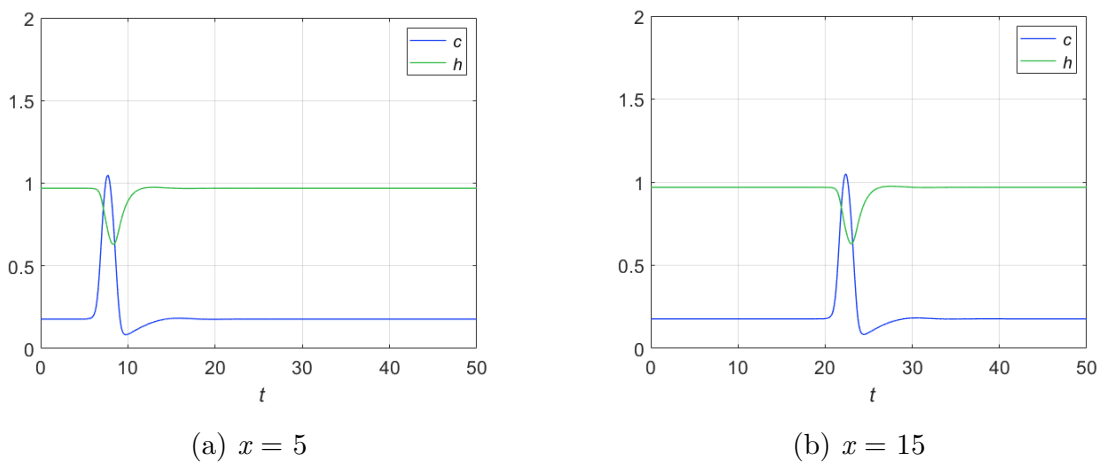


Figure 3.3: Time evolution of  $c$  and  $h$ , solutions of the system (3.4)-(3.11), at (a)  $x = 5$  and (b)  $x = 15$ .  $\mu = 0.288$ . *Software:* COMSOL Multiphysics

Figure 3.2 depicts surface plots of  $c$  and  $h$ , obtained as solutions for the spatially extended Atri model, for  $\mu = 0.288$ . Figure 3.3 depicts the evolution of  $c$  and  $h$  with time at points  $x = 5$  and  $x = 15$ . These plots can be visualised as slices taken from Figures 3.2a & 3.2b along the lines  $x = 5$  and  $x = 15$ . It is sufficient to obtain these plots for only positive values of  $x$  because, as we see in Figure 3.2, the wave pattern is symmetric about  $x = 0$ .

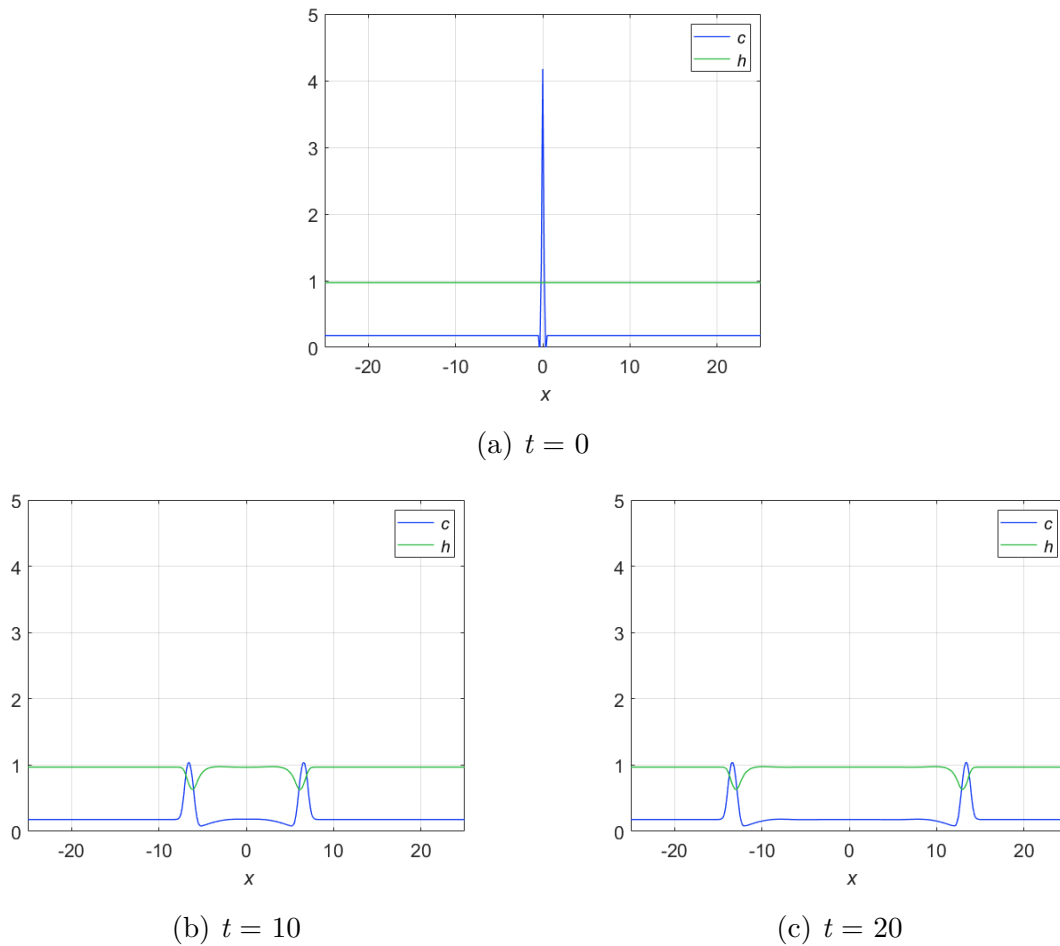
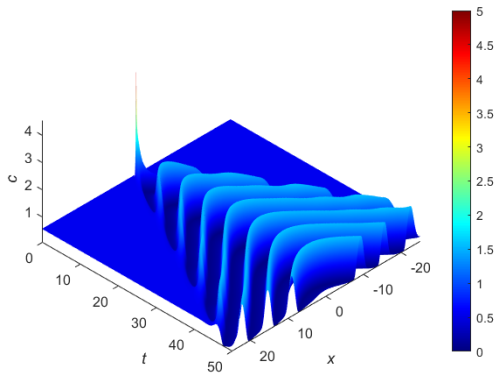
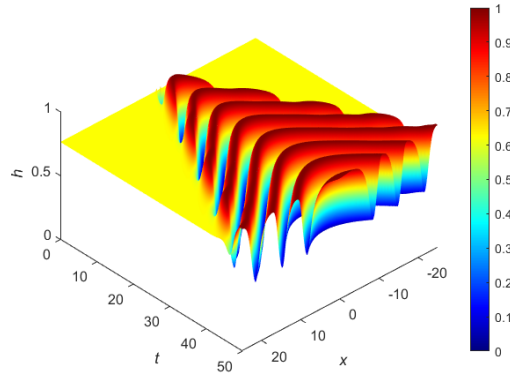


Figure 3.4: Spatial distribution of  $c$  and  $h$ , solutions of the system (3.4)-(3.11), at (a)  $t = 0$ , (b)  $t = 10$ , and (c)  $t = 20$ .  $\mu = 0.288$ . *Software: COMSOL Multiphysics*

Figure 3.4 depicts the distribution of  $c$  and  $h$  over the domain at time instants  $t = 0$ , 10 & 20. These plots can be visualised as slices taken from Figures 3.2a & 3.2b along the lines  $t = 0$ , 10 & 20. By measuring the distance travelled by a  $\text{Ca}^{2+}$  pulse between  $t = 10$  and  $t = 20$ , the speed of a  $\text{Ca}^{2+}$  wave was calculated to be  $6.95\mu\text{m}/\text{s}$ .



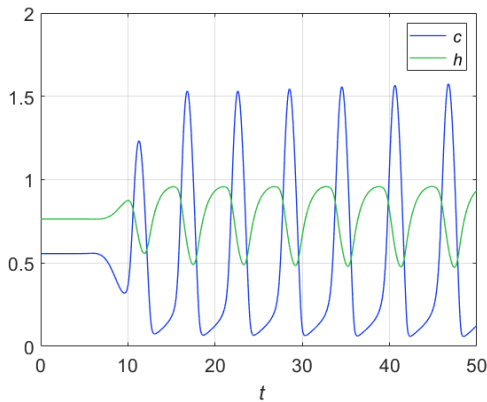
(a) Cytosolic  $\text{Ca}^{2+}$  concentration



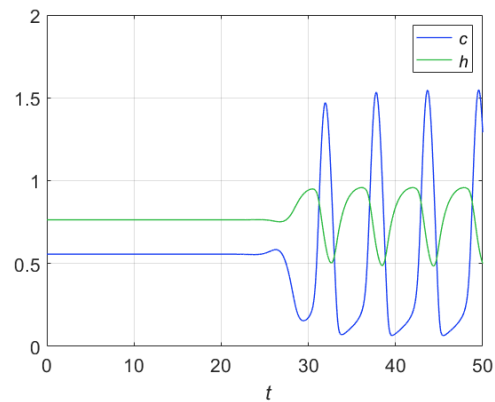
(b) Fraction of active IPR

Figure 3.5: (a)  $\text{Ca}^{2+}$  concentration ‘ $c$ ’ and (b) fraction of active IPRs ‘ $h$ ’ over the domain  $-25 \leq x \leq 25$  for  $0 \leq t \leq 50$  generated as solutions of the system (3.4)-(3.11),  $\mu = 0.3$ .

*Software:* COMSOL Multiphysics



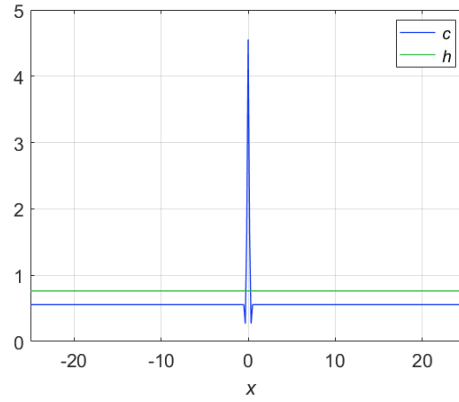
(a)  $x = 5$



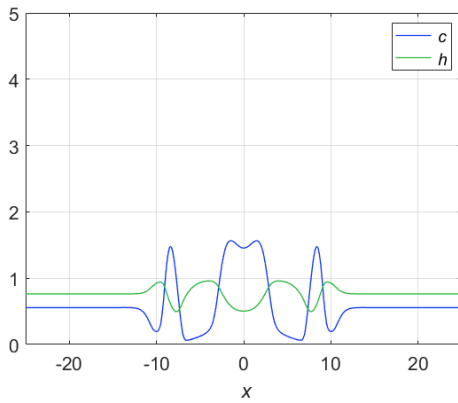
(b)  $x = 15$

Figure 3.6: Time evolution of  $c$  and  $h$ , solutions of the system (3.4)-(3.11), at (a)  $x = 5$  and (b)  $x = 15$ .  $\mu = 0.3$ . *Software:* COMSOL Multiphysics

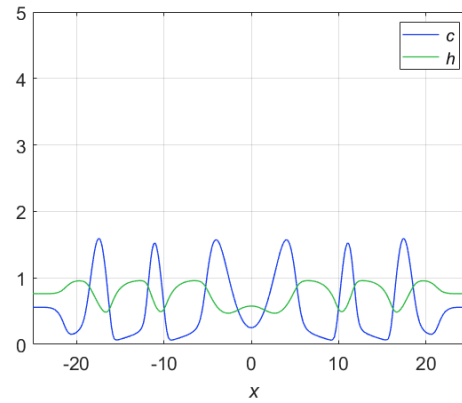
Figure 3.5 depicts surface plots of  $c$  and  $h$ , obtained as solutions for the spatially extended Atri model, for  $\mu = 0.3$ . Figure 3.6 depicts the evolution of  $c$  and  $h$  with time at points  $x = 5$  and  $x = 15$ . These plots can be visualised as slices taken from Figures 3.5a & 3.5b along the lines  $x = 5$  and  $x = 15$ . It is sufficient to obtain these plots for only positive values of  $x$  because, as we see in Figure 3.5, the wave pattern is symmetric about  $x = 0$ .



(a)  $t = 0$



(b)  $t = 20$



(c)  $t = 40$

Figure 3.7: Spatial distribution of  $c$  and  $h$ , solutions of the system (3.4)-(3.11), at (a)  $t = 0$ , (b)  $t = 20$ , and (c)  $t = 40$ .  $\mu = 0.3$ . *Software:* COMSOL Multiphysics

Figure 3.7 depicts the distribution of  $c$  and  $h$  over the domain at time instants  $t = 0$ , 20 & 40. These plots can be visualised as slices taken from Figures 3.5a & 3.5b along the lines  $t = 0$ , 20 & 40. By measuring the distance travelled by a  $\text{Ca}^{2+}$  pulse between  $t = 20$  and  $t = 40$ , the speed of a  $\text{Ca}^{2+}$  wave was calculated to be  $4.45\mu\text{m}/\text{s}$ .

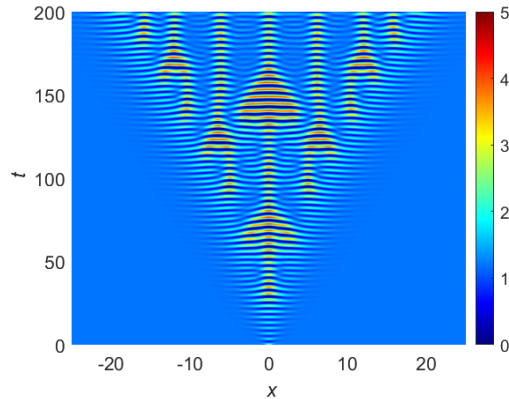


Figure 3.8:  $\text{Ca}^{2+}$  concentration ‘ $c$ ’ over the domain  $-25 \leq x \leq 25$  for  $0 \leq t \leq 200$  generated as a solution of the system (3.4)-(3.11),  $\mu = 0.45$ .

*Software:* COMSOL Multiphysics

Figure 3.8 depicts a contour plot of  $c$ , obtained as a solution for the spatially extended Atri model, for  $\mu = 0.45$ . After  $t \approx 75$ , some very interesting wave patterns begin to appear.

Over the course of the simulations, it was found that the choice of non-dimensional diffusion coefficient  $D_o$  greatly impacted the solutions. In general, it was observed that reducing the value of  $D_o$  below 0.1 led to divergence, particularly for the cases with lower values of  $\mu$ . This influenced the choice of  $l$  ( $= 20\mu\text{m}$ ), used to non-dimensionalise the system.

In this chapter, we looked at the solutions of the spatially extended Atri model and observed some interesting patterns. As noted in Chapter 2, for an appropriate range of  $\text{IP}_3$ ,  $\text{Ca}^{2+}$  oscillations occur at a constant value of  $\text{IP}_3$ . Above this range, a sustained elevation of  $c$  is observed rather than oscillations (Atri et al., 1993). The insights drawn from the qualitative behaviour of the Atri model were then used to understand the behaviour of the spatially extended Atri model.

# Chapter 4

## Calcium signalling and mechanics: a mechanochemical model

In Chapters 2 and 3, we discussed models describing  $\text{Ca}^{2+}$  oscillations and waves but, so far, no consideration has been given to how these  $\text{Ca}^{2+}$  signals impact the cells. Over the course of embryogenesis, cells and tissues generate physical forces, by virtue of which, they change their shape, move and proliferate (Lecuit & Lenne, 2007). Hunter et al. (2014) found that  $\text{Ca}^{2+}$  flashes could induce cell contraction and directly impact morphogenesis. Therefore, it becomes imperative to construct and study models that intertwine  $\text{Ca}^{2+}$  dynamics and cellular mechanics.

The first mechanochemical models for embryogenesis can be found in the works of Oster, Murray and their collaborators (Oster & Odell, 1984; Murray & Oster, 1984; J. D. Murray et al., 1988; J. Murray, 2001). In those early models,  $\text{Ca}^{2+}$  evolution was modelled as a bistable reaction-diffusion process where the application of stress could ‘switch’ the  $\text{Ca}^{2+}$  state from low to high stable concentration.

Over time, as more experimental evidence came to light, it became clear that the  $\text{Ca}^{2+}$  dynamics were more complicated than the initial models had assumed. Thus, the mechanochemical model in Kaouri et al. (2019) employs the  $\text{Ca}^{2+}$  dynamics of the empirically verified model in Atri et al. (1993), which encapsulates the experimentally observed  $\text{Ca}^{2+}$ -induced  $\text{Ca}^{2+}$  release (CICR) process.

Many experimental studies have shown that actomyosin-based contractions are produced in response to  $\text{Ca}^{2+}$  release in both embryonic and cultured cells (Christodoulou & Skourides, 2015; Herrgen et al., 2014; Hunter et al., 2014; Suzuki et al., 2017; Wallingford et al., 2001). The ability of cells to sense and respond to forces by modulating their cytosolic  $\text{Ca}^{2+}$  is also well established. Mechanically induced  $\text{Ca}^{2+}$  waves have been observed in tracheal epithelial

cells, epithelial cells in *Drosophila* wing discs and other cell types (M. J. Sanderson et al., 1990, 1988; M. Sanderson & Sleight, 1981; Narciso et al., 2017). This mutual interplay of  $\text{Ca}^{2+}$  release and cell mechanics points towards the existence of two-way mechanochemical feedback between  $\text{Ca}^{2+}$  and contractions.

The mechanochemical model in Kaouri et al. (2019) captures this two-way feedback and is based on the experiments conducted by Christodoulou & Skourides (2015) on the embryonic neuroepithelial cells of *Xenopus*. This model operates on the basis of a stretch-activation  $\text{Ca}^{2+}$  flux from the extracellular medium. Stretch sensitive calcium channels (SSCCs) have been identified experimentally in recent years (Árnadóttir & Chalfie, 2010; Dupont et al., 2016; Hamill, 2006; Moore et al., 2010). Located on the cell membrane, they allow  $\text{Ca}^{2+}$  to flow into the cytosol from the extracellular space upon activation. The SSCCs are activated upon exposure to mechanical stimulation and they close either by relaxation of, or by adaptation to, the mechanical force.

In this chapter, we study the mechanochemical model developed in Kaouri et al. (2019). We simulate the model using two *novel* traction terms and observe how the system behaviour changes with the traction term.

## 4.1 A mechanochemical model based on the Atri model

In Chapter 2, we discussed how the Atri model (Equations (2.1) & (2.2)) described  $\text{Ca}^{2+}$  oscillations at a point. In this chapter, we will study mechanochemical models based on the Atri model. Kaouri et al. (2019) extended the Atri model by adding a mechanics equation that governs cell dilation/compression over time. Early mechanochemical models included an ad hoc stretch-activation  $\text{Ca}^{2+}$  flux term, following from which, Kaouri et al. (2019) derived this stretch-activation flux as a contribution from the SSCCs in their model. The derived mechanochemical model is as follows:

$$\frac{dc}{dt} = J_{\text{channel}}(c, h) - J_{\text{pump}}(c) + J_{\text{leak}} + J_{\text{SSCC}}(\theta), \quad (4.1)$$

$$\tau_h \frac{dh}{dt} = h_{\infty}(c) - h, \quad (4.2)$$

$$\frac{d\theta}{dt} = -\frac{E'(1 + \nu')}{(\xi_1 + \xi_2)}\theta + \frac{1}{(\xi_1 + \xi_2)}T_D(c), \quad (4.3)$$

where

$$J_{\text{channel}}(c, h) = k_{\text{flux}}\mu h \frac{bk_1 + c}{k_1 + c}, \quad J_{\text{pump}}(c) = \frac{\gamma c}{k_{\gamma} + c}, \quad J_{\text{leak}} = \beta, \quad J_{\text{SSCC}}(\theta) = S\theta,$$

and

$$h_\infty(c) = \frac{k_2^2}{k_2^2 + c^2}.$$

As in previous chapters,  $c$  represents cytosolic  $\text{Ca}^{2+}$  concentration,  $h$  is a dimensionless variable denoting the proportion of IPRs that have not been inactivated and  $\theta$  is the dilation/compression of the apical surface area of a cell, which has been approximated as a linear, viscoelastic continuum. Ignoring the effect of cell boundaries, this model could be applied over the embryonic epithelial tissue, as well. The parameter  $\mu$  is taken as the bifurcation parameter, to be held at any desired value between 0 and 1, and  $J_{\text{leak}}$  is neglected since it is assumed to be small.

$J_{\text{SSCC}}$  is the stretch-activation  $\text{Ca}^{2+}$  flux due to the activated SSCCs, where the constant  $S$  represents the ‘strength’ of stretch activation.  $T_D(c)$  is the contraction stress term. The constants  $\xi_1$ ,  $\xi_2$  are the shear and bulk viscosities of the cytosol, respectively, and the constants  $E' = E/(1 + \nu)$  and  $\nu' = \nu/(1 - 2\nu)$ , where  $E$  and  $\nu$  are Young’s modulus and the Poisson ratio, respectively.

It is important to note that, although this model assumes the cell’s mechanical properties to be fixed (i.e. Young’s modulus, Poisson ratio, and viscosity are treated as constants), these properties have been found to vary significantly over space and also with the embryo’s developmental stage (Brodland et al., 2006; Luby-Phelps, 1999; Zhou et al., 2009).

#### 4.1.1 Force balance equation for a viscoelastic material

Kaouri et al. (2019) derived Equation (4.3) from the mechanical force balance equation for a linear viscoelastic material. The experimental results of Von Dassow et al. (2010) justify the approximation of embryonic tissue as a linear viscoelastic material. Assuming no external forces, the force balance equation for a Kelvin-Voigt, linear viscoelastic material can be written as follows (Landau et al., 1960; J. Murray, 2001):

$$\nabla \cdot \boldsymbol{\sigma} = 0 \Rightarrow \nabla \cdot \left( \underbrace{(\xi_1 \mathbf{e}_t + \xi_2 \theta_t \mathbf{I})}_{\text{viscous stress}} + \underbrace{E'(\mathbf{e} + \nu' \theta \mathbf{I})}_{\text{elastic stress}} - \underbrace{T_D(c) \mathbf{I}}_{\text{contraction stress}} \right) = 0, \quad (4.4)$$

where  $\boldsymbol{\sigma}$  is the stress tensor,  $\mathbf{e} = \frac{1}{2}(\nabla \mathbf{u} + \nabla \mathbf{u}^T)$  is the strain tensor,  $\mathbf{u}$  the displacement vector,  $\theta = \nabla \cdot \mathbf{u}$  is the dilation/compression of the material, and  $\mathbf{I}$  is the unit tensor. In one spatial dimension  $\mathbf{e} = e = \theta = \frac{\partial u}{\partial x}$ ; therefore, upon integrating Equation (4.4) with respect to  $x$ , we get

$$(\xi_1 + \xi_2)\theta_t + E'(1 + \nu')\theta - T_D(c) = A. \quad (4.5)$$

The constant of integration  $A = 0$  since when  $c = 0$ ,  $T_D = 0$ ,  $\theta = 0$  and  $\theta_t = 0$ . This concludes the derivation of ODE (4.3).

### 4.1.2 Nondimensionalising the ODE model

As in Kaouri et al. (2019), the mechanochemical model (Equation (4.1)-(4.3)) can be nondimensionalised using  $c = k_1 \bar{c}$  and  $t = \tau_h \bar{t}$ . After dropping the bars for notational convenience, we obtain

$$\frac{dc}{dt} = \mu h K_1 \frac{b+c}{1+c} - \frac{\Gamma c}{K+c} + \lambda \theta = R_1(c, \theta, h; \mu, \lambda), \quad (4.6)$$

$$\frac{dh}{dt} = \frac{K_2^2}{K_2^2 + c^2} - h = R_2(c, h), \quad (4.7)$$

$$\frac{d\theta}{dt} = -k_\theta \theta + \hat{T}(c) = R_3(c, \theta), \quad (4.8)$$

where  $K_1 = k_f \tau_h / k_1$ ,  $\Gamma = \gamma \tau_h / k_1$ ,  $K = k_\gamma / k_1$ , and  $\lambda = \tau_h S / k_1$  in (4.6);  $K_2 = k_2 / k_1$  in (4.7); and,  $k_\theta = \frac{\tau_h E'(1+\nu')}{(\xi_1 + \xi_2)}$  and  $T(c) = \frac{\tau_h}{(\xi_1 + \xi_2)} T_D(c)$  in (4.8).

Using the parameter values from Atri et al. (1993) (see Appendix A1, Table A1.1), it can easily be found that  $K_2 = 1$ ,  $\Gamma = 40/7 \sim 5.71$ , and  $K = 1/7$ . Taking the values of  $E$ ,  $\nu$ , and viscosity from Zhou et al. (2009) ( $E = 8.5$  Pa,  $\nu = 0.4$  and  $\xi_1 + \xi_2 = 100$  Pa.s),  $k_\theta$  was found to be approximately 0.36. Since the parameter values for  $\text{Ca}^{2+}$  dynamics are approximate, we take  $k_\theta = 1$  for simplicity. Lastly, taking  $T_D(c) = T_{0D} \hat{T}(c) \implies T(c) = \frac{\tau_h}{(\xi_1 + \xi_2)} T_{0D} \hat{T}(c)$  where  $\hat{T}(c)$  is nondimensional, we fix  $\frac{\tau_h}{(\xi_1 + \xi_2)} T_{0D} = 1$ .

The ‘strength’ of stretch activation  $\lambda$  can be thought of as a coupling parameter between  $\text{Ca}^{2+}$  signalling and mechanics. Physically, it corresponds to a combination of the structural characteristics of an SSCC. An exhaustive literature search revealed that there are no measured properties for SSCCs. Therefore,  $\lambda$  was instead taken as a bifurcation parameter. To ensure that the  $J_{\text{SSCC}}$  term is comparable in size to the other flux terms, it is prudent to take  $\lambda \leq 10$ .

### 4.1.3 Modelling the Traction stress

The cellular cytoplasm is subjected to mechanical effects by the cytoskeleton - microfilaments of protein that form a three-dimensional network. The cytosol has active contractile units, actomyosin molecules, which behave like miniature muscles and exert a contraction stress on the cytoplasm via the network. These actomyosin units are formed at very low  $\text{Ca}^{2+}$  concentrations but the network itself begins to break apart at higher concentrations of

$\text{Ca}^{2+}$ . So, the contraction effect ceases to be felt although the contractile units themselves are not destroyed (Murray & Oster, 1984).

In their models for epidermal sheets, Murray & Oster (1984) and Cruywagen & Murray (1992) modelled the cytosol as a stable gel at low  $\text{Ca}^{2+}$  concentrations and the cytoskeleton network breakdown was simulated by the solation of the gel, such that, at high  $\text{Ca}^{2+}$  concentrations, the gel is considered too solated to support any stress. In these works, the traction stress stems from the formation of the actomyosin units, and is modelled as a *sigmoidal* function of  $\text{Ca}^{2+}$ . It should be noted that they also consider the viscosity and elasticity of the gel to vary with  $\text{Ca}^{2+}$  concentration. In contrast, we assume the viscosity and elasticity to be constant in this project.

Based on the experiments conducted by Christodoulou & Skourides (2015) on the embryonic neuroepithelial cells of *Xenopus*, Kaouri et al. (2019) constructed a model where the  $\text{Ca}^{2+}$ -induced stress saturates to a nonzero level with an increase in  $\text{Ca}^{2+}$  concentration but they speculated that there might be other cell types where the cell could relax back to baseline stress. In their study of post-fertilization waves on the surface of vertebrate eggs, Lane et al. (1987) considered the cytoplasm to be a gel and modelled the traction stress as a switch from 1, at low values of  $\text{Ca}^{2+}$ , to 0, at high values of  $\text{Ca}^{2+}$ . The traction term was modelled in a similar fashion by Piechór (2013) in a study of thin viscoelastic cells. This project considers traction terms with a similar shape, however, we model the traction term to have a gradual ascent and descent, to more closely mimic a biological response.

The  $\text{Ca}^{2+}$ -induced traction stress  $\hat{T}(c)$  has been modelled as a ‘pulse’ function dependent upon only one variable, the cytosolic  $\text{Ca}^{2+}$  concentration. Kaouri et al. (2019) used the traction term  $\hat{T}(c) = \frac{\alpha c}{1 + \alpha c}$ , which is similar in form to the well known Michaelis-Menten equation, written as:

$$V(S) = V_{max} \left( \frac{K_m^{-1} S}{1 + K_m^{-1} S} \right) \quad (4.9)$$

where  $V$  is the reaction velocity,  $V_{max}$  is the maximum reaction velocity,  $S$  is substrate concentration, and  $K_m$  is the Michaelis constant.

The Michaelis constant is the value of substrate concentration which results in a reaction velocity of  $0.5V_{max}$ . This can be easily verified by setting  $\text{LHS} = 0.5V_{max}$  in Equation (4.9), and solving for  $S$ . The Michaelis constant is an indicator of how quickly  $V$  *ascends* to peak value i.e.  $K_m$  denotes the ‘scale’ of ascent of  $V$ . A low value of  $K_m$  signifies a rapid rise and vice versa. Applying this to  $\hat{T}(c) = \frac{\alpha c}{1 + \alpha c}$ , it can be seen that, in this instance, the scale of ascent is  $1/\alpha$ . The Michaelis-Menten equation shows that, upon increasing the value of  $S$ ,  $V(S)$  increases in a *hyperbolic* manner until it reaches saturation (Figure 4.2a).

The simulations in Subsection 4.1.5 and Section 4.2 were performed using different traction stresses to compare the system responses. In this project, we use two *novel* traction stress terms to model two distinct types of mechanochemical response. To generate a wide ‘pulse’ that begins its ascent at the origin, we set

$$\hat{T}(c) = T_1(W, c) = \frac{c^n}{M^n + c^n} + \frac{(c - W)^n}{M^n + (c - W)^n} H(W - c) - 1, \quad (4.10)$$

where  $H(c)$  is the *Heaviside function*,  $M > 0$  and  $n$  is an even-valued positive integer. To generate a thin pulse centred at a certain target value ( $G$ ), we set

$$\begin{aligned} \hat{T}(c) = T_2(c) &= 1 - \frac{\alpha(c - G)^n}{1 + \alpha(c - G)^n} \\ &= \frac{1}{1 + \alpha(c - G)^n}, \end{aligned} \quad (4.11)$$

where  $\alpha > 0$  and  $n$  is an even-valued positive integer.

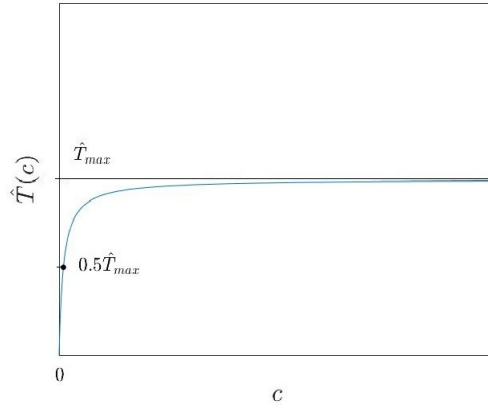
Note that the Michaelis-Menten equation is a 1<sup>st</sup> order Hill equation. Equations (4.10) & (4.11) were derived using Hill equations of order  $n$ . In both cases, only *even* values of  $n$  generate the shape of a pulse. In modelling the traction terms, it is assumed that there is no contraction in the absence of  $\text{Ca}^{2+}$ . This is realised by ensuring that  $\hat{T}(0) = 0$ .

The traction term  $\hat{T}(c) = T_1(W, c)$  produces a wide solitary ‘pulse’ (Figure 4.1b) whose width can be adjusted by tuning the parameter  $W$ . As  $c$  increases, for small  $c$ ,  $\hat{T}(c)$  increases in a *sigmoidal* manner and attains peak value at  $c = W/2$ , after which it begins its descent. Increasing the order ( $n$ ) of the function increases the ‘steepness’ of the pulse and the peak value of the pulse is given by the expression

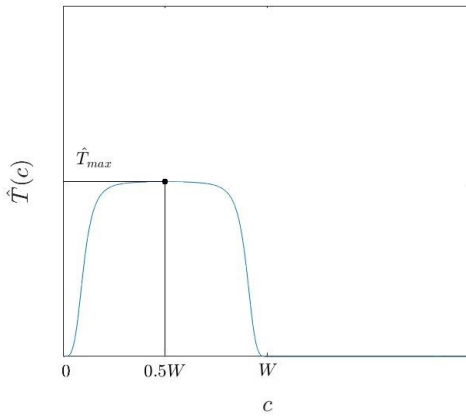
$$\begin{aligned} \hat{T}_{max} &= \hat{T}(W/2) \\ &= \frac{W^n - (2M)^n}{W^n + (2M)^n} \end{aligned}$$

The traction term  $\hat{T}(c) = T_2(c)$  has a different form compared to the Michaelis-Menten equation and produces a thin pulse-shaped function (Figure 4.1c). So, it is more meaningful to look for the ‘steepness’ of the pulse instead of a scale of ascent. To find the steepness, set  $\text{LHS} = 0.5\hat{T}_{max} = 0.5$  in Equation (4.11)

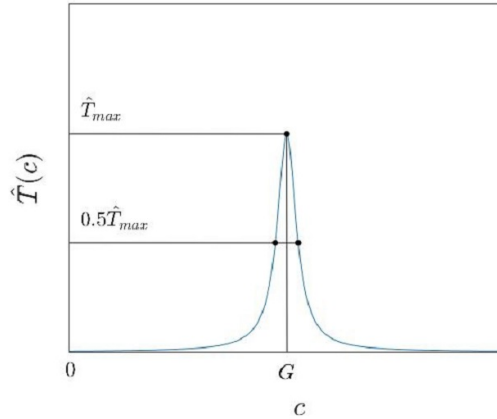
$$\begin{aligned} \implies (c - G) &= \pm(1/\alpha)^{1/n} \\ \implies c &= G \pm (1/\alpha)^{1/n} = C_{0.5} \end{aligned}$$



$$(a) \hat{T}(c) = \frac{\alpha c}{1 + \alpha c}$$



$$(b) \hat{T}(c) = T_1(W, c)$$



$$(c) \hat{T}(c) = T_2(c)$$

Figure 4.1: The shape of  $\hat{T}(c)$  for the different traction stress profiles.

*Software:* MATLAB

The steepness of the pulse is given by  $|C_{0.5} - G| = (1/\alpha)^{1/n}$ . A lower value of  $|C_{0.5} - G|$  indicates a steeper pulse and vice versa. Also, the width of the pulse  $= 2|C_{0.5} - G|$ . In modelling the pulse, it is assumed that the cells experience a contraction stress only in the vicinity of a certain target value ( $G$ ) of  $\text{Ca}^{2+}$ . If the  $\text{Ca}^{2+}$  level is significantly lower or higher than the target value, the cells will tend to return to their relaxed state. For  $\alpha > 1$ , increasing the order ( $n$ ) of the function  $\hat{T}(c)$  decreases the steepness and increases the width of the pulse; whereas, increasing the value of the coefficient  $\alpha$  increases the steepness of the pulse while decreasing its width. Because of the assumption that there is no traction stress without  $\text{Ca}^{2+}$ , it is important to choose a sufficiently high  $G$ .

#### 4.1.4 Linear stability analysis: The Hopf curve

The linear stability analysis performed in Subsection 2.4 helped identify the bifurcation regimes for the Atri model, considering only  $\mu$  as a bifurcation parameter. Similarly, a linear stability analysis must be performed for the mechanochemical model, with two bifurcation parameters -  $\mu$  and  $\lambda$ . However, the increase in complexity, owing to the inclusion of an extra bifurcation parameter, calls for the use of a visual aid - the *Hopf curve* to locate the region of parameter space that sustains oscillations. The *Hopf curve* is the locus of the Hopf bifurcation points in the  $\mu$ - $\lambda$  parametric plane. The full linear stability analysis and derivation of the *Hopf curve* can be found in Kaouri et al. (2019).

Setting the left-hand sides of Equations (4.6)-(4.8) to zero, it can be seen that the steady states of the system satisfy

$$\mu K_1 \frac{1}{1+c^2} \frac{b+c}{1+c} - \frac{\Gamma c}{K+c} + \lambda \hat{T}(c) = 0. \quad (4.12)$$

Equation (4.12) can be used to plot the system steady states as a function of  $\mu$  and  $\lambda$ .

The Jacobian of (4.6)-(4.8) is given by

$$M_1 = \begin{bmatrix} R_{1c} & R_{1h} & \lambda \\ R_{2c} & -1 & 0 \\ \hat{T}'(c) & 0 & -1 \end{bmatrix}, \quad (4.13)$$

whose characteristic polynomial can be factorised as the *cubic* equation

$$(1 + \omega)((R_{1c} - \omega)(1 + \omega) + R_{1h}R_{2c} + \lambda \hat{T}'(c)) = 0, \quad (4.14)$$

where  $\omega$  represents the eigenvalues. As one eigenvalue is always equal to -1, the system bifurcations can be studied through the *quadratic*

$$\omega^2 - (R_{1c} - 1)\omega - R_{1c} - R_{1h}R_{2c} - \lambda \hat{T}'(c) = 0. \quad (4.15)$$

To identify the  $\mu$ - $\lambda$  parameter range sustaining oscillations, we must locate the region in the  $\mu$ - $\lambda$  parameter space that gives rise to either an unstable node or an unstable spiral in the linearised system. In the full non-linear system, this instability corresponds to limit cycles. In dynamical systems, a Hopf bifurcation marks the transition from a stable node (or spiral) to an unstable node (or spiral) and vice versa. So, we seek the Hopf bifurcations in the  $\mu$ - $\lambda$  parameter space, which satisfy  $\text{Tr}(M_2) = 0$ , where

$$M_2 = \begin{bmatrix} R_{1c} & R_{1h}R_{2c} + \lambda \hat{T}'(c) \\ 1 & -1 \end{bmatrix} \quad \text{and} \quad \text{Tr}(M_2) = R_{1c} - 1.$$

Setting

$$\text{Tr}(M_2) = 0 \implies \mu(c) = \frac{(1+c^2)(1+c)^2}{K_1(1-b)} \left( 1 + \frac{\Gamma K}{(K+c)^2} \right), \quad (4.16)$$

and substituting in (4.12) we obtain

$$\lambda(c) = \frac{1}{\hat{T}(c)} \left( \frac{\Gamma c}{K+c} - \frac{(b+c)(1+c)}{1-b} \left( 1 + \frac{\Gamma K}{(K+c)^2} \right) \right). \quad (4.17)$$

Thus, the Hopf curve can be obtained for *any*  $\hat{T}(c)$  by parametrically plotting (4.16) and (4.17), taking  $c$  as the parameter. The interior of the Hopf curve corresponds to an unstable spiral and approximates the  $\mu$ - $\lambda$  parameter space sustaining oscillations (limit cycles) in the full non-linear system.

#### 4.1.5 Hopf curves for various Traction terms

Kaouri et al. (2019) considered the traction term  $\hat{T}(c) = \frac{\alpha c}{1 + \alpha c}$ , for  $\alpha = 1, 2, 10, 100$ , and  $n = 1, 2$ . Here we use traction terms which were *derived* from higher-order Hill functions. Recall the expressions for the traction terms defined in Equations (4.10) & (4.11). We assign fixed values to some of the equation parameters and rewrite  $T_1(W, c)$  and  $T_2(c)$  as follows:

$$T_1(W, c) = \frac{c^4}{0.2^4 + c^4} + \frac{(c-W)^4}{0.2^4 + (c-W)^4} H(W-c) - 1,$$

$$T_2(c) = \frac{1}{1 + 10(c-4)^2}.$$

Our goal is to select a reasonable  $\hat{T}(c)$ , in line with experimental evidence. The limited data allows us to consider various parameter choices so we choose those values that generate the most reasonable shape of  $\hat{T}(c)$ . The simulations in Section 4.2 will use the traction terms  $T_1(W, c)$  and  $T_2(c)$ , as defined above.

Some traction terms and their corresponding Hopf curves are depicted in Figures 4.2 and 4.3. The area inside the Hopf curves approximates the parameter space that yields sustained oscillations in the non-linear system. The area outside the curve could correspond to either a stable node ( $\text{Discr}(M_2) > 0$ ) or stable spiral ( $\text{Discr}(M_2) < 0$ ), where

$$\text{Discr}(M_2) = (R_{1c} - 1)^2 + 4(R_{1c} + R_{1h}R_{2c} + \lambda\hat{T}'(c)).$$

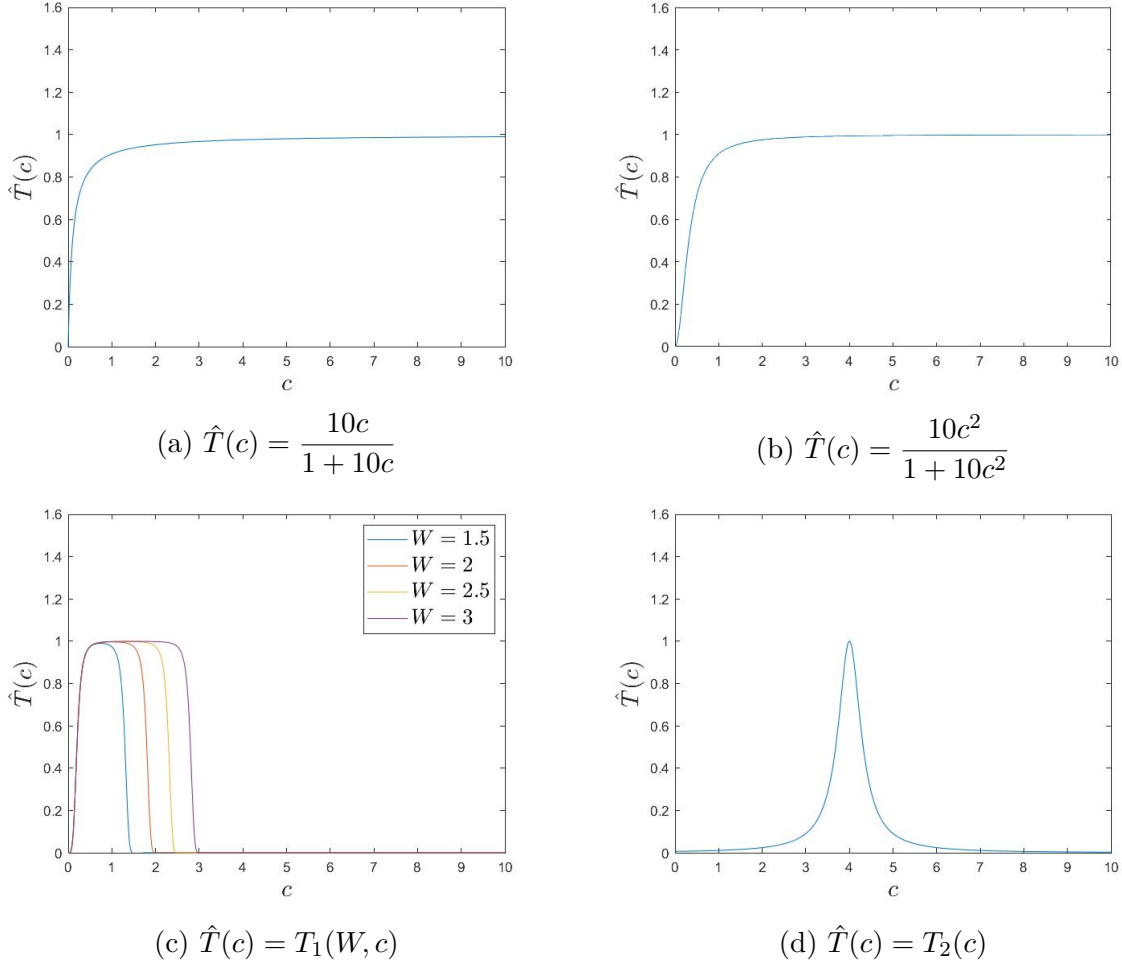


Figure 4.2: Shape of the traction stress term for different  $\hat{T}(c)$ . *Software:* MATLAB

In the case of the 2<sup>nd</sup> order Hill function, it is observed that the apex of the Hopf curve begins to loop, as can be seen in Figure 4.3b. This indicates the existence of a single  $\mu - \lambda$  pair which corresponds to two singular points of the system, both of which satisfy  $\text{Tr}(M_2) = 0$ . Upon testing with higher order Hill functions (tested up to 10<sup>th</sup> order), it was found that the loop area increased greatly with an increase in the order of the Hill function.

The shape of the Hopf curve associated with the traction term  $\hat{T}(c) = T_1(W, c)$  was found to be similar to the Hopf curve for  $\hat{T}(c) = \frac{10c}{1 + 10c}$ . It is observed that changing the value of  $W$  doesn't greatly impact the shape of the corresponding Hopf curve (Figure 4.3c). The Hopf curves for  $W = 2, 2.5, 3$  coincide, whereas the curve for  $W = 1.5$  deviates from them very slightly. As we consider higher values of  $W$ , we expect system behaviour to resemble the  $\hat{T}(c) = \frac{\alpha c}{1 + \alpha c}$  case. This was confirmed upon observing system behaviour for values of  $W > 3$ .

For the traction term  $\hat{T}(c) = \frac{1}{1 + \alpha(c - 4)^n}$ , the mechanochemical model was simulated using  $\alpha = 10$  and  $n = 2$  (Figure 4.2d). Comparing the corresponding Hopf curve (Figure 4.3d) to the ones previously discussed, it can be seen that this Hopf curve is far larger and spans a much greater range of  $\lambda$ . Increasing the amplitude of this traction term greatly diminishes the area of the Hopf curve. In effect, as the amplitude of the traction term increases, the range of  $\mu$  for which we obtain limit cycles decreases (for a constant value of  $\lambda$ ).

Hopf curves were also obtained for other values of  $\alpha$  and  $n$  (Figure 4.4) but it was found that, over the parameter space of interest:  $\lambda \in (0, 10] \cup \mu \in [0, 1]$ , the plots were practically identical.

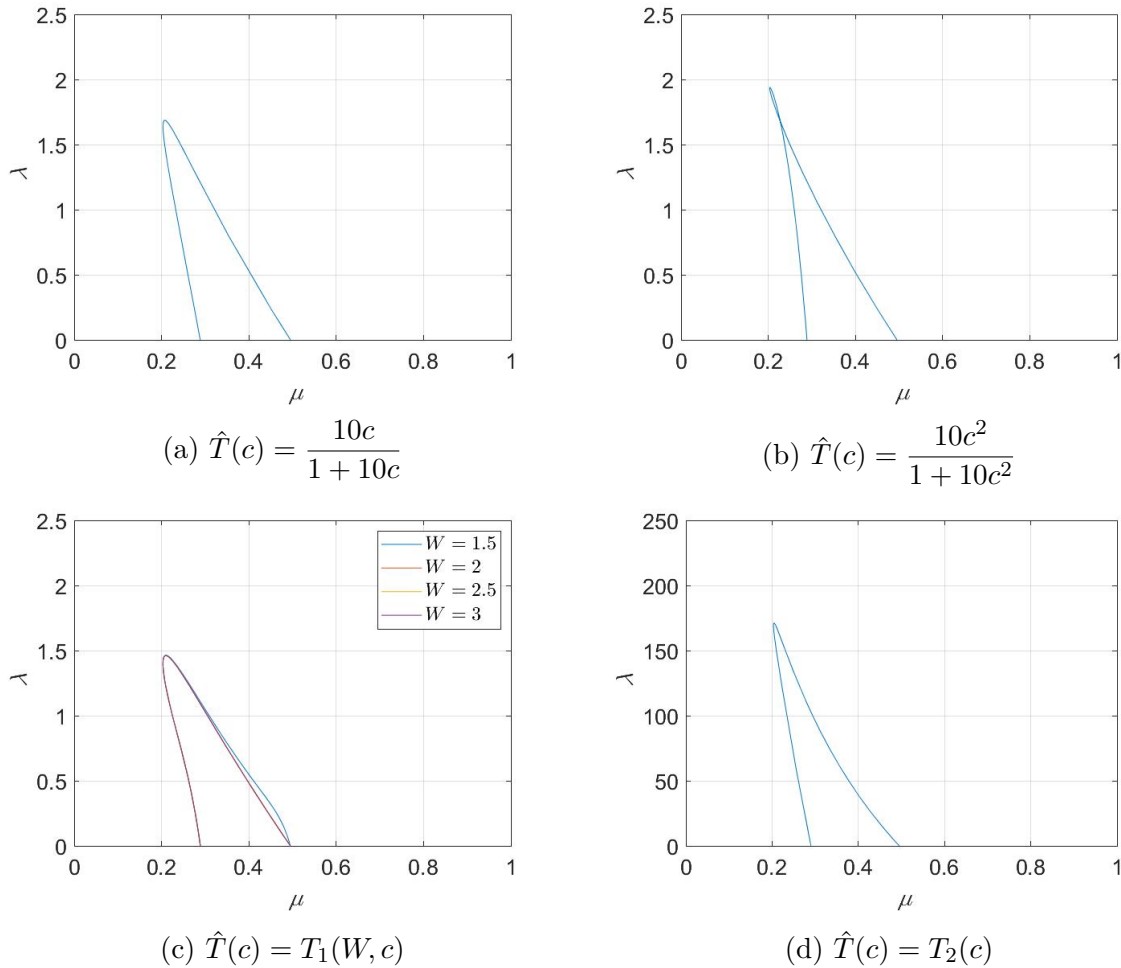


Figure 4.3: Shape of the Hopf curve for different traction terms  $\hat{T}(c)$ . *Software:* MATLAB

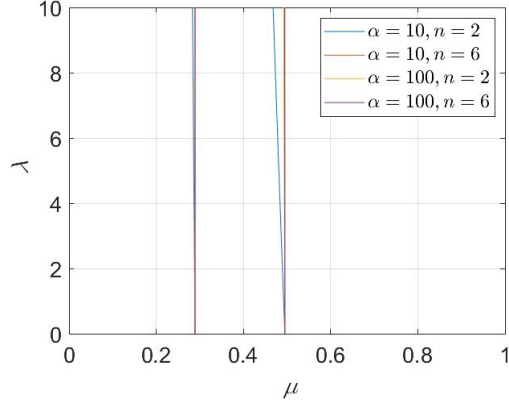


Figure 4.4: Hopf curves for  $\hat{T}(c) = \frac{1}{1 + \alpha(c - 4)^n}$  for various values of  $\alpha$  and  $n$ .  
*Software: MATLAB*

## 4.2 Simulations

To study the solution of the mechanochemical model for different bifurcation regimes, Equations (4.6)-(4.8) were solved numerically in MATLAB using the *ode45* function for the system parameters specified in Table A1.1. The initial conditions were taken as:  $c(0) = 1$ ,  $h(0) = 1$ , and  $\theta(0) = 1$ .

Initially, simulations were run for the same traction term used in Kaouri et al. (2019) and are displayed in Figure 4.6. The Hopf curve associated with that traction term is depicted in Figure 4.5 and the  $\mu$ - $\lambda$  values for which the simulations were run are depicted graphically in the parameter space.

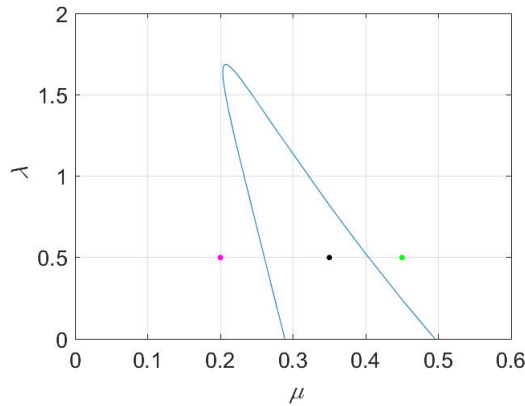


Figure 4.5: Hopf curve for the traction term  $\hat{T}(c) = \frac{10c}{1 + 10c}$ . The coloured dots depict the  $\mu$ - $\lambda$  values used for the simulations of Figure 4.6. *Software: MATLAB*

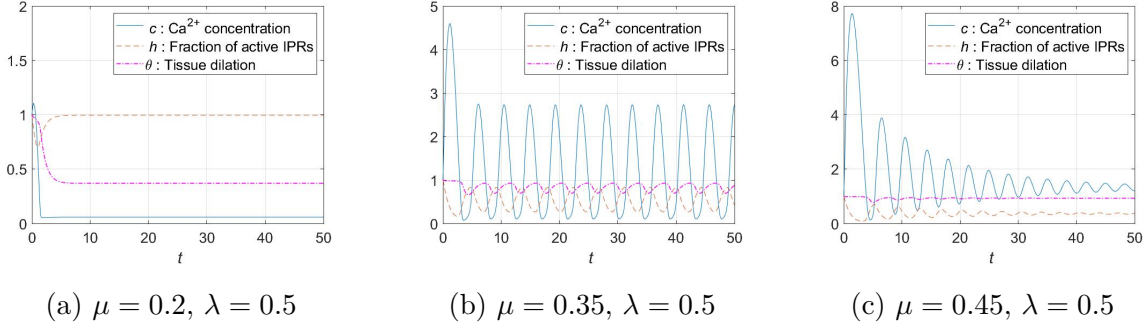


Figure 4.6: Solutions of  $c, h, \theta$  for the system (4.6)-(4.8) over  $0 \leq t \leq 50$  for various values of  $\mu$ . We fix  $\lambda = 0.5$ .  $\hat{T}(c) = \frac{10c}{1 + 10c}$ . *Software: MATLAB*

$\mu = 0.2, \lambda = 0.5$ : The system rapidly reaches steady state (Figure 4.6a). This is in accordance with our expectations because, in Figure 4.5, the point  $(\mu = 0.2, \lambda = 0.5)$  lies to the left of the area enclosed by the Hopf curve in  $\mu$ - $\lambda$  parameter space, and corresponds to a *stable node*.

$\mu = 0.35, \lambda = 0.5$ : The system exhibits limit cycles (Figure 4.6b). The point  $(\mu = 0.35, \lambda = 0.5)$  lies within the area enclosed by the Hopf curve and corresponds to an *unstable spiral*. This instability results in *limit cycles* in the full non-linear system. It can be seen that the oscillations in  $\theta$  have the *same frequency* as the oscillations in  $c$ .

$\mu = 0.45, \lambda = 0.5$ : The system oscillations are observed to die out over time (Figure 4.6c). The point  $(\mu = 0.45, \lambda = 0.5)$  lies to the right of the Hopf curve and corresponds to a *stable spiral*. The oscillations in  $\theta$  are noted to be of negligible amplitude.

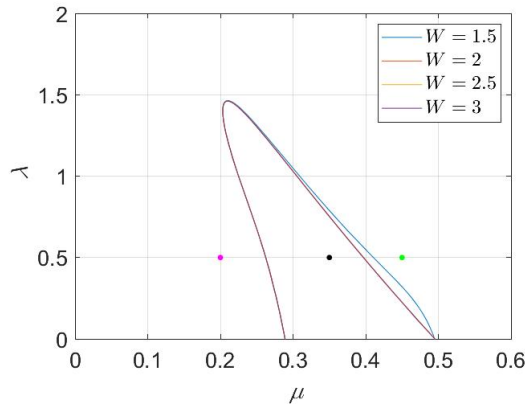


Figure 4.7: Hopf curves for the traction term  $\hat{T}(c) = T_1(W, c)$ , for different values of  $W$ . The coloured dots depict the  $\mu$ - $\lambda$  values used for the simulations of Figure 4.8.

*Software: MATLAB*

Figure 4.8 depicts system behaviour for the traction term  $\hat{T}(c) = T_1(W, c)$ . The coloured dots on the corresponding Hopf curve (Figure 4.7) denote the combinations of bifurcation parameters ( $\mu$  and  $\lambda$ ) used for the simulations. The points were chosen to represent different bifurcation regimes, in order to observe the qualitative changes in system behaviour.

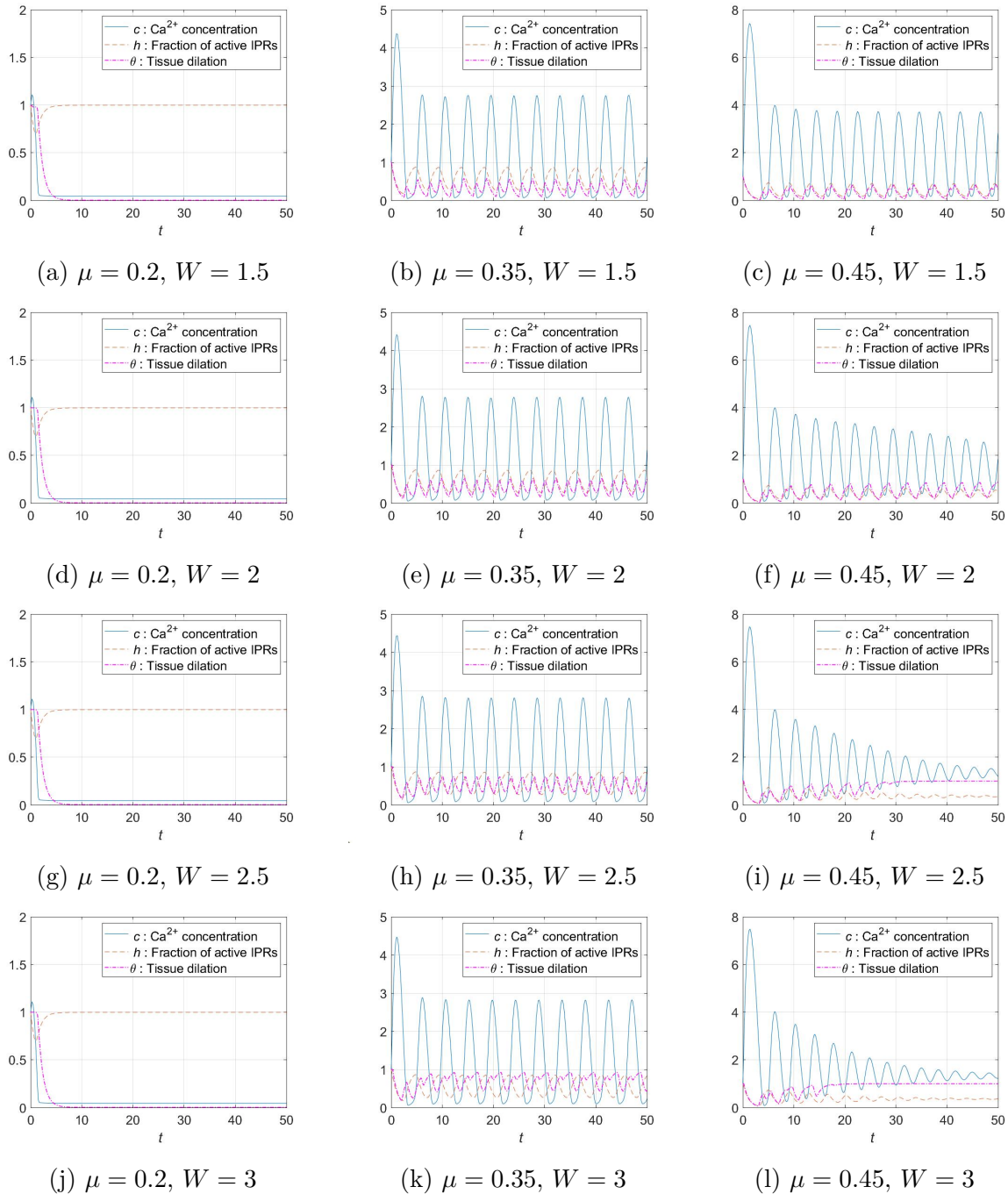


Figure 4.8: Solutions of  $c$ ,  $h$ ,  $\theta$  for the system (4.6)-(4.8) over  $0 \leq t \leq 50$  for various values of  $W$  and  $\mu$ . We fix  $\lambda = 0.5$ .  $\hat{T}(c) = T_1(W, c)$ . *Software*: MATLAB

$\mu = 0.2, \lambda = 0.5$ : The system rapidly reaches steady state (Figures 4.8a, 4.8d, 4.8g & 4.8j). This behaviour is to be expected because the point  $(\mu = 0.2, \lambda = 0.5)$  lies to the left of the area enclosed by the Hopf curve (Figure 4.7) and corresponds to a *stable node*. Upon closer inspection, it was observed that changing  $W$  only produced a very minute change (in the order of  $10^{-6}$ ) in the steady state values of  $c$ ,  $h$  and  $\theta$ .

$\mu = 0.35, \lambda = 0.5$ : The system exhibits *limit cycles* (Figures 4.8b, 4.8e, 4.8h & 4.8k). The point  $(\mu = 0.35, \lambda = 0.5)$  lies within the area enclosed by the Hopf curve (Figure 4.7) and corresponds to an *unstable spiral*. It can be observed that the oscillations in  $\theta$  occur at *twice the frequency* of the oscillations in  $c$ .

During each individual spike in  $\text{Ca}^{2+}$  ( $c$ ), we see two spikes in the value of  $\theta$ . In Figure 4.8b, a short spike is followed by one of greater amplitude. In Figures 4.8e & 4.8h, the two spikes are of equal amplitude. And, in Figure 4.8k, the two spikes have begun to merge.

$\mu = 0.45, \lambda = 0.5$ : We expect the system to exhibit decaying oscillations in  $c$ ,  $h$ , and  $\theta$  as the point  $(\mu = 0.45, \lambda = 0.5)$  lies to the right of the area enclosed by the Hopf curve (Figure 4.7) and corresponds to a *stable spiral*. This behaviour is observed in Figures 4.8f, 4.8i & 4.8l. However, in Figure 4.8c, we observe that the system displays sustained oscillations. A likely explanation for this occurrence could be that the point  $(\mu = 0.45, \lambda = 0.5)$  lies comparatively close to the Hopf curve for  $W = 1.5$ . Because of this proximity to the bifurcation point, the system exhibits sustained oscillations rather than decaying ones.

Thus, it can be seen that although the Hopf curves for  $W = 1.5, 2, 2.5, 3$  appear very similar, the corresponding non-linear systems exhibit significantly different behaviour.

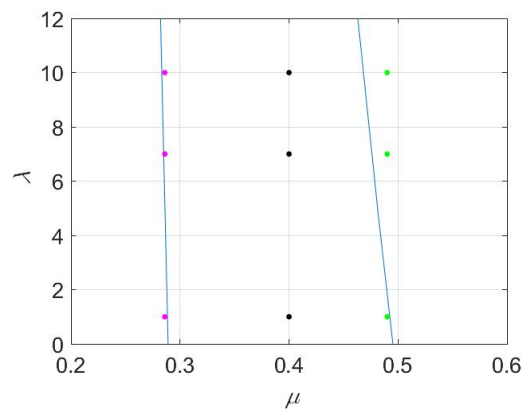


Figure 4.9: Hopf curve for the traction term  $\hat{T}(c) = T_2(c)$ . The coloured dots depict the  $\mu$ - $\lambda$  values used for the simulations of Figure 4.10. *Software*: MATLAB

Figure 4.10 depicts system behaviour for the traction term  $\hat{T}(c) = T_2(c)$ . With the aid of the Hopf curve (Figure 4.9), we select combinations of the bifurcation parameters ( $\mu$  and  $\lambda$ ) corresponding to different bifurcation regimes, to observe qualitative changes in system behaviour.

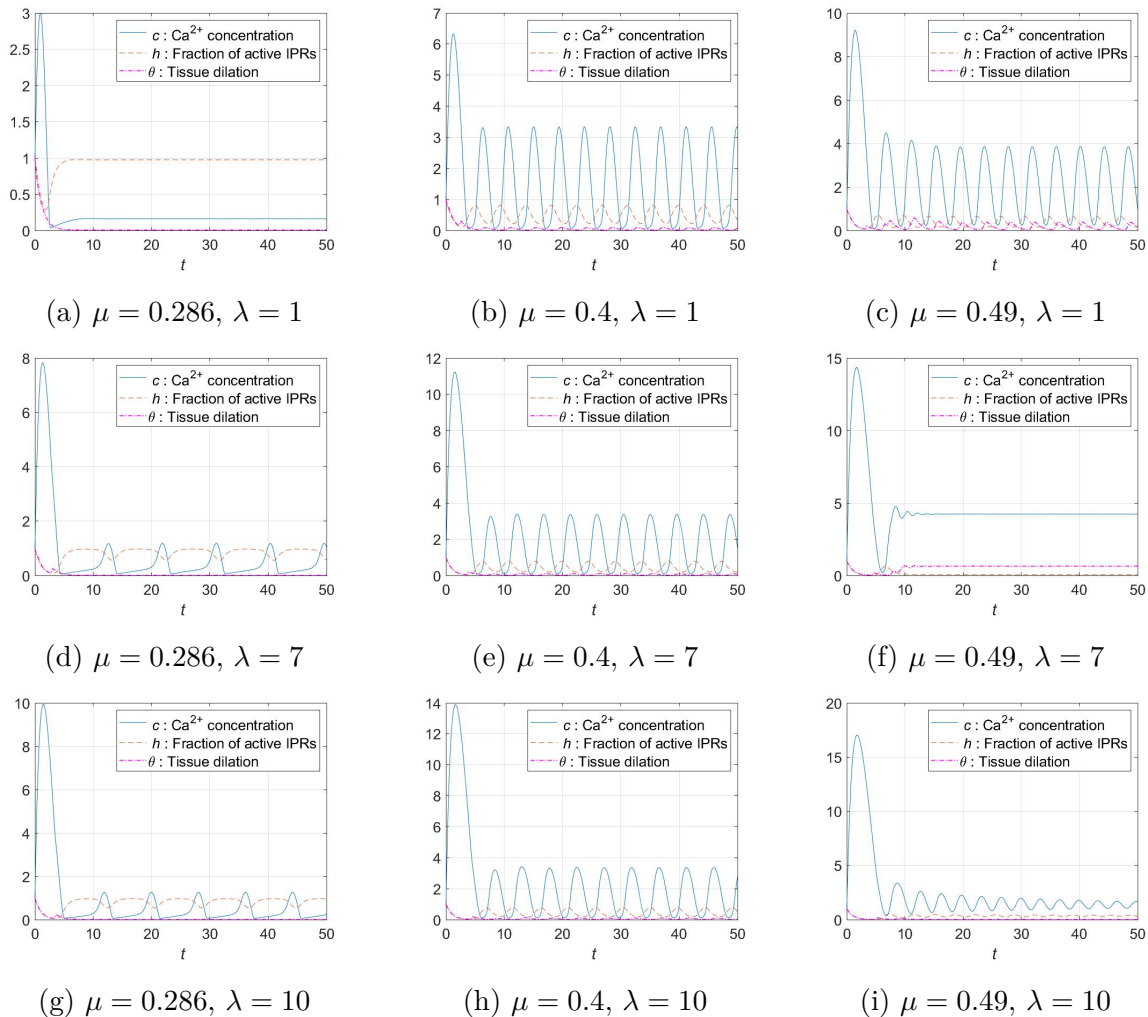


Figure 4.10: Solutions of  $c, h, \theta$  for the system (4.6)-(4.8) over  $0 \leq t \leq 50$  for various values of  $\lambda$  and  $\mu$ .  $\hat{T}(c) = T_2(c)$ . *Software*: MATLAB

- *Outside the Hopf curve - Left area*

$\mu = 0.286, \lambda = 1$ : System has only one equilibrium point - stable spiral. In Figure 4.10a, the system quickly decays to steady state. Due to the chosen initial conditions, the system starts out in the vicinity of the equilibrium point and reaches it without much overshoot or oscillation.

- *Inside the Hopf curve*

In cases where the system has three equilibrium points i.e. Equation (4.12) has three positive real roots, it is to be understood that the system has undergone *Hopf bifurcation* for the smallest root ( $c_{St}$ ). Generally, for any combination of  $\mu$ - $\lambda$ , the equilibrium points for this system were found to be:  $c_{St} \approx 1, \approx 3$  and  $\approx 4$ ,  $h_{St} \in [0, 1]$ ,  $\theta_{St} \in [0, 1]$ . So,  $c = 1, h = 1, \theta = 1$  has been chosen as the initial condition, to ensure that the system starts out in proximity to the equilibrium point corresponding to  $c_{St} \approx 1$ .

$\mu = 0.286, \lambda = 7 \ \& \ 10$ : System has three equilibrium points - one unstable spiral, one saddle point and, one stable spiral. The appearance of the saddle point along with an additional equilibrium point implies that the system has undergone a *Fold bifurcation* at some point ( $\mu = 0.286, 1 < \lambda < 7$ ). In Figures 4.10d & 4.10g, we observe limit cycles (in  $c$  and  $h$ ) of small amplitude and frequency because these  $\mu$ - $\lambda$  pairs are situated very close to the Hopf curve. From Figure 2.3, it can be recalled that limit cycles have low amplitude and frequency near the Hopf bifurcation point. However, it can be seen that  $\theta = 0$  over the runtime of the simulations.

$\mu = 0.4, \lambda = 1$ : System has only one equilibrium point - unstable spiral. In Figure 4.10b, the system exhibits limit cycles as expected but the oscillations in  $\theta$  are of negligible amplitude.

$\mu = 0.4, \lambda = 7 \ \& \ 10$ : System has three equilibrium points - one unstable spiral, one saddle point and, one stable spiral. Across the three Figures 4.10b, 4.10e & 4.10h, the system exhibits limit cycles having roughly the same amplitude and frequency. It would seem that  $\lambda$  does not exert a significant influence on the characteristics of the limit cycles. However, these limit cycles have greater amplitude and frequency than the ones in Figures 4.10d & 4.10g. From Figure 2.3, it can be recalled that following the Hopf bifurcation, after an initial steep rise, frequency increases very gradually with  $\mu$ ; however, amplitude rises sharply with increasing  $\mu$ .

$\mu = 0.49, \lambda = 1$ : System has only one equilibrium point - unstable spiral. In Figure 4.10c, the system exhibits limit cycles having noticeably greater amplitude than the limit cycles for  $\mu = 0.4$ . The oscillations in  $\theta$  have acquired a *significantly greater amplitude* compared to the previous cases, and are noted to be of *similar frequency* to the oscillations in  $c$  and  $h$ .

- *Outside the Hopf curve - Right area*

$\mu = 0.49, \lambda = 7$ : System has three equilibrium points - one stable spiral (at  $c = 1.33, h = 0.36, \theta = 0.01$ ), one saddle point and, one stable spiral (at  $c = 4.23, h =$

0.05,  $\theta = 0.65$ ). In Figure 4.10f, the system starts at  $c = 1$ ,  $h = 1$ ,  $\theta = 1$  and, following a substantial overshoot in  $c$ , settles down rapidly at the equilibrium point  $c = 4.23$ ,  $h = 0.05$ ,  $\theta = 0.65$  without displaying noticeable oscillatory behaviour. It was intended that the system would move towards the equilibrium point at  $c = 1.33$ ,  $h = 0.36$ ,  $\theta = 0.01$ ; however, in this case, the initial conditions placed the system in a phase trajectory that caused it to migrate towards the equilibrium point at  $c = 4.23$ ,  $h = 0.05$ ,  $\theta = 0.65$  instead.

$\mu = 0.49$ ,  $\lambda = 10$ : System has three equilibrium points - one stable spiral (at  $c = 1.34$ ,  $h = 0.36$ ,  $\theta = 0.01$ ), one saddle point and, one stable spiral (at  $c = 4.34$ ,  $h = 0.05$ ,  $\theta = 0.46$ ). In Figure 4.10i, the system starts at  $c = 1$ ,  $h = 1$ ,  $\theta = 1$  and, following an initial overshoot in  $c$ , we observe oscillations about the equilibrium point  $c = 1.34$ ,  $h = 0.36$ ,  $\theta = 0.01$ , that die out over time.

When comparing Figures 4.6, 4.8 & 4.10, we see that the limit cycles of  $\theta$  have the greatest amplitude in the case of Figure 4.8 - corresponding to the traction term  $T_1(W, c)$ .

In Figure 4.8, for the cases where  $\mu = 0.35$  and  $\lambda = 0.5$ , it was noted that the spikes in  $\theta$  began to merge upon increasing the value of  $W$ . And, in Figure 4.10, for the bifurcation parameters  $\mu = 0.49$ ,  $\lambda = 1$ , it was observed that the limit cycles in  $\theta$  had greater amplitude as compared to the instances of  $\mu = 0.4$ ,  $\lambda = 1, 7$ . These behaviours can be understood by visualising the shape of the respective traction terms.

For  $\hat{T}(c) = \frac{10c}{1+10c}$ : In Figure 4.6b, while executing limit cycles,  $0 < c < 2.75$ . In a plot of  $\hat{T}(c)$  versus  $c$ , this range of  $c$  corresponds to  $0 < \hat{T}(c) < 1$ . Hence, we get limit cycles of noticeable amplitude in  $\theta$ .

For  $\hat{T}(c) = T_1(W, c)$ : In Figures 4.8b, 4.8e, 4.8h & 4.8k, while executing limit cycles,  $0 < c < 2.75$ . Considering the shape of  $T_1(W, c)$ , it can be recalled that as  $c$  is increased from 0,  $\hat{T}(c)$  goes through a cycle - rising steeply, reaching a plateau, and then falling back to 0. This generates the shape of a wide ‘pulse’ whose width is determined by  $W$ . For each spike in  $c$ ,  $\hat{T}(c)$  goes through this cycle twice - starting at the rising edge of the  $\text{Ca}^{2+}$  spike and then, again, on the falling edge. This generates two spikes in  $\theta$  for a single spike in  $c$ . As  $W$  is increased, the two spikes in  $\theta$  begin to merge because  $\hat{T}(c)$  is unable to complete the full cycle.

The behavioural transition observed in Figures 4.8f & 4.8i can be explained similarly. For  $\mu = 0.45$  and  $\lambda = 0.5$ , as we increase  $W$  from 2 to 2.5, it is seen that the oscillations in  $\theta$  stop suddenly near  $t = 30$ . This occurs because the concurrent  $\text{Ca}^{2+}$  oscillations fall within the range  $1 < c < 2.5$ , which corresponds to the plateau of  $\hat{T}(c)$ . Thus, the range of the  $\text{Ca}^{2+}$  oscillations can influence the characteristics of the  $\theta$  oscillations.

For  $\hat{T}(c) = T_2(c)$ : In Figures 4.10b, 4.10e & 4.10h, while executing limit cycles,  $0 < c < 3.5$ . In a plot of  $\hat{T}(c)$  versus  $c$ , it can be seen that  $\hat{T}(c)$  has non-zero values only in the vicinity of  $c = 4$  so, this range of  $c$  corresponds to  $\hat{T}(c) \approx 0$ . Hence, the limit cycles in  $\theta$  are almost imperceptible. In Figure 4.10c, while executing limit cycles,  $0 < c < 4$ . In this range, we can get  $0 < \hat{T}(c) < 1$ . Hence, we get limit cycles of noticeable amplitude in  $\theta$ .

In this chapter, we presented a mechanochemical ODE model which extends the Atri model from Chapter 2. After examining the relevant literature, we modelled two *novel* terms for traction stress, simulated the mechanochemical model and compared the behaviour for both terms. Using the simulation results, we compared the  $\text{Ca}^{2+}$  oscillations and mechanical oscillations across different  $(\mu-\lambda)$  bifurcation regimes. To conclude, it can be said that the shape and ascent of the traction term can greatly influence cell, and tissue, contractions.

# Chapter 5

## The Mechanochemical model with diffusion (1D)

In Chapter 4 we presented a mechanochemical model that examines the interplay of  $\text{Ca}^{2+}$  dynamics and tissue dilation/contraction (Kaouri et al., 2019). In this chapter, we add  $\text{Ca}^{2+}$  diffusion effects to augment the mechanochemical model and investigate the effects of  $\text{Ca}^{2+}$  diffusion in mechanical waves.

### 5.1 Adding $\text{Ca}^{2+}$ diffusion to the mechanochemical model

The mechanochemical model (4.1)-(4.3) is extended by adding a cytosolic diffusion term for  $\text{Ca}^{2+}$ . It is assumed that  $\text{Ca}^{2+}$  diffuses with a constant diffusion coefficient and the boundary effects between adjacent cells are neglected. The spatially extended mechanochemical model is given by:

$$\frac{\partial c}{\partial t} = D_c \frac{\partial^2 c}{\partial x^2} + J_{\text{channel}}(c, h) - J_{\text{pump}}(c) + J_{\text{leak}} + J_{\text{SSCC}}(\theta), \quad (5.1)$$

$$\tau_h \frac{\partial h}{\partial t} = h_{\infty}(c) - h, \quad (5.2)$$

$$\frac{\partial \theta}{\partial t} = -\frac{E'(1 + \nu')}{(\xi_1 + \xi_2)} \theta + \frac{1}{(\xi_1 + \xi_2)} T_D(c), \quad (5.3)$$

where

$$J_{\text{channel}}(c, h) = k_{\text{flux}} \mu h \frac{bk_1 + c}{k_1 + c}, \quad J_{\text{pump}}(c) = \frac{\gamma c}{k_{\gamma} + c}, \quad J_{\text{leak}} = \beta, \quad J_{\text{SSCC}}(\theta) = S\theta,$$

and

$$h_{\infty}(c) = \frac{k_2^2}{k_2^2 + c^2}.$$

Again,  $c$  represents cytosolic  $\text{Ca}^{2+}$  concentration,  $h$  is a dimensionless variable denoting the proportion of IPRs that have not been inactivated, and  $\theta$  is the dilation/compression of the apical surface area of the cells that make up the embryonic epithelial tissue - which is approximated as a linear, viscoelastic continuum.

Focusing our attention to one-dimensional geometry, we nondimensionalise the spatially extended mechanochemical model following the same procedure as in Subsection 4.1.2. Once again, we set  $c = k_1 \bar{c}$ ,  $t = \tau_h \bar{t}$ ,  $x = l \bar{x}$ , and neglect  $J_{\text{leak}}$  since it is assumed to be small. Dropping bars for notational convenience, we obtain

$$\frac{\partial c}{\partial t} = D_o \frac{\partial^2 c}{\partial x^2} + \mu h K_1 \frac{b+c}{1+c} - \frac{\Gamma c}{K+c} + \lambda \theta = R_1(c, \theta, h; \mu, \lambda), \quad (5.4)$$

$$\frac{\partial h}{\partial t} = \frac{K_2^2}{K_2^2 + c^2} - h = R_2(c, h), \quad (5.5)$$

$$\frac{\partial \theta}{\partial t} = -k_\theta \theta + \hat{T}(c) = R_3(c, \theta), \quad (5.6)$$

where  $K_1 = k_f \tau_h / k_1$ ,  $\Gamma = \gamma \tau_h / k_1$ ,  $K = k_\gamma / k_1$ , and  $\lambda = \tau_h S / k_1$  in (5.4);  $K_2 = k_2 / k_1$  in (5.5); and,  $k_\theta = \frac{\tau_h E'(1 + \nu')}{(\xi_1 + \xi_2)}$  and  $T(c) = \frac{\tau_h}{(\xi_1 + \xi_2)} T_D(c)$  in (5.6).

In Equation (5.4),  $D_o = D_c \tau_h / l^2$ . Taking  $l = 20 \mu m$  and using the parameter values of Atri et al. (1993) (see Appendix A1, Table A1.1), we have  $K_2 = 1$ ,  $\Gamma = 40/7 \sim 5.71$ ,  $K = 1/7$ , and  $D_o = 0.1$ . Also, we assume  $k_\theta = 1$  and fix  $\frac{\tau_h}{(\xi_1 + \xi_2)} T_{0D} = 1$  (Kaouri et al., 2019). As in Subsection 4.1.2,  $\mu$  and  $\lambda$  are taken as *bifurcation parameters* with  $\mu \in (0, 1]$  and  $\lambda \in (0, 10]$ . In line with Chapter 4, the simulations in the following section will be performed for the same traction terms used in Section 4.2. To recap, the expressions are:

$$T_1(W, c) = \frac{c^4}{0.2^4 + c^4} + \frac{(c - W)^4}{0.2^4 + (c - W)^4} H(W - c) - 1,$$

$$T_2(c) = \frac{1}{1 + 10(c - 4)^2}.$$

## 5.2 Simulations

To study the spatiotemporal evolution of the spatially extended mechanochemical model for different bifurcation regimes, Equations (5.4)-(5.6) were solved numerically in MATLAB using the *pdepe* function for the system parameters specified in Table A1.1, over a domain size of  $1000 \mu m$  (i.e.  $-25 \leq x \leq 25$  in nondimensional units). As in Section 3.3, we consider a  $\text{Ca}^{2+}$  wave diffusing outward over 20 cells placed side by side. Because we ignore the effects of the cell boundaries, we apply no flux boundary conditions (Equations (5.7)-(5.12)).

$$c_x(-25, t) = 0 \quad (5.7)$$

$$c_x(25, t) = 0 \quad (5.8)$$

$$h_x(-25, t) = 0 \quad (5.9)$$

$$h_x(25, t) = 0 \quad (5.10)$$

$$\theta_x(-25, t) = 0 \quad (5.11)$$

$$\theta_x(25, t) = 0 \quad (5.12)$$

Equations (5.13)-(5.15) are assumed to be the initial conditions of the system. They represent a perturbation in  $c$  at the centre of the domain, with all other spatial points taken to be at the steady state values of  $c$ ,  $h$ , and  $\theta$  -  $c_{St}$ ,  $h_{St}$ , and  $\theta_{St}$  respectively. The spatially independent steady state values  $c_{St}$ ,  $h_{St}$ , and  $\theta_{St}$  are determined by neglecting the diffusion term and setting LHS = 0 in Equations (5.4)-(5.6), as in Kaouri et al. (2019). We determine the steady state values by numerically solving Equation (4.12) and set up the initial conditions as follows:

$$c(x, 0) = c_{St} + 4 \exp(-50x^2), \quad (5.13)$$

$$h(x, 0) = h_{St} = \frac{1}{1 + c_{St}^2}, \quad (5.14)$$

$$\theta(x, 0) = \theta_{St} = \hat{T}(c_{St}). \quad (5.15)$$

In Chapter 4, the Hopf curves helped identify the combination of bifurcation parameters which would produce limit cycles in the mechanochemical ODE model (Figure 4.3). For the PDE model, we can expect the system to undergo bifurcations at *approximately* the same values of  $(\mu, \lambda)$  due to the small effect of diffusion. Thus, the simulations were performed for various  $\mu$ - $\lambda$  pairs, representative of different bifurcation regimes, so that we could observe qualitative changes in the system's behaviour in the presence of diffusion.

In the case of the traction terms  $\hat{T}(c) = \frac{10c}{1 + 10c}$  and  $\hat{T}(c) = T_1(W, c)$ , the simulations have been performed for the same pairs of  $(\mu, \lambda)$  as in Chapter 4 to easily compare the mechanochemical ODE and PDE models. For  $\hat{T}(c) = T_2(c)$ , we are interested in observing how the behaviour transitions from solitary pulses to periodic wavetrains, as the system undergoes a Hopf bifurcation upon changing the values of  $\mu$  and  $\lambda$ . So, we choose different values of  $\mu$ , as compared to Chapter 4, and select  $(\mu, \lambda)$  pairs that lie very close to the Hopf curve, in the parametric plane. We take the same values of  $\lambda$  as in Figure 4.10.

In Subsection 4.1.4, we established that the Hopf curve could be obtained for a traction term  $\hat{T}(c)$  by parametrically plotting (4.16) and (4.17), taking  $c$  as the parameter. In the

case of the ODE model, the interior of the Hopf curve corresponds to an unstable spiral and approximates the  $\mu$ - $\lambda$  *parameter space* sustaining oscillations (limit cycles) in the non-linear system. We utilize the same method to obtain the Hopf curve here. However, we take cognizance of the fact that the added diffusion term will have an effect on the approximation of this parameter space.

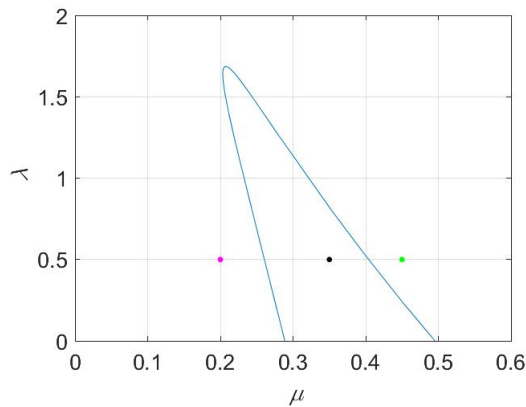


Figure 5.1: Hopf curve for the traction term  $\hat{T}(c) = \frac{10c}{1+10c}$ . The coloured dots depict the  $\mu$ - $\lambda$  values used for the simulations of Figures 5.2 & 5.3. *Software: MATLAB*

As in Chapter 4, initial simulations were run for the traction term  $\hat{T}(c) = \frac{10c}{1+10c}$  (Kaouri et al., 2019). The solutions for this system are displayed in Figures 5.2 & 5.3. The Hopf curve associated with this traction term is depicted in Figure 5.1 and the  $\mu$ - $\lambda$  values for which the simulations were run are depicted graphically in the parameter space. These values were chosen to represent different bifurcation regimes, in order to observe the qualitative changes in system behaviour. Figure 5.2 depicts the behaviour of the system in terms of  $\text{Ca}^{2+}$  waves.

$\mu = 0.2, \lambda = 0.5$ : The initial pulse rapidly decays to steady state (Figure 5.2a) as expected from Figure 4.6a.

$\mu = 0.35, \lambda = 0.5$ : A periodic wavetrain is observed in the vicinity of  $x = 0$  (Figure 5.2b). Analogous to the limit cycles seen in Figure 4.6b.

$\mu = 0.45, \lambda = 0.5$ : The initial pulse triggers oscillations which die out with time (Figure 5.2c), at the point of origin. Analogous to Figure 4.6c.

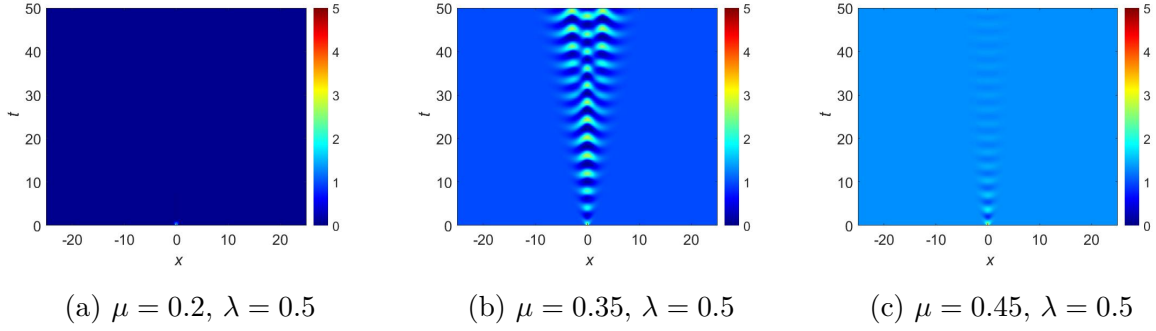


Figure 5.2:  $\text{Ca}^{2+}$  concentration ‘ $c$ ’ over the domain  $-25 \leq x \leq 25$  for  $0 \leq t \leq 50$  generated as solutions of the system (5.4)-(5.15) for  $\hat{T}(c) = \frac{10c}{1+10c}$ , over a range of  $\mu$  and  $\lambda$ .  
*Software: MATLAB*

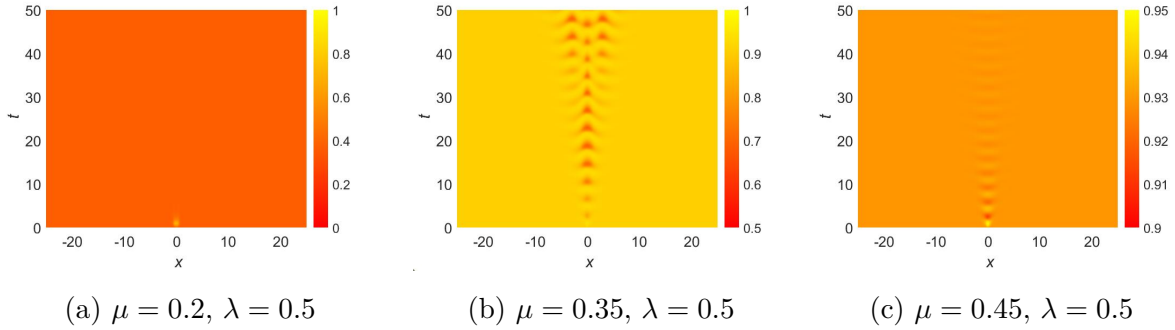


Figure 5.3: Tissue dilation ‘ $\theta$ ’ over the domain  $-25 \leq x \leq 25$  for  $0 \leq t \leq 50$  generated as solutions of the system (5.4)-(5.15) for  $\hat{T}(c) = \frac{10c}{1+10c}$ , over a range of  $\mu$  and  $\lambda$ .  
*Software: MATLAB*

Figure 5.3 depicts the behaviour of the same system in terms of mechanical waves - tissue dilations. Comparing Figures 5.2 & 5.3, it can be seen that the mechanical wave pattern matches that of the  $\text{Ca}^{2+}$  waves due to the coupling of Equations (5.4) & (5.6). From Figure 5.4, it can be seen that the mechanical waves have the *same frequency* as the  $\text{Ca}^{2+}$  waves and that they have a much smaller amplitude than the  $\text{Ca}^{2+}$  waves, similar to the mechanochemical system (Figure 4.6b). Here, a key difference is noted between the ODE and PDE systems. In the former, the  $\text{Ca}^{2+}$  oscillations had a constant amplitude whereas, in the latter, the amplitude is varying periodically with time. In both cases, however, the oscillations in  $\theta$  appear to be of constant amplitude.

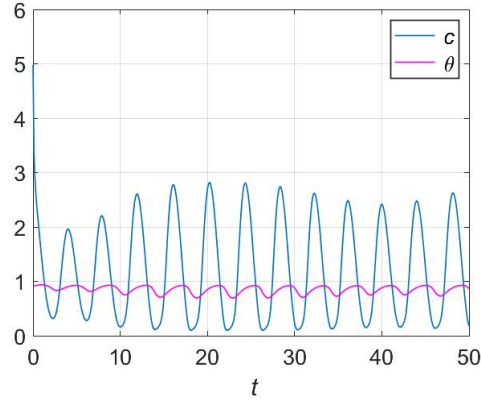


Figure 5.4: Time evolution of  $c$  and  $\theta$  at  $x = 0$ . Solutions of the system (5.4)-(5.15) for the traction term  $\hat{T}(c) = \frac{10c}{1 + 10c}$ . We fix  $\mu = 0.35$  and  $\lambda = 0.5$ . *Software:* MATLAB

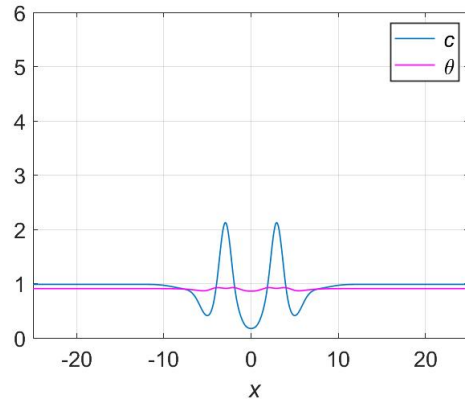


Figure 5.5: Spatial distribution of  $c$  and  $\theta$  at  $t = 50$ . Solutions of the system (5.4)-(5.15) for the traction term  $\hat{T}(c) = \frac{10c}{1 + 10c}$ . We fix  $\mu = 0.35$  and  $\lambda = 0.5$ . *Software:* MATLAB

Figure 5.4 depicts the evolution of  $c$  and  $\theta$  with time at point  $x = 0$ . Figure 5.5 depicts the distribution of  $c$  and  $\theta$  over the domain at time  $t = 50$ . These plots can be visualised as slices taken from Figures 5.2b & 5.3b along the lines  $x = 0$  and  $t = 50$ , respectively.

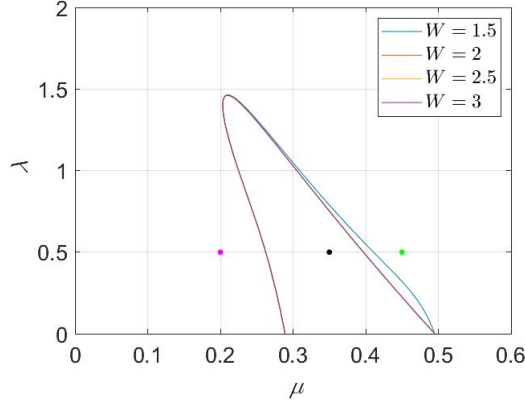


Figure 5.6: Hopf curve for the traction term  $\hat{T}(c) = T_1(W, c)$ . The coloured dots depict the  $\mu$ - $\lambda$  values used for the simulations of Figures 5.7 & 5.8. *Software: MATLAB*

Figure 5.6 depicts the Hopf curve for the traction term  $\hat{T}(c) = T_1(W, c)$ . The coloured dots denote the combinations of bifurcation parameters ( $\mu$  and  $\lambda$ ) used for the simulations. We choose the same combination of bifurcation parameters as in Figure 5.1 for ease of comparison between the traction terms  $\hat{T}(c) = \frac{10c}{1+10c}$  and  $\hat{T}(c) = T_1(W, c)$ . Figures 5.7 & 5.8 depict system behaviour in terms of  $\text{Ca}^{2+}$  waves and mechanical waves, respectively, for the traction term  $\hat{T}(c) = T_1(W, c)$ .

$\mu = 0.2, \lambda = 0.5$ : The initial pulse rapidly decays to steady state (Figures 5.7a, 5.7d, 5.7g & 5.7j) as expected from Figures 4.8a, 4.8d, 4.8g & 4.8j.

$\mu = 0.35, \lambda = 0.5$ : A periodic wavetrain is observed in the vicinity of  $x = 0$  (Figures 5.7b, 5.7e, 5.7h & 5.7k). Analogous to the limit cycles seen in Figures 4.8b, 4.8e, 4.8h & 4.8k.

$\mu = 0.45, \lambda = 0.5$ : The initial pulse triggers oscillations which die out with time, at the point of origin (Figures 5.7c, 5.7f, 5.7i & 5.7l). For  $W = 2, 2.5$  &  $3$ , this is analogous to Figures 4.8f, 4.8i & 4.8l respectively. In the case of  $W = 1.5$ , Figure 4.8c displayed sustained oscillations whereas, in Figure 5.7c, we observe dying oscillations. Possibly, this discrepancy arises due to diffusion.

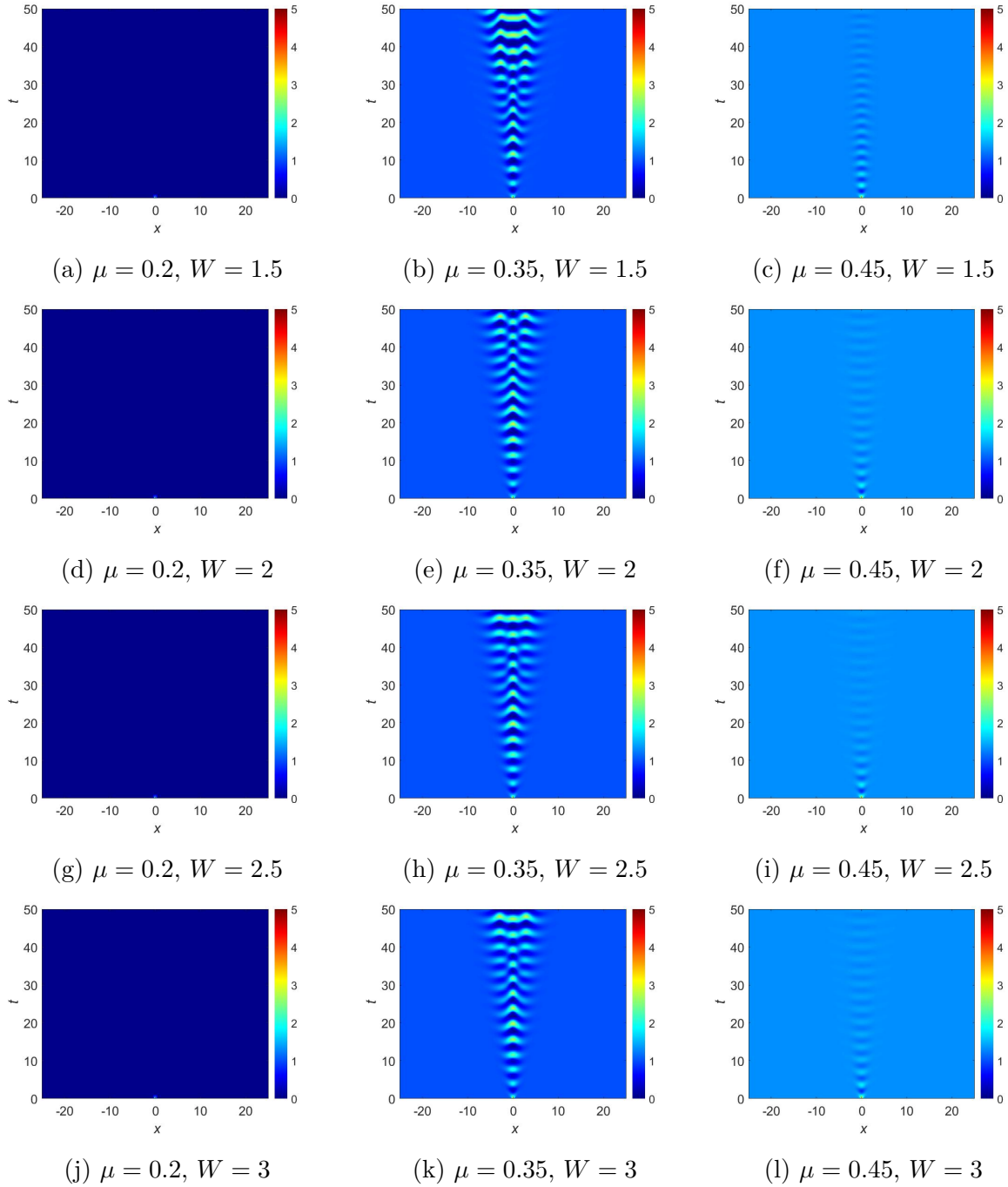


Figure 5.7:  $\text{Ca}^{2+}$  concentration ‘ $c$ ’ over the domain  $-25 \leq x \leq 25$  for  $0 \leq t \leq 50$  generated as solutions of the system (5.4)-(5.15) for  $\hat{T}(c) = T_1(W, c)$ , over a range of  $W$  and  $\mu$ . We fix  $\lambda = 0.5$ . *Software: MATLAB*

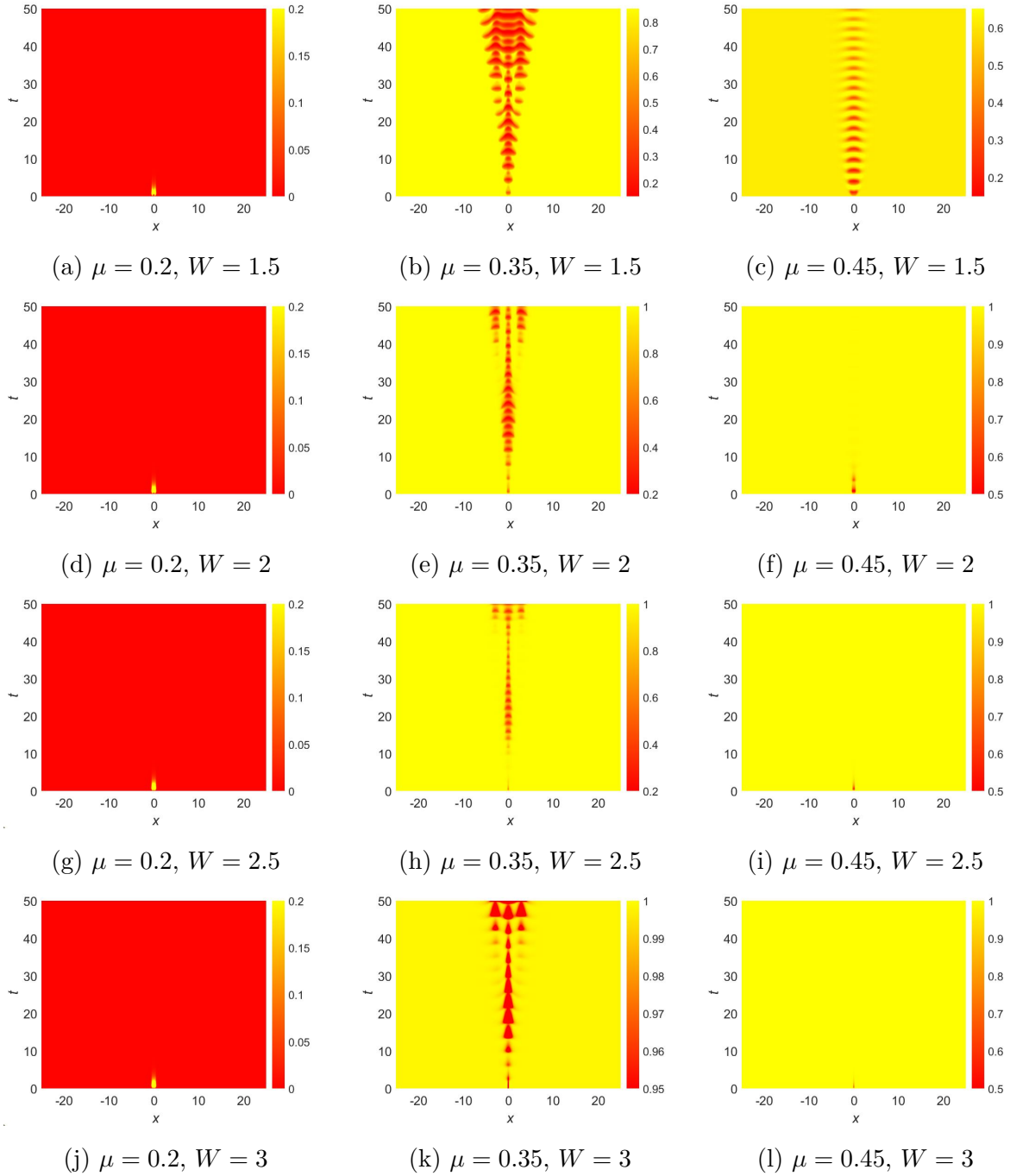


Figure 5.8: Tissue dilation ‘ $\theta$ ’ over the domain  $-25 \leq x \leq 25$  for  $0 \leq t \leq 50$  generated as solutions of the system (5.4)-(5.15) for  $\hat{T}(c) = T_1(W, c)$ , over a range of  $W$  and  $\mu$ . We fix  $\lambda = 0.5$ . *Software: MATLAB*

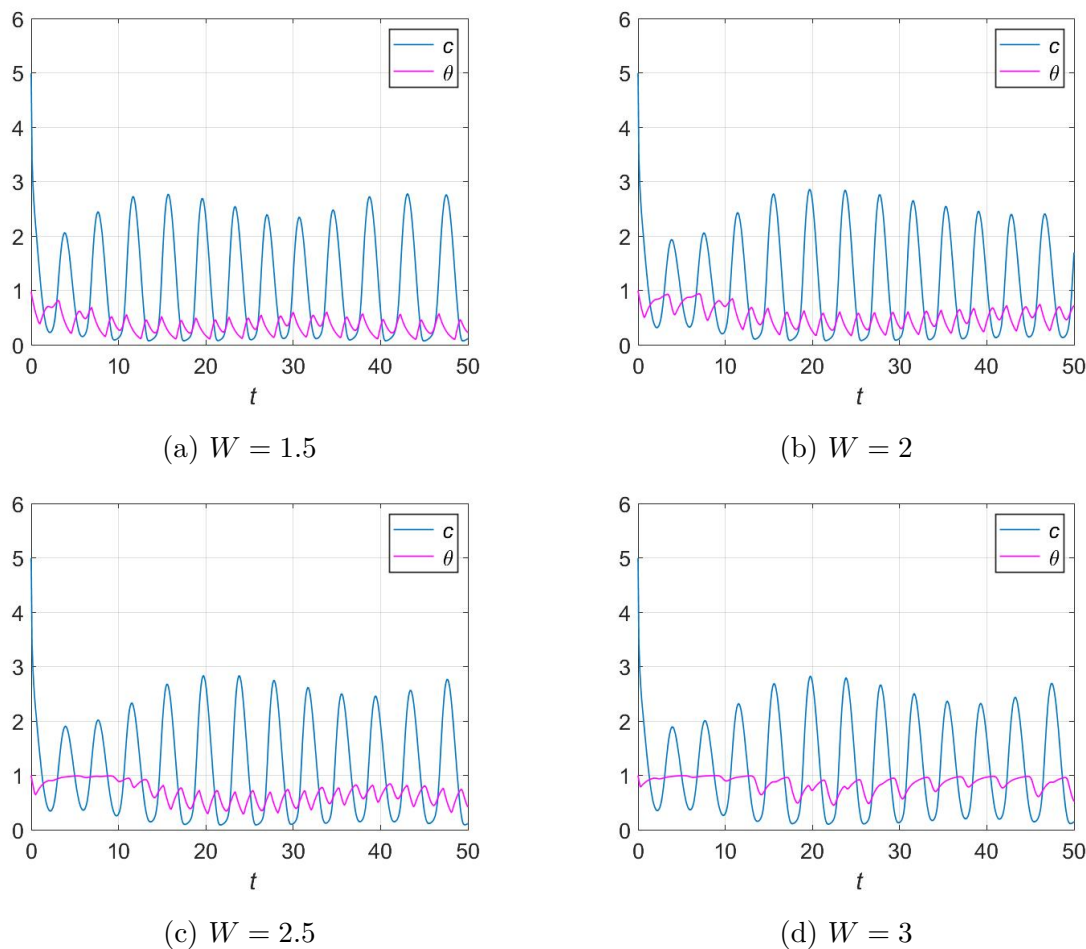


Figure 5.9: Time evolution of  $c$  and  $\theta$  at  $x = 0$  for different values of  $W$ . Solutions of the system (5.4)-(5.15) for the traction term  $\hat{T}(c) = T_1(W, c)$ . We fix  $\mu = 0.35$  and  $\lambda = 0.5$ .

*Software:* MATLAB

Comparing Figures 5.7 & 5.8, it can be seen that the mechanical wave pattern resembles that of the  $\text{Ca}^{2+}$  waves. However, it should be noted that the frequency of the mechanical waves changes with  $W$  (Figure 5.9). For each individual spike in  $\text{Ca}^{2+}$ , we see two spikes in the value of  $\theta$ , similar to the corresponding mechanochemical system (Figure 4.8). In Figure 5.9a, the spikes appear to be merging. In Figures 5.9b & 5.9c, the spikes are of similar amplitude. And, in Figure 5.9d, the two spikes have merged completely. Also, it is interesting to note that, in the case of  $\mu = 0.45$ ,  $W = 1.5$ , the minute  $\text{Ca}^{2+}$  oscillations (Figure 5.7c) are adequate to trigger oscillations of significant amplitude in  $\theta$  (Figure 5.8c).

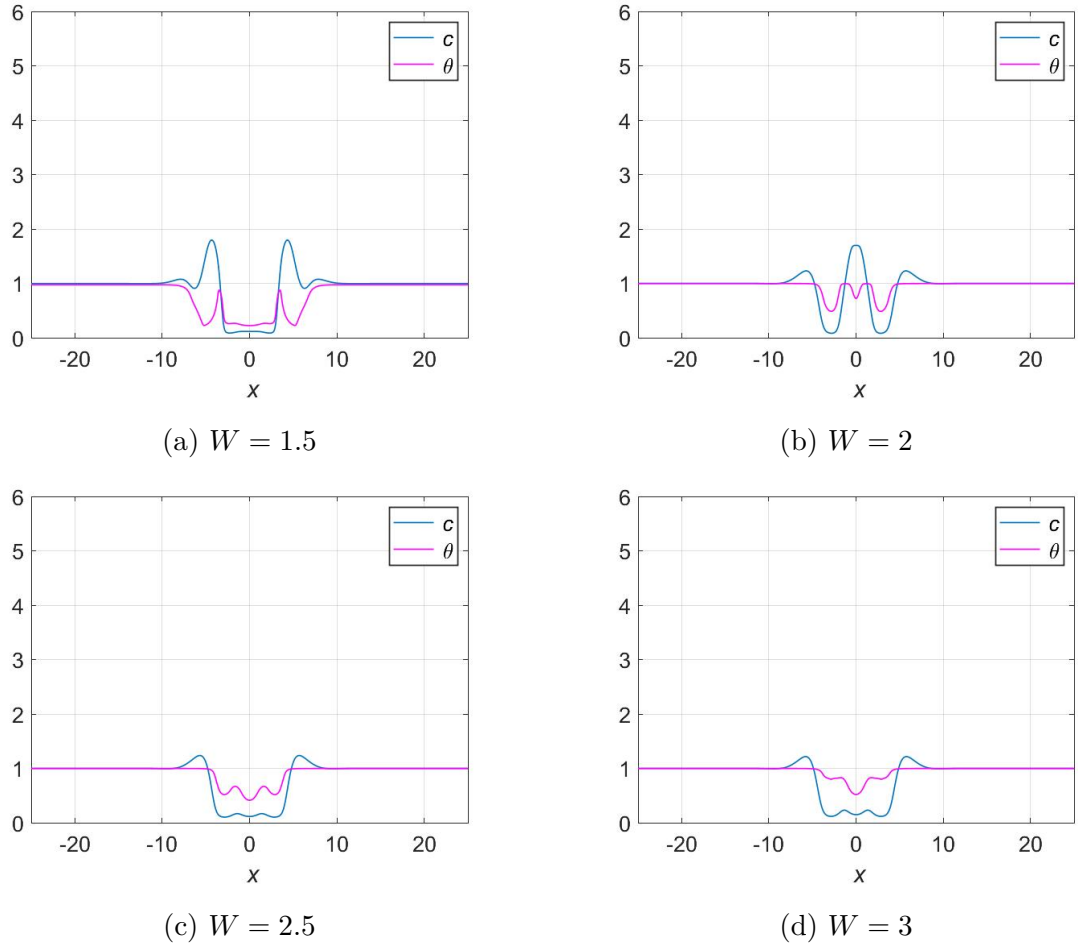


Figure 5.10: Spatial distribution of  $c$  and  $\theta$  at  $t = 50$  for different values of  $W$ . Solutions of the system (5.4)-(5.15) for the traction term  $\hat{T}(c) = T_1(W, c)$ . We fix  $\mu = 0.35$  and  $\lambda = 0.5$ .  
*Software:* MATLAB

Figure 5.9 depicts the evolution of  $c$  and  $\theta$  with time at point  $x = 0$ . Figure 5.10 depicts the distribution of  $c$  and  $\theta$  over the domain at time  $t = 50$ . These plots can be visualised as slices taken from Figures 5.7 & 5.8 (images having  $\mu = 0.35$ ) along the lines  $x = 0$  and  $t = 50$ , respectively.

Again, we note that the amplitude of the  $\text{Ca}^{2+}$  oscillations varies periodically over time while the amplitude of the  $\theta$  oscillations remains constant. However, it should be noted that the central value of the  $\theta$  oscillations changes with time. Upon inspection of Figure 5.9, it would seem that this variation in central value is related to the changing amplitude of the  $\text{Ca}^{2+}$  oscillations, with higher amplitudes of  $\text{Ca}^{2+}$  oscillation corresponding to lower central values of  $\theta$ .

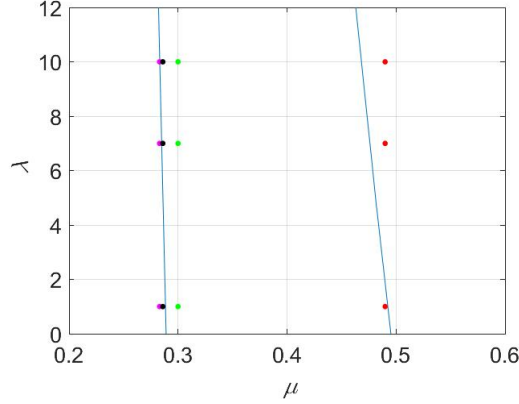


Figure 5.11: Hopf curve for the traction term  $\hat{T}(c) = T_2(c)$ . The coloured dots depict the  $\mu$ - $\lambda$  values used for the simulations of Figures 5.12 & 5.13. *Software*: MATLAB

Figures 5.12 & 5.13 depict system behaviour for the traction term  $\hat{T}(c) = T_2(c)$ . The coloured dots on the corresponding Hopf curve (Figure 5.11) denote the combinations of bifurcation parameters ( $\mu$  and  $\lambda$ ) used for the simulations. The points were chosen to represent different bifurcation regimes, in order to observe the qualitative changes in system behaviour.

- *Outside the Hopf curve - Left area*

$\mu = 0.283, \lambda = 1$ : Solitary pulses (Figure 5.12a). The initial pulse triggers an action potential at  $x = 0$ . This action potential, then, induces two pulses that travel in opposite directions and decay after travelling a short distance. In the ODE model (4.6)-(4.8), this combination of  $\mu$ - $\lambda$  produce an action potential (similar to Figure 4.10a). Here, due to diffusion, we get solitary pulses which travel some distance before decaying.

$\mu = 0.283, \lambda = 7$  and  $\mu = 0.286, \lambda = 1$ : Solitary pulses (Figures 5.12b & 5.12d). The initial pulse triggers an action potential at  $x = 0$ , which is followed by two pulses travelling in opposite directions, towards the boundaries, without noticeable attenuation. For these values of  $\mu$ - $\lambda$ , the ODE model exhibits an action potential (Figure 4.10a) but here, owing to diffusion, we get travelling solitary pulses. Because these values of  $\mu$ - $\lambda$  lie close to the Hopf curve, it is likely that this behaviour might be representative of an intermediate ‘phase’ of the system as it transitions between two bifurcation regimes.

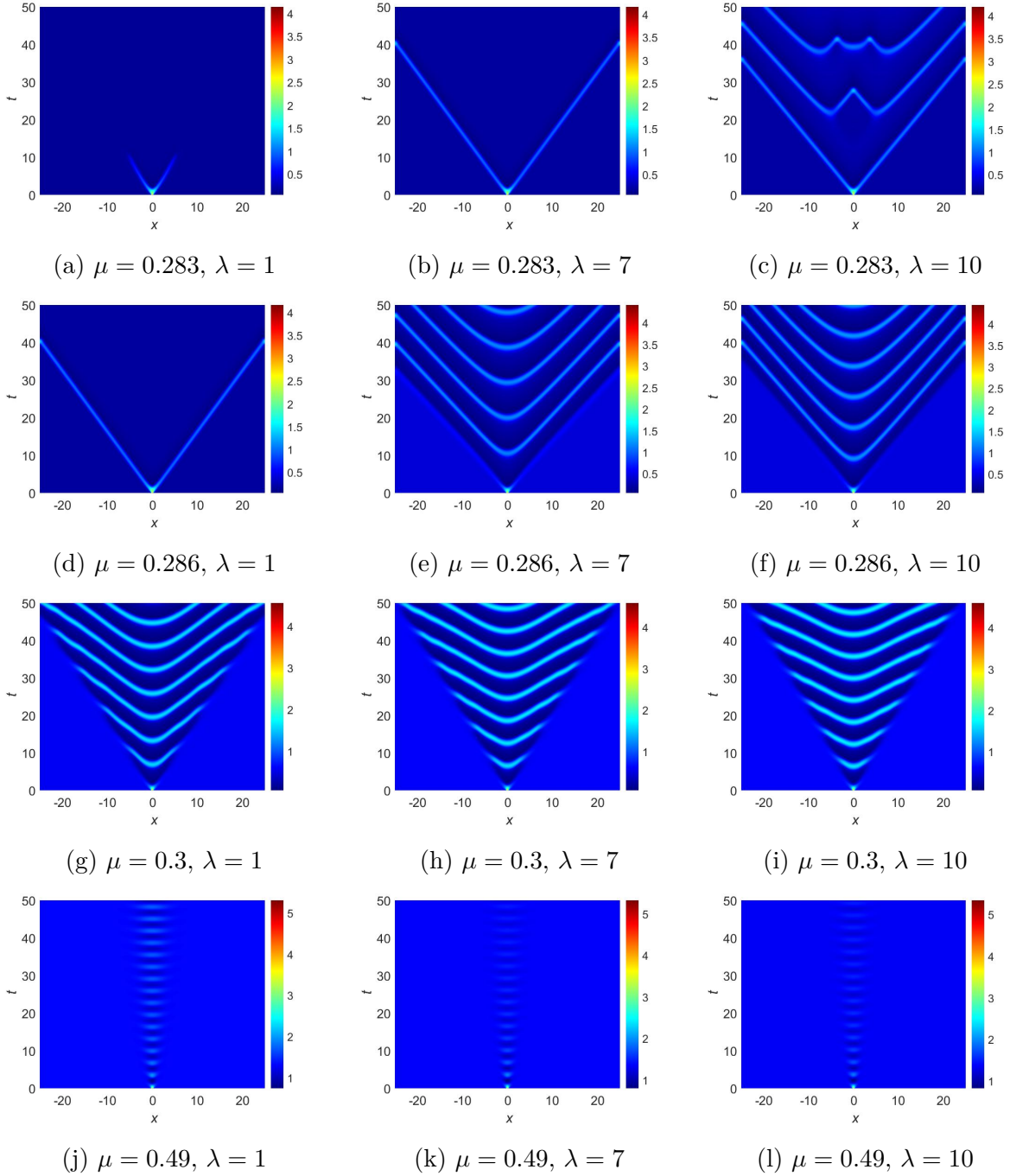


Figure 5.12:  $\text{Ca}^{2+}$  concentration ‘ $c$ ’ over the domain  $-25 \leq x \leq 25$  for  $0 \leq t \leq 50$  generated as solutions of the system (5.4)-(5.15) for  $\hat{T}(c) = T_2(c)$ , over a range of  $\mu$  and  $\lambda$ .

*Software: MATLAB*

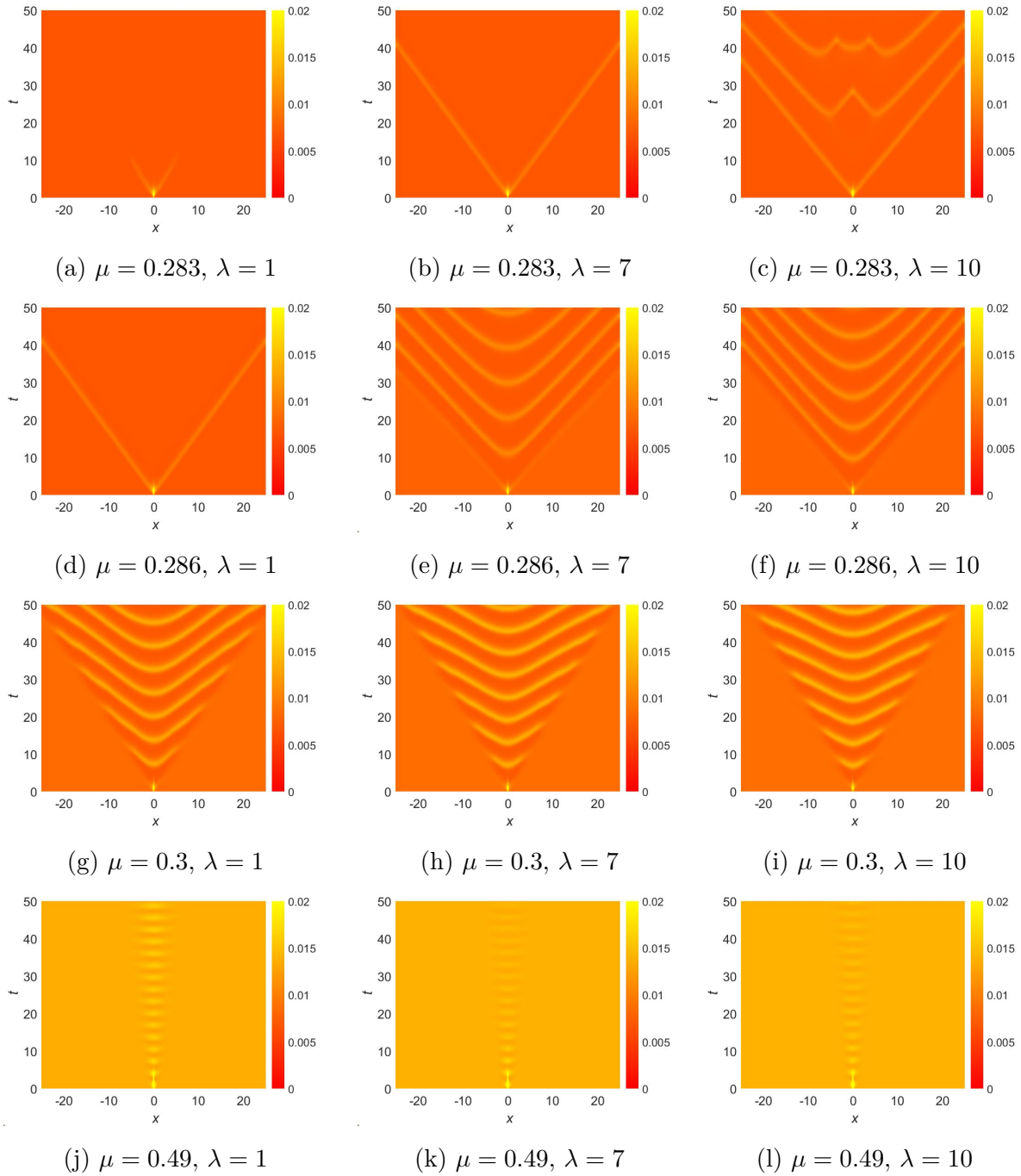


Figure 5.13: Tissue dilation ‘ $\theta$ ’ over the domain  $-25 \leq x \leq 25$  for  $0 \leq t \leq 50$  generated as solutions of the system (5.4)-(5.15) for  $\hat{T}(c) = T_2(c)$ , over a range of  $\mu$  and  $\lambda$ .

Software: MATLAB

$\mu = 0.283$ ,  $\lambda = 10$ : Travelling pulses (Figure 5.12c). The initial pulse triggers an action potential at  $x = 0$ , which is followed by two pulses travelling in opposite directions. Soon afterwards, solitary pulses originate from two points on either side of  $x = 0$  - two pulses from each point. Two of the pulses collide and vanish, the other two travel outward unhindered. This is, then, followed by solitary pulses originating from three points. For this combination of  $\mu$ - $\lambda$ , the ODE system simply produced an action potential. However, in the spatially extended model, we observe this unusual wave pattern due to diffusion. Upon closely inspecting Figure 5.11, it was found that the Hopf bifurcation occurs at  $\mu \approx 0.28324$  for  $\lambda = 10$ . Because these values of  $\mu$ - $\lambda$  lie close to the Hopf curve, it is possible that this behaviour might be representative of an intermediate ‘phase’ of the system as it transitions between two bifurcation regimes.

- *Inside the Hopf curve*

$\mu = 0.286$ ,  $\lambda = 7$  &  $10$ : Periodic wavetrains (Figures 5.12e & 5.12f). The initial pulse triggers low frequency limit cycles and two periodic wavetrains that travel outward in opposing directions. In the ODE model, these values of  $\mu$ - $\lambda$  generated limit cycles (Figures 4.10d & 4.10g).

$\mu = 0.3$ ,  $\lambda = 1, 7$  &  $10$ : Periodic wavetrains (Figures 5.12g, 5.12h & 5.12i). The initial pulse triggers limit cycles and two periodic wavetrains that travel outward in opposing directions. These wavetrains are faster than the ones produced for  $\mu = 0.286$ . In line with the predictions of the Hopf curve and the bifurcation diagram in Figure 2.3a, the ODE model also exhibits limit cycles of greater amplitude and frequency for  $\mu = 0.3$ , compared to  $\mu = 0.286$ .

$\mu = 0.49$ ,  $\lambda = 1$ : Decaying oscillations (Figure 5.12j). Over short simulation times, the system only exhibits low amplitude, high frequency limit cycles near  $x = 0$  but, for larger times (Figure 5.14), the system was observed to display a complex wave pattern. In comparison, for this combination of  $\mu$ - $\lambda$ , the ODE model displayed limit cycles with high amplitude and frequency (Figure 4.10c).

- *Outside the Hopf curve - Right area*

$\mu = 0.49$ ,  $\lambda = 7$  &  $10$ : Decaying oscillations (Figures 5.12k & 5.12l). The initial pulse triggers oscillations at the point of origin. These oscillations die out with time, analogous to Figures 4.10f & 4.10i.

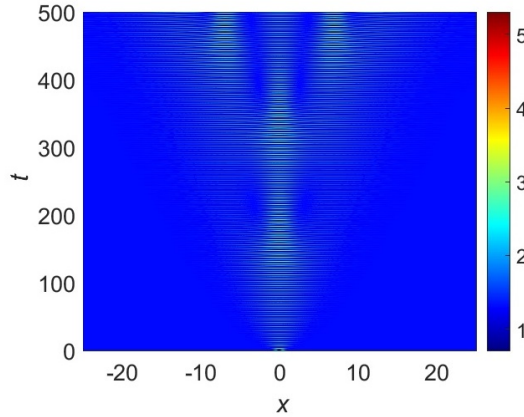


Figure 5.14:  $\text{Ca}^{2+}$  concentration ‘ $c$ ’ over the domain  $-25 \leq x \leq 25$  for  $0 \leq t \leq 500$  generated as a solution of the system (5.4)-(5.15) for  $\hat{T}(c) = T_2(c)$ .  $\mu = 0.49$ , and  $\lambda = 1$ .

*Software:* MATLAB

Figure 5.13 depicts system behaviour, in terms of the associated mechanical waves - tissue dilations, over a range of values of the bifurcation parameters  $\mu$  and  $\lambda$ . Comparing Figures 5.12 & 5.13, once again, it can be seen that the mechanical wave pattern matches that of the  $\text{Ca}^{2+}$  waves and that the mechanical waves have a much smaller amplitude than the  $\text{Ca}^{2+}$  waves.

When comparing Figures 5.3, 5.8 & 5.13, we see that the mechanical waves have the greatest amplitude in the case of Figure 5.8 - corresponding to the traction term  $T_1(W, c)$ .

In Figure 5.9, it was noted that the spikes in  $\theta$  began to merge upon increasing the value of  $W$ . And, in Figure 5.8, for  $\mu = 0.45$  and  $W = 1.5$ , we observed  $\theta$  oscillations of significant amplitude which disappeared upon increasing  $W$  (for the same bifurcation parameters). These behaviours can be understood by visualising the shape of the respective traction terms.

For  $\hat{T}(c) = \frac{10c}{1+10c}$ : In Figure 5.4, the amplitude of the  $\text{Ca}^{2+}$  waves is such that  $0 < c < 2.8$ . In a plot of  $\hat{T}(c)$  versus  $c$ , this range of  $c$  corresponds to  $0 < \hat{T}(c) < 1$ . Hence, we get mechanical waves of noticeable amplitude.

For  $\hat{T}(c) = T_1(W, c)$ : In Figure 5.9, the amplitude of the  $\text{Ca}^{2+}$  waves is such that  $0 < c < 2.8$ . Considering the shape of  $T_1(W, c)$ , it can be recalled that  $\hat{T}(c)$  goes through a cycle of ascent and descent as  $c$  is increased from 0. This generates the shape of a wide ‘pulse’ whose width is determined by  $W$ . For each spike in  $c$ ,  $\hat{T}(c)$  goes through this cycle twice - starting at the rising edge of the  $\text{Ca}^{2+}$  spike and then, again, on the falling edge. This generates two spikes in  $\theta$  for a single spike in  $c$ . As  $W$  is increased, the two spikes in  $\theta$  begin to merge

because  $\hat{T}(c)$  is unable to complete the full cycle.

The  $\theta$  oscillations of Figure 5.8c can be explained similarly. The amplitude of the corresponding  $\text{Ca}^{2+}$  waves (Figure 5.7c) is such that  $1.1 < c < 1.5$ , which corresponds to the falling edge of the associated  $\hat{T}(c)$  (Figure 4.2c). By comparison, for the  $\text{Ca}^{2+}$  waves in Figures 5.7f, 5.7i & 5.7l,  $1.2 < c < 1.4$  which corresponds to the plateau of  $\hat{T}(c)$ , for their respective traction terms. Thus, we observe  $\theta$  oscillations in Figure 5.8c and not in Figures 5.8f, 5.8i & 5.8l.

For  $\hat{T}(c) = T_2(c)$ : In Figure 5.12, the amplitude of the  $\text{Ca}^{2+}$  waves is such that  $0 < c < 3$ . In a plot of  $\hat{T}(c)$  versus  $c$ , it can be seen that  $\hat{T}(c)$  has non-zero values only in the vicinity of  $c = 4$  so, this range of  $c$  corresponds to  $\hat{T}(c) \approx 0$ . Hence, the mechanical waves have a nearly imperceptible amplitude. However, based on Figure 4.10c and the conclusions drawn from the bifurcation diagram (Figure 2.3a), choosing a high value of  $\mu$  inside the Hopf curve e.g.  $\mu = 0.4$  or  $0.45$  should produce mechanical waves of greater amplitude.

It should be noted that all of the traction terms above have a peak value of 1 i.e.  $\hat{T}_{max} = 1$ . If the traction terms are scaled to give higher values of  $\hat{T}_{max}$  (Figure 5.15), it results in larger mechanical waves. However, scaling the traction term reduces the area enclosed by the associated Hopf curve (Figure 5.16), limiting the range of  $\mu$ - $\lambda$  parameter choices that produce periodic wavetrains.

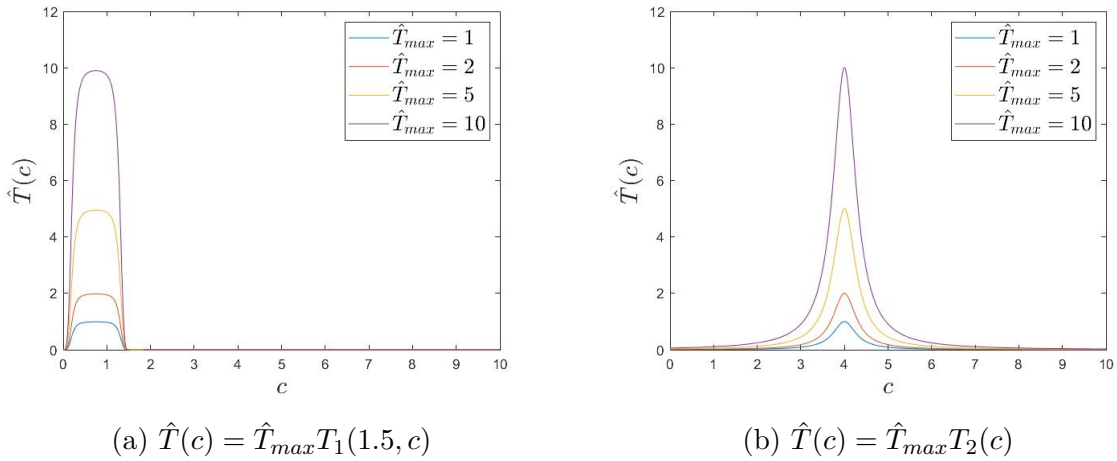


Figure 5.15: Shape of the scaled traction stress terms. *Software:* MATLAB

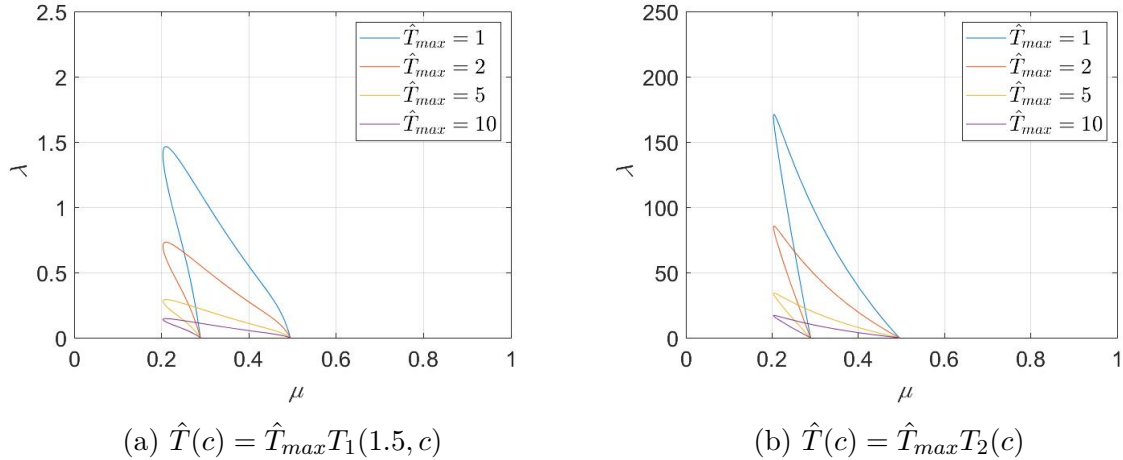


Figure 5.16: Hopf curves for the scaled traction stress terms. *Software:* MATLAB

In this chapter, diffusion (in one spatial dimension) was added to the mechanochemical ODE model from Chapter 4 and we studied the behaviour of the spatially extended system for the traction stress terms modelled in Chapter 4. It can be recalled that we used the results of the linear stability analysis and the simulations from Chapter 2 to describe the behaviour of the spatially extended Atri model in Chapter 3. In an analogous manner, the Hopf curve and the simulations from Chapter 4 were used to explain the behaviour of the mechanochemical PDE model.

In the instances where the system displayed periodic wavetrains, it was observed that the amplitude of the  $\text{Ca}^{2+}$  waves varied periodically over time. This was found to exert an effect on the mechanical waves such that, at a point, the central value of the  $\theta$  oscillations varied in accordance with the amplitude of the  $\text{Ca}^{2+}$  oscillations at that point.

Thus far, it has been observed that the shape of the traction term and the amplitude of the  $\text{Ca}^{2+}$  waves can greatly impact the mechanical waves. However, the traction terms (and, by extension, the oscillations in  $\theta$ ) don't seem to have much effect on  $\text{Ca}^{2+}$  due to our choice of low  $\hat{T}_{max}$ . With higher values of  $\hat{T}_{max}$ , we can expect a greater impact on the behaviour of  $\text{Ca}^{2+}$ . However, as seen in Figure 5.16, increasing  $\hat{T}_{max}$  greatly reduces the range of  $\lambda$  that sustains oscillations. And because  $\lambda$  is the 'strength' of the coupling between  $\text{Ca}^{2+}$  and cell mechanics, this imposes a restriction upon the effect that cell mechanics can have on cytosolic  $\text{Ca}^{2+}$  dynamics.

# Chapter 6

## The Atri model on a disc (2D)

In the models discussed so far, we have worked with diffusion in one spatial dimension. In reality, the developing embryo is a complex three-dimensional structure and hence, in our modelling, we will now progress to two spatial dimensions, assuming radial symmetry for convenience. In fact, in most experimental investigations, groups of cells arranged in a two-dimensional layer are studied. For instance, Narciso et al. (2017) studied intercellular  $\text{Ca}^{2+}$  waves in *Drosophila* wing discs and Wallingford et al. (2001) studied intercellular  $\text{Ca}^{2+}$  waves in the dorsal tissue layer of gastrulating *Xenopus* embryos.

In this chapter, we simulate the Atri model over a circular disc (including  $\text{Ca}^{2+}$  diffusion). The circular disc is taken to approximate a layer of tissue, comprised of a few hundred cells. For the sake of simplicity, we forgo the inclusion of cellular mechanics here, which can be explored in a future study.

From Chapter 3, it can be recalled that the Atri model is given by Equations (3.1)-(3.3), where  $c$  represents cytosolic  $\text{Ca}^{2+}$  concentration and  $h$  is a dimensionless variable denoting the proportion of IPRs that have not been inactivated. Once again, neglecting  $\text{IP}_3$  dynamics, the equations reduce to:

$$\frac{\partial c}{\partial t} = D_c \nabla^2 c + J_{\text{channel}}(c, h) - J_{\text{pump}}(c) + J_{\text{leak}}, \quad (6.1)$$

$$\tau_h \frac{\partial h}{\partial t} = h_{\infty}(c) - h, \quad (6.2)$$

where

$$J_{\text{channel}}(c, h) = k_{\text{flux}} \mu h \frac{b k_1 + c}{k_1 + c}, \quad J_{\text{pump}}(c) = \frac{\gamma c}{k_{\gamma} + c}, \quad J_{\text{leak}} = \beta,$$

and

$$h_{\infty}(c) = \frac{k_2^2}{k_2^2 + c^2}.$$

## 6.1 Nondimensionalising the model

While Atri et al. (1993) extended their model to two spatial dimensions in the Cartesian system, we use plane polar coordinates. Owing to the radial symmetry of our chosen initial conditions (Equations (6.7) & (6.8)) and model geometry, this choice of coordinates allows us to simplify the model. To nondimensionalise the model, as in Chapter 3, we set  $c = k_1 \bar{c}$ ,  $t = \tau_h \bar{t}$ ,  $r = l \bar{r}$ , and neglect  $J_{\text{leak}}$  as it is again assumed to be small. Dropping bars for notational convenience, we obtain

$$\frac{\partial c}{\partial t} = D_o \left( \frac{\partial^2 c}{\partial r^2} + \frac{1}{r} \frac{\partial c}{\partial r} \right) + \mu h K_1 \frac{b+c}{1+c} - \frac{\Gamma c}{K+c}, \quad (6.3)$$

$$\frac{\partial h}{\partial t} = \frac{K_2^2}{K_2^2 + c^2} - h, \quad (6.4)$$

where

$$r = \sqrt{x^2 + y^2}.$$

In Equations (6.3) & (6.4),  $D_o = D_c \tau_h / l^2$ ,  $K_1 = k_f \tau_h / k_1$ ,  $\Gamma = \gamma \tau_h / k_1$ ,  $K = k_\gamma / k_1$ , and  $K_2 = k_2 / k_1$ . Taking  $l = 20 \mu m$  and using the parameter values of Atri et al. (1993) (see Appendix A1, Table A1.1), we obtain  $K_2 = 1$ ,  $\Gamma = 40/7 \sim 5.71$ ,  $K = 1/7$ , and  $D_o = 0.1$ . We again take  $\mu$  to be the *bifurcation parameter*.

## 6.2 Simulations

We simulate the model over the surface of a circular disc of diameter  $1000 \mu m$  (i.e.  $r \leq 25$  in nondimensional units). For a cell diameter of  $50 \mu m$ , this can be visualised by imagining 20 epithelial cells placed side by side along the diameter of this disc. By approximating the shape of an individual cell to be circular, and neglecting the spaces between the cells, we can imagine roughly 400 cells in this circular tissue. Again, we neglect any intercellular interfaces, so we model the tissue as a continuum.

To study the spatiotemporal evolution of the system for different bifurcation regimes, Equations (6.3)-(6.4) were solved numerically in COMSOL Multiphysics for the system parameters specified in Table A1.1, over the circular disc. As in Section 3.3, we consider a  $\text{Ca}^{2+}$  wave diffusing outward over the cells that make up the epithelial tissue layer. Because we ignore the effects of the tissue boundaries, we apply no flux boundary conditions:

$$c_r(25, t) = 0 \quad (6.5)$$

$$h_r(25, t) = 0 \quad (6.6)$$

Equations (6.7)-(6.8) are taken to be the initial conditions of the system. Equation (6.7) expresses a Gaussian pulse (in  $c$ ) whose centre coincides with the centre of the disc. All other points are taken to be at the steady state values of  $c$  and  $h$ .

$$c(r, 0) = c_{St} + \exp(-0.5r^2) \quad (6.7)$$

$$h(r, 0) = h_{St} = \frac{1}{1 + c_{St}^2} \quad (6.8)$$

Figures 6.1, 6.2, 6.5 & 6.12 depict  $c(r, t)$  for different bifurcation regimes. It should be noted that the COMSOL Multiphysics software depicts solutions in Cartesian coordinates. Because our model geometry and initial conditions are radially symmetric, we expect the solutions to be radially symmetric as well.

In Chapter 2, the linear stability analysis helped us identify the different bifurcation regimes for the Atri model. In the case of the spatially extended model, the system will experience bifurcations at *approximately* the same values of  $\mu$  since diffusion effects are small. In Chapter 3, we studied the behaviour of the model over a one-dimensional geometry. In the following pages, we study how that relates to the behaviour over the two-dimensional geometry.

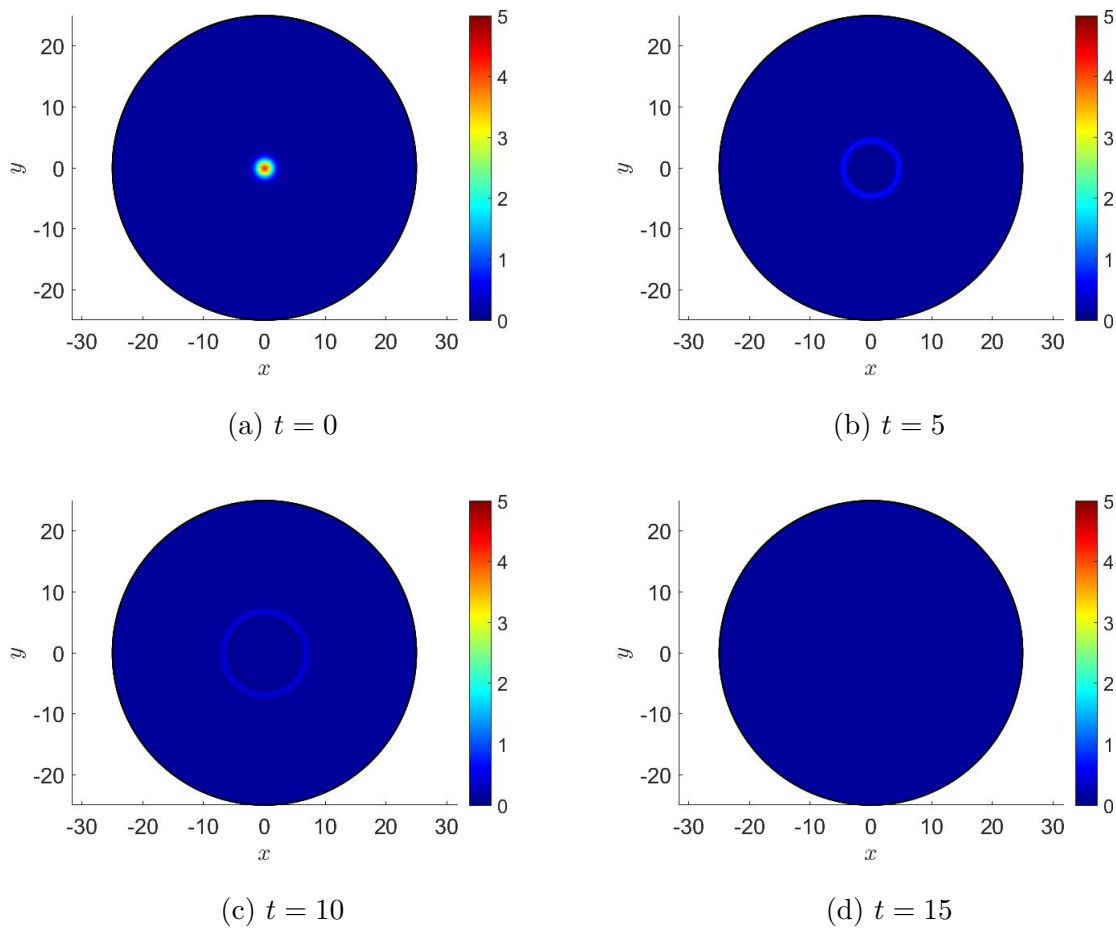


Figure 6.1:  $\text{Ca}^{2+}$  concentration ‘ $c$ ’ over the circular domain of radius  $r = 25$  at different instants of time, generated as solutions of the system (6.3)-(6.8). Simulations ran up to  $t = 50$ , for  $\mu = 0.284$ . *Software: COMSOL Multiphysics*

$\mu = 0.284$ : In Figure 6.1, the initial pulse triggers an action potential at  $r = 0$ . This action potential, then, induces a solitary circular wave that travels outward but decays after travelling a short distance. This is analogous to the solitary pulses in Figure 3.1a.

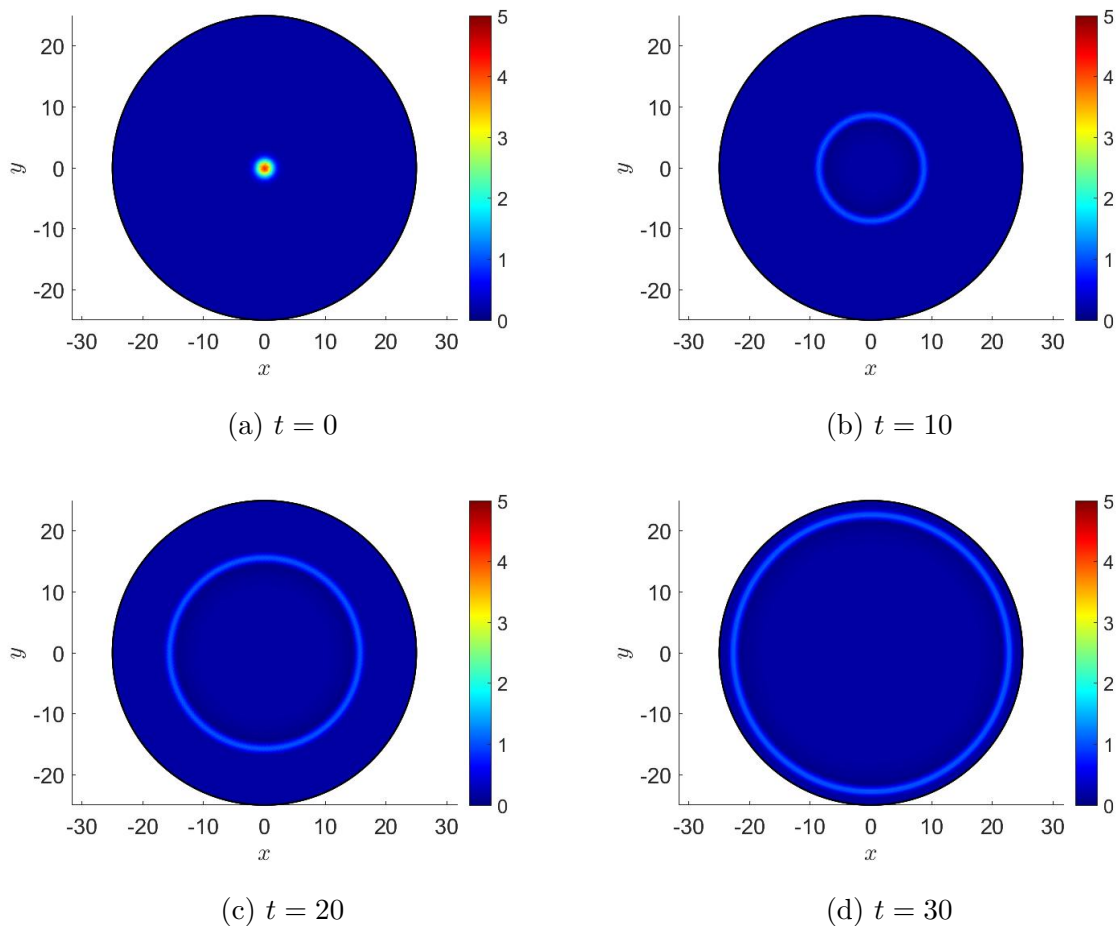


Figure 6.2:  $\text{Ca}^{2+}$  concentration ‘ $c$ ’ over the circular domain of radius  $r = 25$  at different instants of time, generated as solutions of the system (6.3)-(6.8). Simulations ran up to  $t = 50$ , for  $\mu = 0.288$ . *Software: COMSOL Multiphysics*

$\mu = 0.288$ : In Figure 6.2, the initial pulse triggers an action potential at  $r = 0$  which then induces a solitary circular wave that travels outward. This wavefront does not decay, it propagates towards the periphery of the domain without noticeable attenuation and then passes beyond it. It is expected that the wavefront decays after travelling a finite distance beyond the periphery. This is analogous to the solitary pulses in Figure 3.1b.

Generally speaking, in the cases where the system produces a solitary wave, the value of  $\mu$  seems to determine the distance that the wave will travel before decaying. A higher value of  $\mu$  yields a wave that travels over a longer distance. However, increasing the value of  $\mu$  further, beyond the Hopf bifurcation point, changes the system’s behaviour and produces periodic waves.

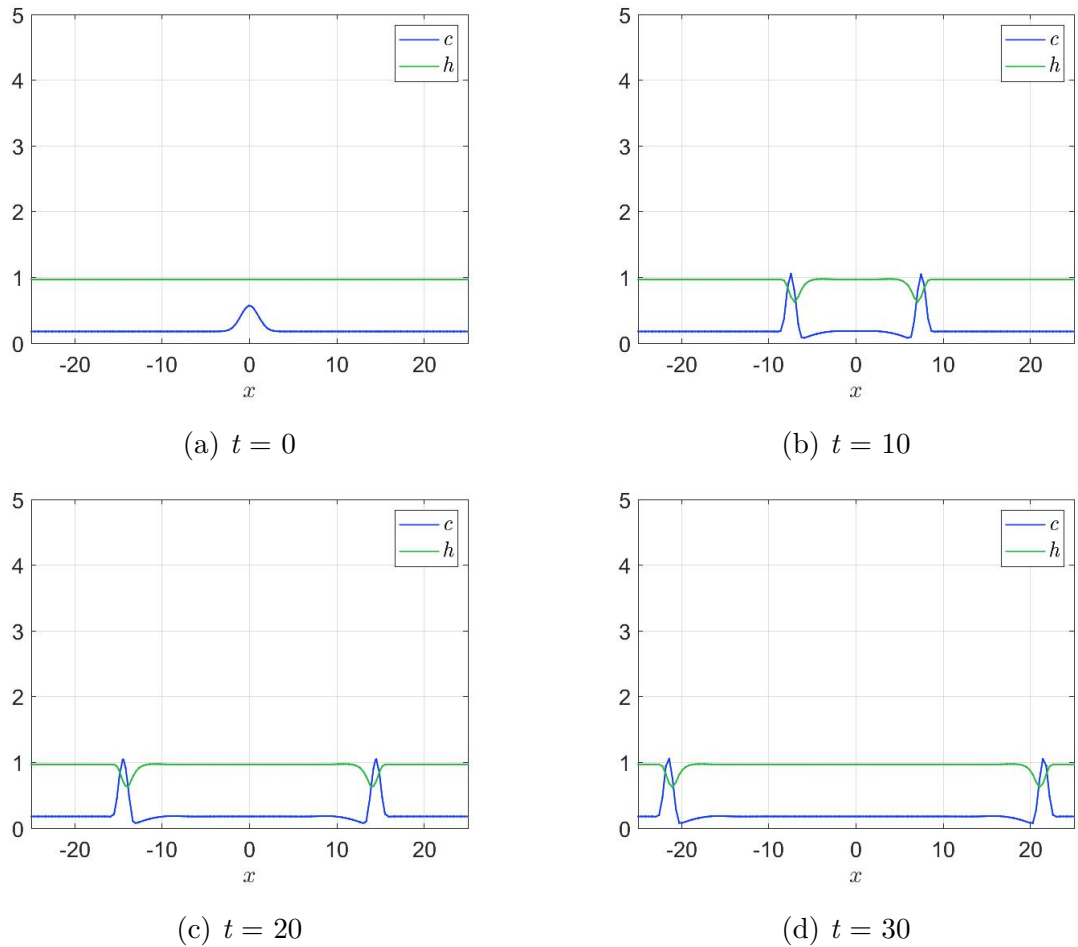


Figure 6.3: Spatial distribution of  $c$  and  $h$  along the diameter at  $y = 0$ . Solutions of the system (6.3)-(6.8) for  $\mu = 0.288$ , at (a)  $t = 0$ , (b)  $t = 10$ , (c)  $t = 20$ , and (d)  $t = 30$ .

*Software:* COMSOL Multiphysics

Figure 6.3 depicts the distribution of  $c$  and  $h$  along the diameter of the disc ( $y = 0$ ) at time instants  $t = 0, 10, 20$ , and  $30$ . As expected, this cross-sectional view of the circular wave resembles the solitary pulses seen in Figure 3.4. On comparing with Figure 3.4, it appears that the solitary pulses have the same amplitude and travel with similar speed in both models. Figure 6.4 depicts the evolution of  $c$  and  $h$  with time at points  $x = 5, y = 0$  and  $x = 15, y = 0$ .

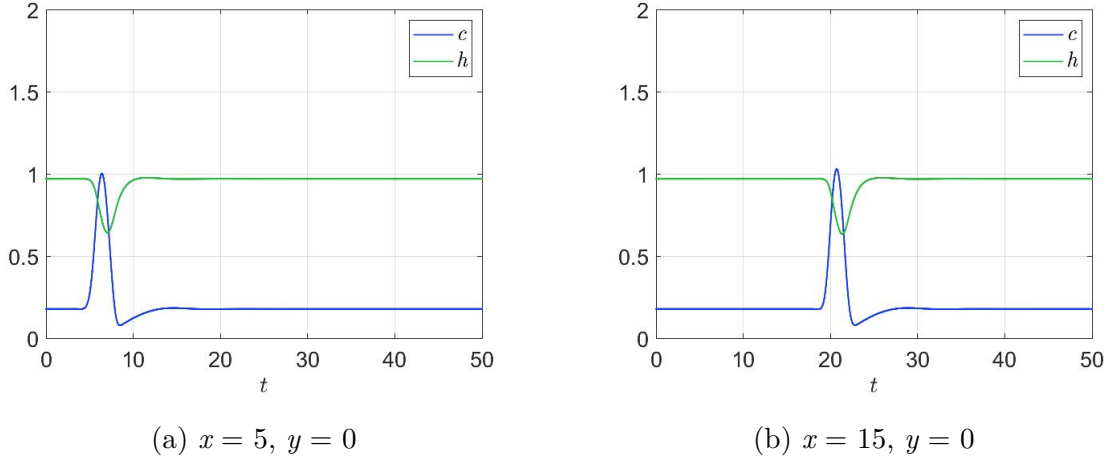


Figure 6.4: Time evolution of  $c$  and  $h$ . Solutions of the system (6.3)-(6.8) for  $\mu = 0.288$ , at points (a)  $x = 5, y = 0$  and (b)  $x = 15, y = 0$ . *Software*: COMSOL Multiphysics

$\mu = 0.3$ : In Figure 6.5, the initial pulse triggers limit cycles at  $r = 0$  and periodic circular waves that travel outward. This is analogous to the periodic wavetrains in Figure 3.1c.

Figure 6.6 depicts the distribution of  $c$  and  $h$  along the diameter of the disc at time instants  $t = 0, 10, 20, 30, 40$ , and  $50$ . As expected, this cross-sectional view of the circular waves resembles the periodic wavetrain seen in Figure 3.7. Figure 6.7 depicts the evolution of  $c$  and  $h$  with time at points  $x = 5, y = 0$  and  $x = 15, y = 0$ .

The waves originate at the centre of the disc and travel towards the periphery but they decay after travelling a certain distance. The first wave decays very close to the centre (Figure 6.6b). Before they begin to decay, the waves appear to travel with a consistent amplitude and each wave travels further than its predecessor before decaying. The effect of this behaviour can be seen in Figure 6.7. In both Figures 6.7a & 6.7b, the first oscillation is smaller than the subsequent oscillations, which are of constant amplitude.

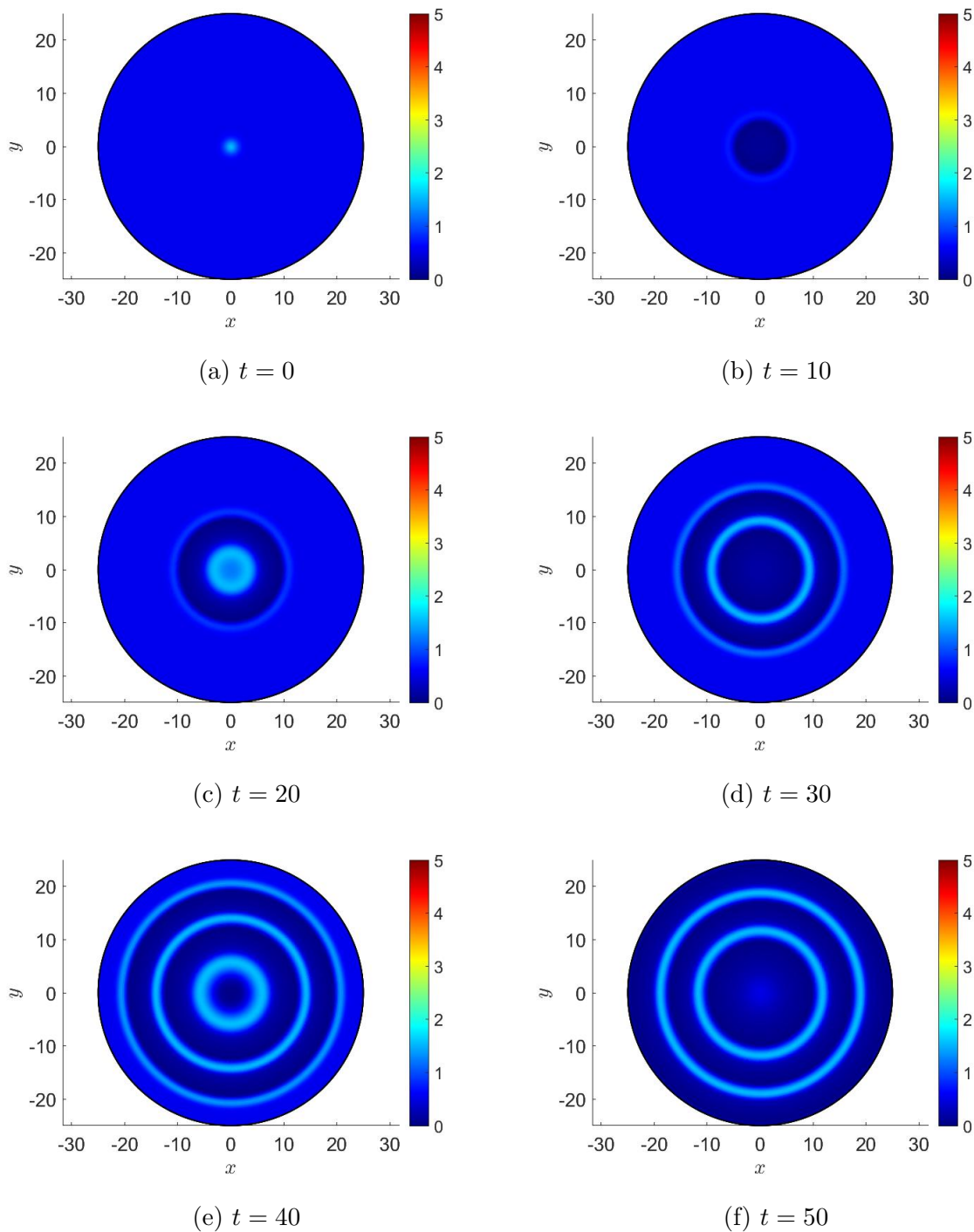
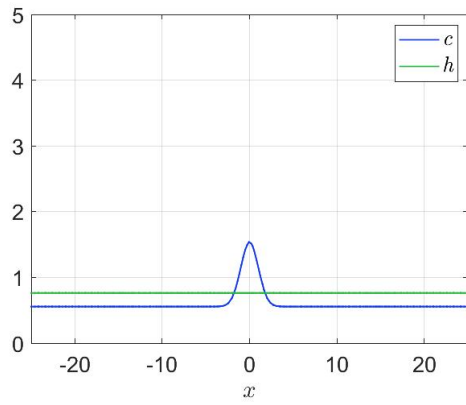
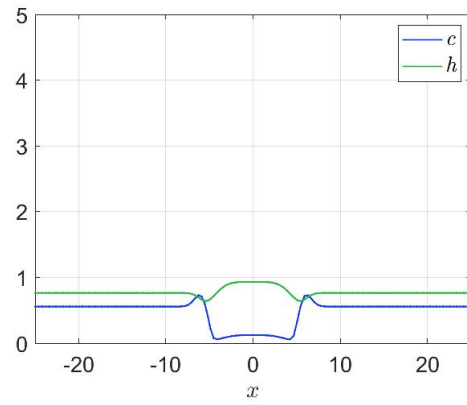


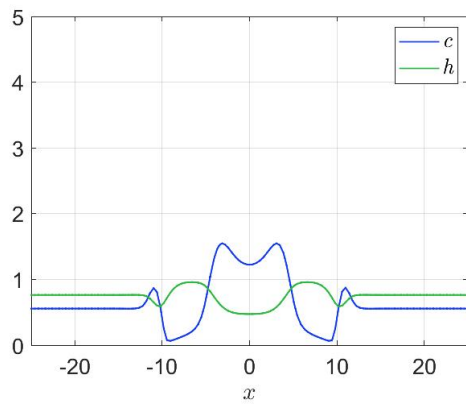
Figure 6.5:  $\text{Ca}^{2+}$  concentration ‘ $c$ ’ over the circular domain of radius  $r = 25$  at different instants of time, generated as solutions of the system (6.3)-(6.8). Simulations ran up to  $t = 50$ , for  $\mu = 0.3$ . *Software: COMSOL Multiphysics*



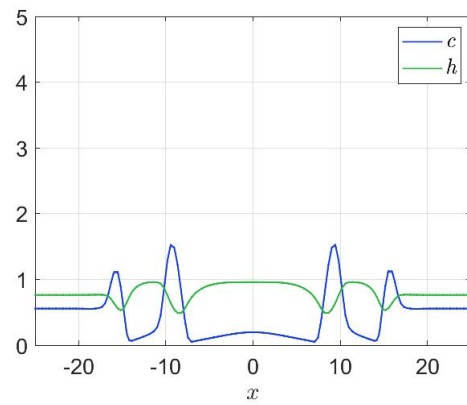
(a)  $t = 0$



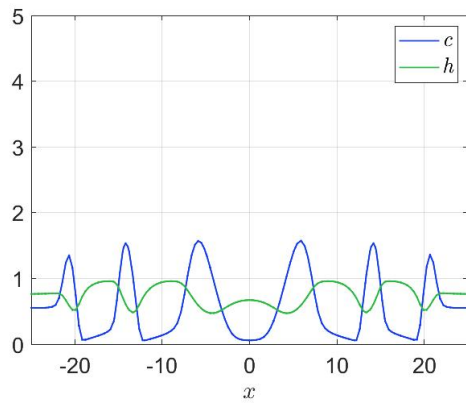
(b)  $t = 10$



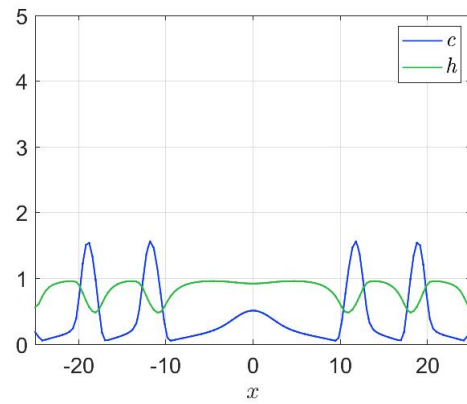
(c)  $t = 20$



(d)  $t = 30$



(e)  $t = 40$



(f)  $t = 50$

Figure 6.6: Spatial distribution of  $c$  and  $h$  along the diameter at  $y = 0$ . Solutions of the system (6.3)-(6.8) for  $\mu = 0.3$ , at (a)  $t = 0$ , (b)  $t = 10$ , (c)  $t = 20$ , (d)  $t = 30$ , (e)  $t = 40$ , and (f)  $t = 50$ . *Software:* COMSOL Multiphysics

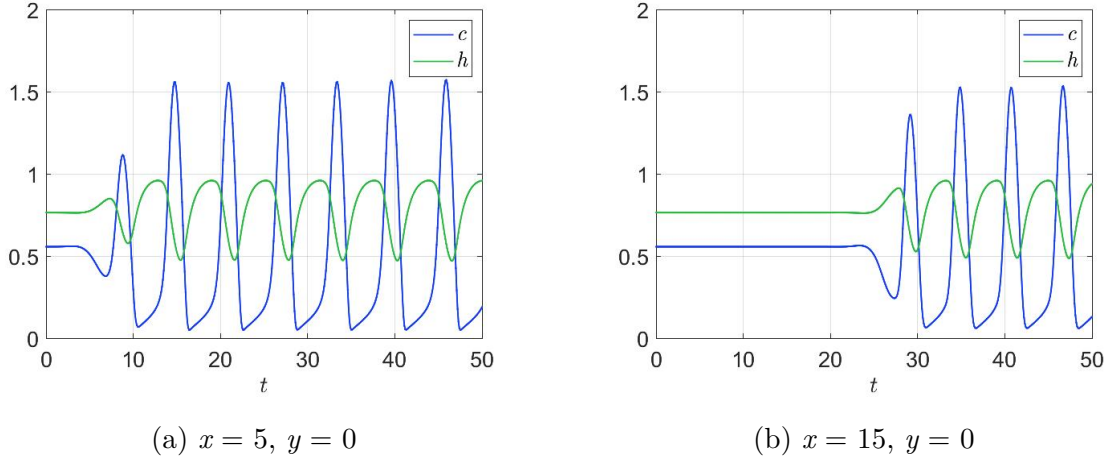


Figure 6.7: Time evolution of  $c$  and  $h$ . Solutions of the system (6.3)-(6.8) for  $\mu = 0.3$ , at points (a)  $x = 5, y = 0$  and (b)  $x = 15, y = 0$ . *Software*: COMSOL Multiphysics

$\mu = 0.35$ : In Figure 6.8, the initial pulse triggers limit cycles at  $r = 0$  and periodic circular waves that travel inward. This is analogous to the periodic wavetrains in Figure 3.1d.

Figure 6.9 depicts the distribution of  $c$  and  $h$  along the diameter of the disc at time instants  $t = 0, 10, 20, 30, 40$ , and  $50$ . The waves originate at some distance from the centre of the disc and then travel towards it. The first wave originates very close to the centre (Figure 6.9c). Each subsequent wave is generated further away from the centre and travels inward with constant amplitude.

$\mu = 0.45$ : In Figure 6.10, the initial pulse triggers limit cycles at  $r = 0$  and inward-travelling periodic circular waves, in the vicinity of  $r = 0$ . This is analogous to the periodic wavetrains in Figure 3.1e.

Figure 6.11 depicts the distribution of  $c$  and  $h$  along the diameter of the disc at time instants  $t = 0, 5, 10, 15, 20, 25, 30, 35$ , and  $40$ . The waves originate at a distance from the centre of the disc and then travel towards it. Unlike Figure 6.9, however, these waves are only generated in the vicinity of  $r = 0$ .

$\mu = 0.55$ : In Figure 6.12, the initial pulse triggers oscillations at the point of origin. These oscillations die out with time, analogous to Figure 3.1f.

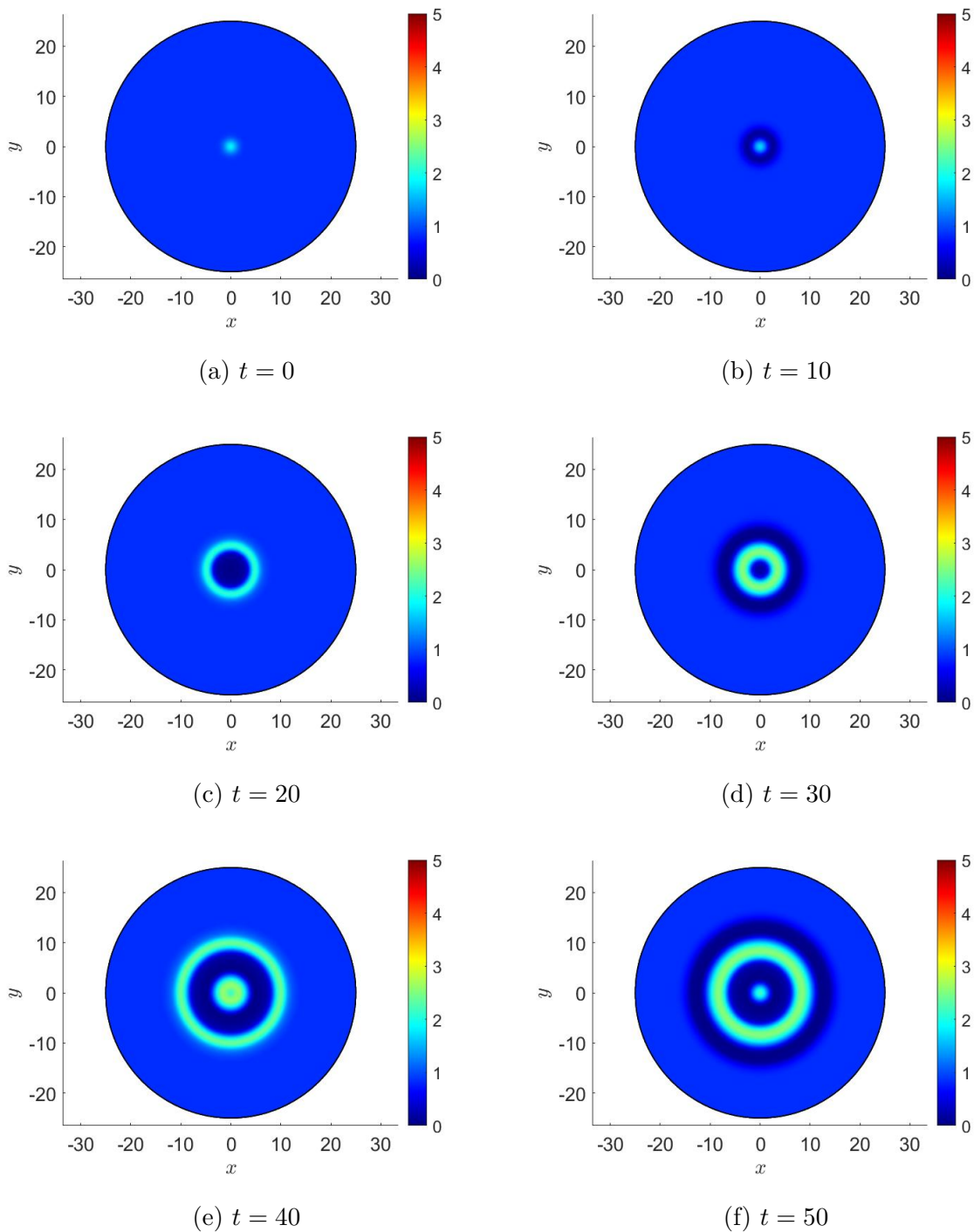
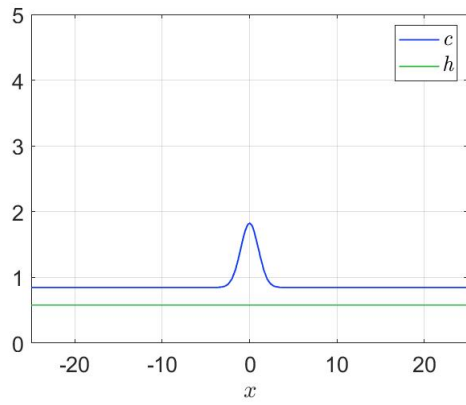
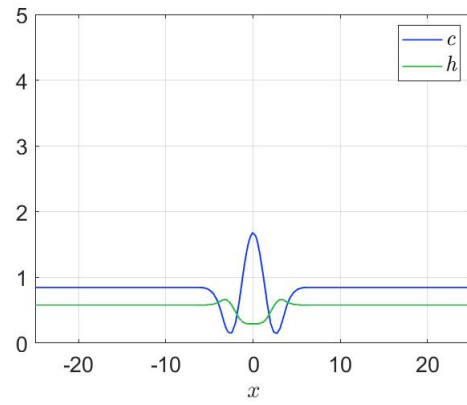


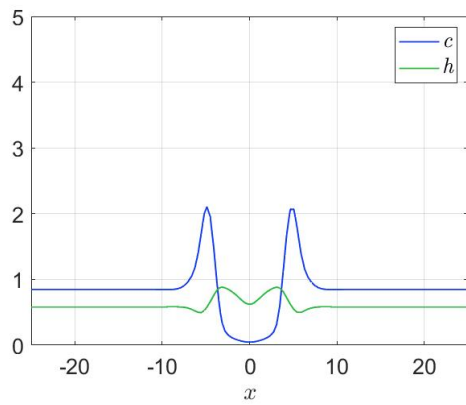
Figure 6.8:  $\text{Ca}^{2+}$  concentration ‘ $c$ ’ over the circular domain of radius  $r = 25$  at different instants of time, generated as solutions of the system (6.3)-(6.8). Simulations ran up to  $t = 50$ , for  $\mu = 0.35$ . *Software:* COMSOL Multiphysics



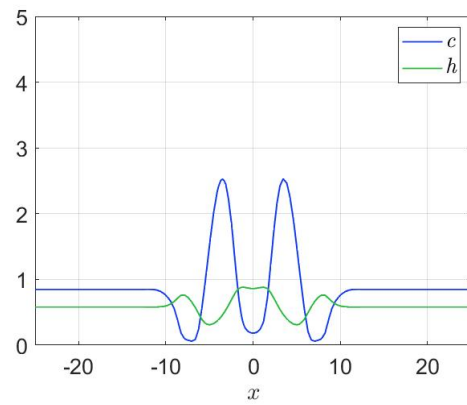
(a)  $t = 0$



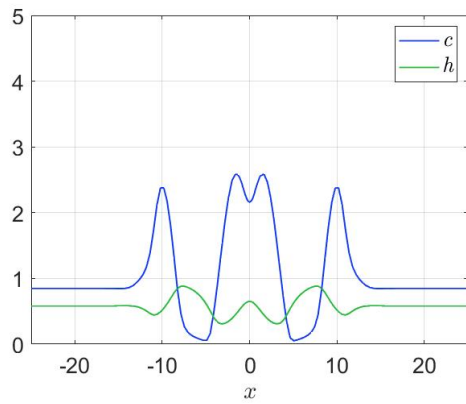
(b)  $t = 10$



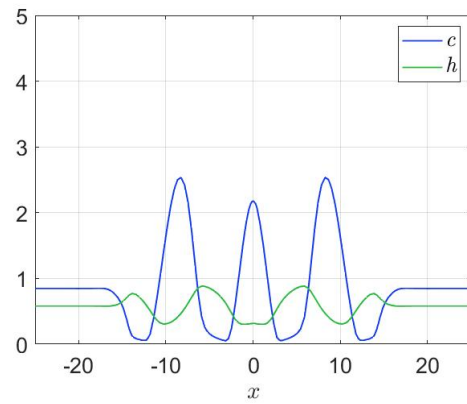
(c)  $t = 20$



(d)  $t = 30$



(e)  $t = 40$



(f)  $t = 50$

Figure 6.9: Spatial distribution of  $c$  and  $h$  along the diameter at  $y = 0$ . Solutions of the system (6.3)-(6.8) for  $\mu = 0.35$ , at (a)  $t = 0$ , (b)  $t = 10$ , (c)  $t = 20$ , (d)  $t = 30$ , (e)  $t = 40$ , and (f)  $t = 50$ . *Software: COMSOL Multiphysics*

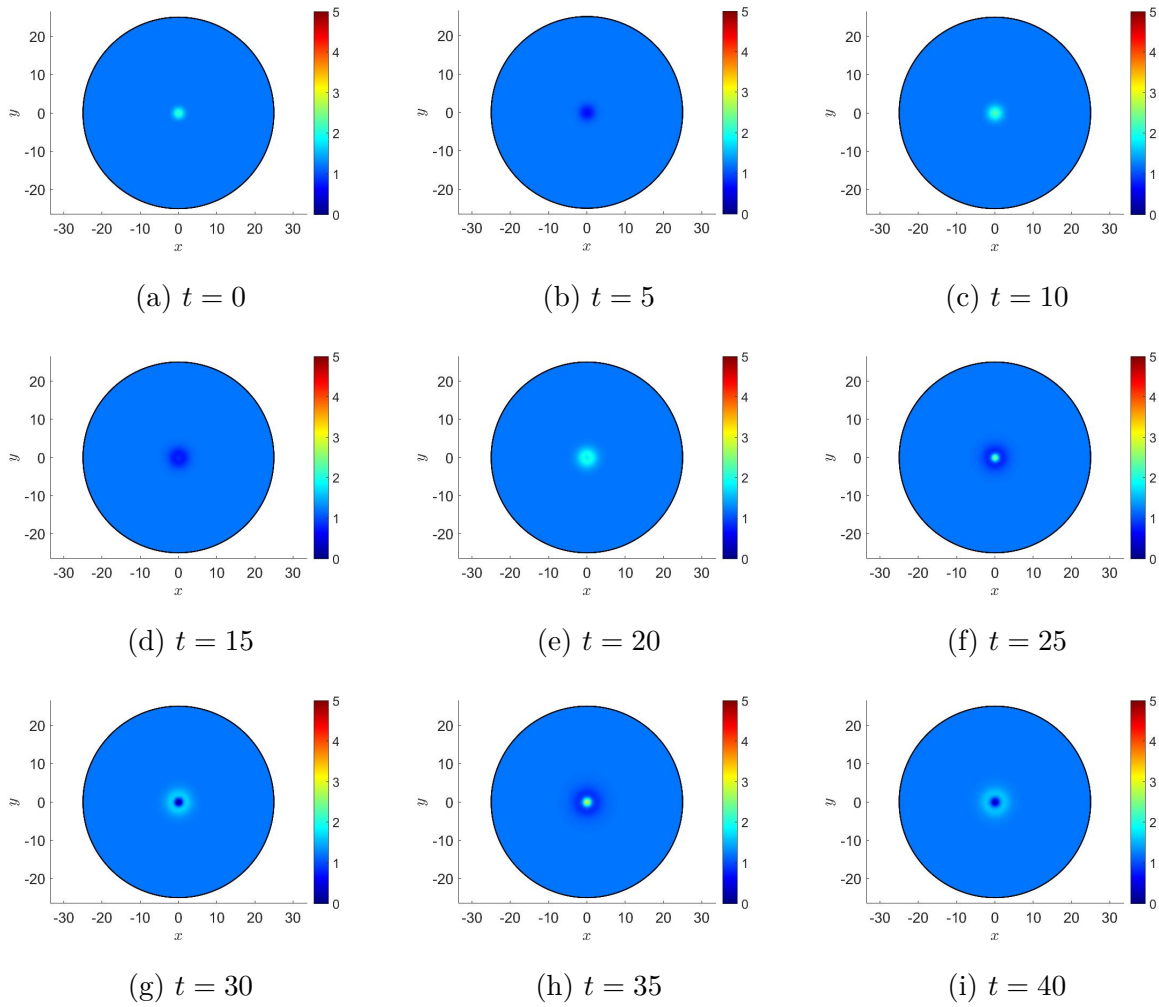


Figure 6.10:  $\text{Ca}^{2+}$  concentration ‘ $c$ ’ over the circular domain of radius  $r = 25$  at different instants of time, generated as solutions of the system (6.3)-(6.8). Simulations ran up to  $t = 50$ , for  $\mu = 0.45$ . *Software:* COMSOL Multiphysics

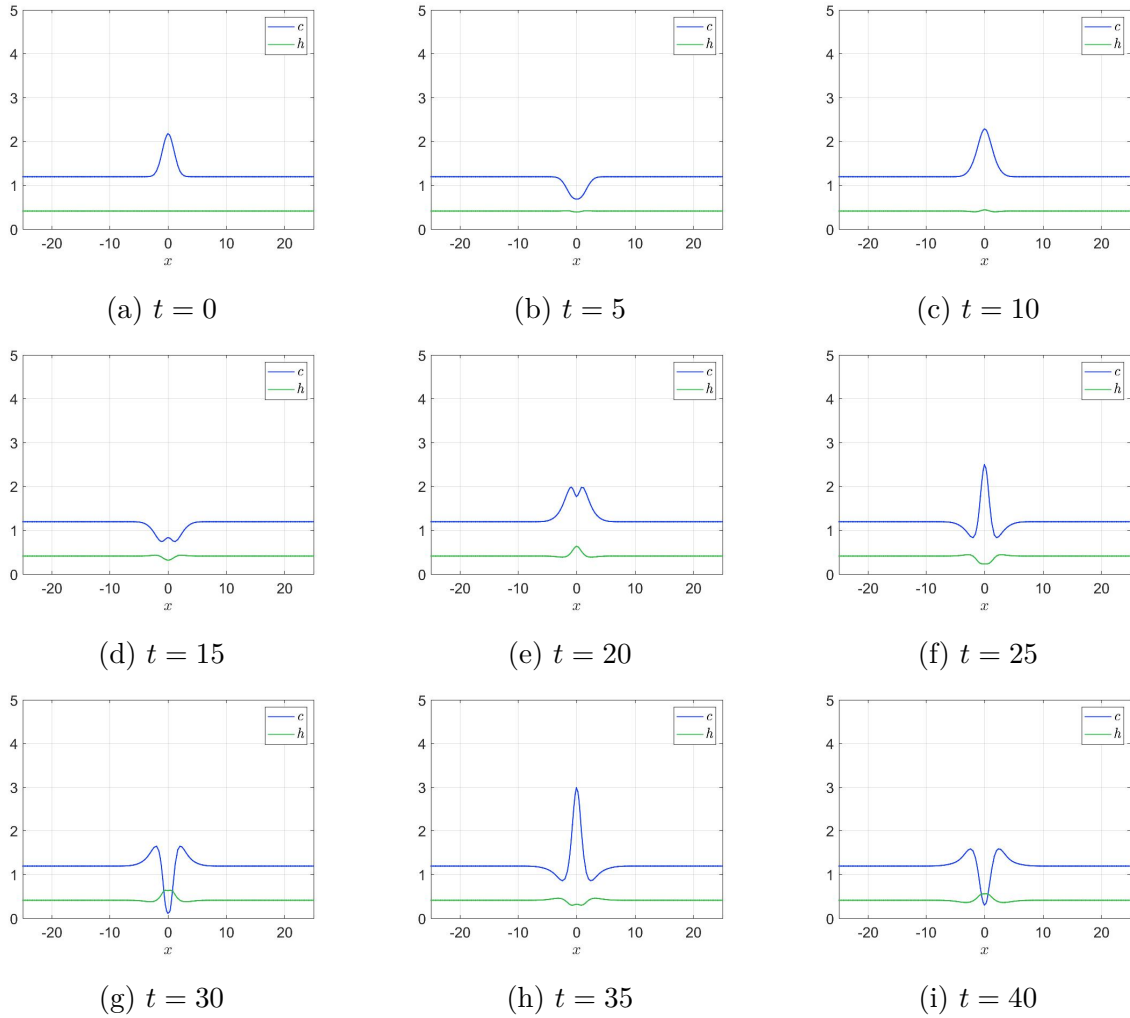


Figure 6.11: Spatial distribution of  $c$  and  $h$  along the diameter at  $y = 0$ . Solutions of the system (6.3)-(6.8) for  $\mu = 0.45$ , at (a)  $t = 0$ , (b)  $t = 5$ , (c)  $t = 10$ , (d)  $t = 15$ , (e)  $t = 20$ , (f)  $t = 25$ , (g)  $t = 30$ , (h)  $t = 35$ , and (i)  $t = 40$ . *Software:* COMSOL Multiphysics

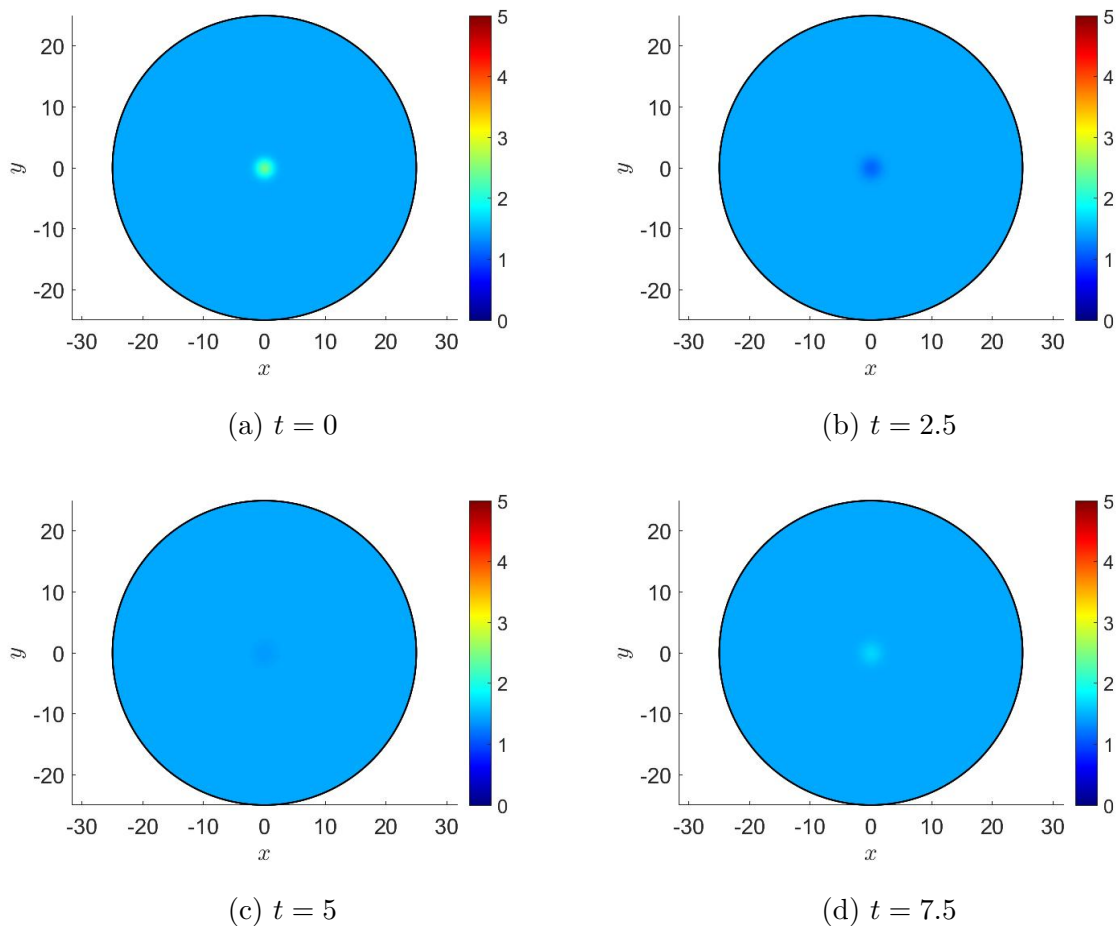


Figure 6.12:  $\text{Ca}^{2+}$  concentration ‘ $c$ ’ over the circular domain of radius  $r = 25$  at different instants of time, generated as solutions of the system (6.3)-(6.8). Simulations ran up to  $t = 50$ , for  $\mu = 0.55$ . *Software:* COMSOL Multiphysics

In this chapter, we computed solutions of the spatially extended Atri model over a circular disc and observed the wave patterns of  $\text{Ca}^{2+}$ . It was found that the periodic wavetrains arising in the one-dimensional Atri model (Chapter 3) are similar to the circular waves in the two-dimensional model (Figures 6.5, 6.8 & 6.10). It appears that the two-dimensional model undergoes bifurcations at approximately the same values predicted by the linear stability analysis of Chapter 2, performed for the one-dimensional model. Our choice of a radially symmetric initial condition allowed us to simplify the model and obtain circular  $\text{Ca}^{2+}$  waves. Non-radially symmetric initial conditions could be explored in a future study.

# Chapter 7

## Summary, Conclusions and Future Work

In this project, we studied a series of increasingly complex  $\text{Ca}^{2+}$  signalling models. We focused on the interplay of  $\text{Ca}^{2+}$  signalling and mechanics in fertilization and embryogenesis, a very important phenomenon, albeit poorly understood. Despite its importance, there is a scarcity of models that couple  $\text{Ca}^{2+}$  signalling and cellular mechanics.

In Chapter 1, we begin with a discussion of the biological mechanism underpinning  $\text{Ca}^{2+}$  signalling and the coupling between  $\text{Ca}^{2+}$  signalling and mechanics. Then, we summarise some key models that have been proposed for describing  $\text{Ca}^{2+}$  signalling.

In Chapter 2, we present the derivation of the Atri et al. (1993) model. The model is a non-linear dynamical system consisting of two ODEs, for  $\text{Ca}^{2+}$  concentration ( $c$ ) and the fraction of  $\text{IP}_3$  receptors that have not been inactivated ( $h$ ), respectively. The  $\text{IP}_3$  concentration ( $\mu$ ) is chosen as the bifurcation parameter. We nondimensionalise the model and perform a linear stability analysis, to identify the range of  $\mu$  that sustains  $\text{Ca}^{2+}$  oscillations, as in Kaouri et al. (2019). We then simulate the Atri model for different values of  $\mu$ , corresponding to the different bifurcation regimes (Figure 2.2). The system displays sustained non-linear oscillations (limit cycles) for  $0.289 < \mu < 0.495$ , in agreement with the results of the stability analysis.

Note that we focus on the Atri model because it is backed by experimental findings (Estrada et al., 2016) and its structure allows a semi-analytical treatment (Kaouri et al., 2019). This makes it easy to identify the range of the bifurcation parameter ( $\mu$ ) that sustains  $\text{Ca}^{2+}$  oscillations.

In Chapter 3, we include  $\text{Ca}^{2+}$  diffusion to the Atri model and nondimensionalise. We solve the model numerically over a one-dimensional geometry for different bifurcation regimes,

based on the values of  $\mu$  identified in Chapter 2 (Figure 3.1). We find that the action potential and limit cycles seen in the previous chapter correspond to solitary waves and periodic wavetrains in the one-dimensional model.

In Chapter 4, we follow Murray & Oster (1984) and Kaouri et al. (2019) where the cell, or tissue, is modelled as a viscoelastic material. The traction stress saturates with  $\text{Ca}^{2+}$  and is modelled with a Hill function. From a force balance equation, an ODE for cell dilation/contraction ( $\theta$ ) is derived. The resulting mechanochemical model is a system of three ODEs for the variables  $c$ ,  $h$ , and  $\theta$ .  $\mu$  and  $\lambda$  are chosen as the bifurcation parameters. We nondimensionalise the model and solve Equations (4.16) & (4.17) to plot a *Hopf curve* corresponding to the traction term  $\hat{T}(c)$  (Figure 4.3). The Hopf curve for the Hill function indicates that  $\text{Ca}^{2+}$  oscillations vanish when either  $\mu$  or  $\lambda$  are increased beyond a certain threshold.

For this project, we introduce two *novel* ‘pulse’-shaped traction stress terms -  $T_1(W, c)$  and  $T_2(c)$ , and compare them with a traction term (Hill function) used in Kaouri et al. (2019). Comparing the Hopf curves corresponding to these traction terms over the parameter space of interest:  $\lambda \in (0, 10] \cup \mu \in [0, 1]$ , we find that, in the case of  $T_1(W, c)$ , the  $\text{Ca}^{2+}$  oscillations vanish when either  $\mu$  or  $\lambda$  are increased beyond a certain threshold. In the case of  $T_2(c)$ ,  $\text{Ca}^{2+}$  oscillations vanish when  $\mu$  is increased beyond a certain threshold, however, changing the value of  $\lambda$  doesn’t seem to impact  $\text{Ca}^{2+}$  oscillations.

We then simulate the mechanochemical ODE model for each traction term over the various bifurcation regimes (Figures 4.6, 4.8 & 4.10) - identified using the Hopf curve for each corresponding traction term. We find that the ‘pulse’-width of the traction term can regulate the frequency of the cell contractions (Figure 4.8), specifically, the frequency of the contractions decreases as the width of the traction term increases. The frequency of the  $\text{Ca}^{2+}$  oscillations remains unchanged, however.

In Chapter 5, we include  $\text{Ca}^{2+}$  diffusion in the mechanochemical model of Chapter 4 and obtain a PDE model, which we again nondimensionalise. As in Chapter 4, we simulate the model for each traction term over the different bifurcation regimes (Figures 5.2, 5.3, 5.7, 5.8, 5.12 & 5.13) and compare with the results obtained in Chapter 4.

We find that the mechanical wave pattern is shown to mirror that of the  $\text{Ca}^{2+}$  waves. Also, as found in Chapter 4, the frequency of cell contractions decreases as the width of the traction term increases (Figure 5.9). It was noted that the amplitude of the  $\text{Ca}^{2+}$  oscillations at a point varies periodically with time (Figures 5.4 & 5.9), unlike the behaviour seen in Chapter 4 (Figures 4.6b, 4.8b, 4.8e, 4.8h & 4.8k).

Based on the simulation results of Chapters 4 and 5, we find that the shape of the  $\text{Ca}^{2+}$  waves can greatly impact the shape and size of the mechanical waves whereas the mechanical

waves can only exert a limited influence on the  $\text{Ca}^{2+}$  waves. This can be understood by considering Equations (4.6), (4.8), (5.4) & (5.6).

In Equations (4.8) and (5.6),  $\hat{T}(c)$  is dependent upon  $c$  and directly impacts  $\theta$ , therefore, the shape of the  $\text{Ca}^{2+}$  waves can impact the amplitude, frequency and shape of the mechanical waves based on the shape of  $\hat{T}(c)$ . Increasing the height of  $\hat{T}(c)$  increases the amplitude of the mechanical waves.

From Equations (4.6) and (5.4), it is apparent that mechanical waves of a higher amplitude would exert a greater influence on the shape of the  $\text{Ca}^{2+}$  waves. Note that the parameter  $\lambda$  determines the ‘strength’ of the coupling between  $\theta$  and  $c$ . Upon increasing the height of  $\hat{T}(c)$ , the area of the associated Hopf curve decreases (Figure 5.16). This greatly reduces the range of  $\lambda$  that sustains oscillations and imposes an upper limit on our choice of  $\lambda$ . Thus, we conclude that cell mechanics can only exert a limited influence on the cytosolic  $\text{Ca}^{2+}$  dynamics.

In Chapter 6, similarly to Chapter 3, we include  $\text{Ca}^{2+}$  diffusion in the Atri model from Chapter 2 but solve the model over a disc. We simulate the model for different bifurcation regimes (Figures 6.1 - 6.12). Comparing the results with Chapter 3, we find that the periodic wavetrains observed in the one-dimensional model correspond to radially symmetric periodic waves here. Based on our comparison of Figures 3.1a, 3.1b, 3.1c, 3.1d, 3.1e & 3.1f with Figures 6.1, 6.2, 6.5, 6.8, 6.10 & 6.12, respectively, we find that the disc model undergoes bifurcations at *approximately* the same values as the one-dimensional model.

The radially symmetric initial conditions chosen in Chapter 6 allow us to simplify our model and generate radially symmetric waves. Non-radially symmetric initial conditions would yield different wave patterns and this can be explored in a future study. The next step would be to incorporate the mechanics equation in the model. We could then extend the mechanochemical model and solve it over a cylinder, to emulate an embryonic epithelial cell.

It should be noted that the models studied in this project are deterministic, however,  $\text{Ca}^{2+}$  signalling is an inherently stochastic process so there exists a separate class of models that take into account the effect of stochastic processes. Also, the models we studied assume the cells, and tissue, to be a continuous viscoelastic material i.e. the models are continuum-based. In contrast, there exists another class of models used to study the interplay of  $\text{Ca}^{2+}$  signalling and cell mechanics - cell-based models. In these models, each cell is represented by a polyhedron and a set of equations at each vertex governs the change in cell shape. Stochastic models and cell-based models both could be another direction of research.

# References

- Ajduk, A., Ilozue, T., Windsor, S., Yu, Y., Seres, K. B., Bompfrey, R. J., . . . others (2011). Rhythmic actomyosin-driven contractions induced by sperm entry predict mammalian embryo viability. *Nature communications*, *2*, 417.
- Alberts, B., Bray, D., Hopkin, K., Johnson, A. D., Lewis, J., Raff, M., . . . Walter, P. (2013). *Essential cell biology*. Garland Science.
- Allbritton, N. L., Meyer, T., & Stryer, L. (1992). Range of messenger action of calcium ion and inositol 1, 4, 5-trisphosphate. *Science*, *258*(5089), 1812–1815.
- Árnadóttir, J., & Chalfie, M. (2010). Eukaryotic mechanosensitive channels. *Annual review of biophysics*, *39*, 111–137.
- Atri, A., Amundson, J., Clapham, D., & Sneyd, J. (1993). A single-pool model for intracellular calcium oscillations and waves in the xenopus laevis oocyte. *Biophysical Journal*, *65*(4), 1727–1739.
- Bereiter-Hahn, J. (2005). Mechanics of crawling cells. *Medical engineering & physics*, *27*(9), 743–753.
- Berridge, M. (1989). *In cell to cell signalling from experiments to theoretical models. a goldbeter, editors*. Academic Press, New York.
- Berridge, M. J. (1993). Inositol trisphosphate and calcium signalling. *Nature*, *361*(6410), 315–325.
- Berridge, M. J., & Galione, A. (1988). Cytosolic calcium oscillators. *The FASEB Journal*, *2*(15), 3074–3082.
- Berridge, M. J., Lipp, P., & Bootman, M. D. (2000). The versatility and universality of calcium signalling. *Nature reviews Molecular cell biology*, *1*(1), 11.

- Brodland, G. W., Daniel, I., Chen, L., & Veldhuis, J. H. (2006). A cell-based constitutive model for embryonic epithelia and other planar aggregates of biological cells. *International journal of plasticity*, *22*(6), 965–995.
- Camacho, P., & Lechleiter, J. D. (1993). Increased frequency of calcium waves in xenopus laevis oocytes that express a calcium-atpase. *Science*, *260*(5105), 226–229.
- Camacho, P., & Lechleiter, J. D. (1995). Spiral calcium waves: implications for signalling. *Calcium Waves, Gradients and Oscillations*, *188*, 66–84.
- Chambers, E. L., Pressman, B. C., & Rose, B. (1974). The activation of sea urchin eggs by the divalent ionophores a23187 and x-537a. *Biochemical and biophysical research communications*, *60*(1), 126–132.
- Charles, A. C., Dirksen, E. R., Merrill, J. E., & Sanderson, M. J. (1993). Mechanisms of intercellular calcium signaling in glial cells studied with dantrolene and thapsigargin. *Glia*, *7*(2), 134–145.
- Charles, A. C., Merrill, J. E., Dirksen, E. R., & Sanderson, M. J. (1991). Intercellular signaling in glial cells: calcium waves and oscillations in response to mechanical stimulation and glutamate. *Neuron*, *6*(6), 983–992.
- Charles, A. C., Naus, C., Zhu, D., Kidder, G. M., Dirksen, E. R., & Sanderson, M. J. (1992). Intercellular calcium signaling via gap junctions in glioma cells. *The Journal of cell biology*, *118*(1), 195–201.
- Cheng, J. C., Miller, A. L., & Webb, S. E. (2004). Organization and function of microfilaments during late epiboly in zebrafish embryos. *Developmental dynamics: an official publication of the American Association of Anatomists*, *231*(2), 313–323.
- Chernoff, E. A., & Hilfer, S. R. (1982). Calcium dependence and contraction in somite formation. *Tissue and Cell*, *14*(3), 435–449.
- Christodoulou, N., & Skourides, P. A. (2015). Cell-autonomous  $ca^{2+}$  flashes elicit pulsed contractions of an apical actin network to drive apical constriction during neural tube closure. *Cell reports*, *13*(10), 2189–2202.
- Clapham, D. E. (2007). Calcium signaling. *Cell*, *131*(6), 1047–1058.
- COMSOL. (2019). *Comsol multiphysics® v.5.4*. [www.comsol.com](http://www.comsol.com). COMSOL AB, Stockholm, Sweden.

- Cooper, G. M., Hausman, R. E., & Hausman, R. E. (2000). *The cell: a molecular approach* (Vol. 10). ASM press Washington, DC.
- Cruywagen, G., & Murray, J. (1992). On a tissue interaction model for skin pattern formation. *Journal of Nonlinear Science*, *2*(2), 217–240.
- Deguchi, R., Shirakawa, H., Oda, S., Mohri, T., & Miyazaki, S. (2000). Spatiotemporal analysis of  $ca^{2+}$  waves in relation to the sperm entry site and animal–vegetal axis during  $ca^{2+}$  oscillations in fertilized mouse eggs. *Developmental biology*, *218*(2), 299–313.
- De Young, G. W., & Keizer, J. (1992). A single-pool inositol 1, 4, 5-trisphosphate-receptor-based model for agonist-stimulated oscillations in  $ca^{2+}$  concentration. *Proceedings of the National Academy of Sciences*, *89*(20), 9895–9899.
- Dupont, G., Berridge, M., & Goldbeter, A. (1991). Signal-induced  $ca^{2+}$  oscillations: properties of a model based on  $ca^{2+}$ -induced  $ca^{2+}$  release. *Cell calcium*, *12*(2-3), 73–85.
- Dupont, G., Falcke, M., Kirk, V., & Sneyd, J. (2016). *Models of calcium signalling* (Vol. 43). Springer.
- Estrada, J., Andrew, N., Gibson, D., Chang, F., Gnad, F., & Gunawardena, J. (2016). Cellular interrogation: exploiting cell-to-cell variability to discriminate regulatory mechanisms in oscillatory signalling. *PLoS computational biology*, *12*(7), e1004995.
- Falcke, M. (2003). On the role of stochastic channel behavior in intracellular  $ca^{2+}$  dynamics. *Biophysical journal*, *84*(1), 42–56.
- Finch, E. A., Turner, T. J., & Goldin, S. M. (1991). Calcium as a coagonist of inositol 1, 4, 5-trisphosphate-induced calcium release. *Science*, *252*(5004), 443–446.
- Fletcher, A. G., Osterfield, M., Baker, R. E., & Shvartsman, S. Y. (2014). Vertex models of epithelial morphogenesis. *Biophysical journal*, *106*(11), 2291–2304.
- Furuichi, T., Kohda, K., Miyawaki, A., & Mikoshiba, K. (1994). Intracellular channels. *Current opinion in neurobiology*, *4*(3), 294–303.
- Gilkey, J. C., Jaffe, L. F., Ridgway, E. B., & Reynolds, G. T. (1978). A free calcium wave traverses the activating egg of the medaka, *oryzias latipes*. *The Journal of cell biology*, *76*(2), 448–466.
- Girard, S., & Clapham, D. (1993). Acceleration of intracellular calcium waves in xenopus oocytes by calcium influx. *Science*, *260*(5105), 229–232.

- Goldbeter, A., Dupont, G., & Berridge, M. J. (1990). Minimal model for signal-induced  $ca^{2+}$  oscillations and for their frequency encoding through protein phosphorylation. *Proceedings of the National Academy of Sciences*, *87*(4), 1461–1465.
- Hall, R. (2012). Nondimensionalization. URL: <http://wp.auburn.edu/radich/wp-content/uploads/2014/08/Nondimensionalization-Resource-2.pdf>.
- Hamill, O. (2006). Twenty odd years of stretch-sensitive channels. *Pflügers Archiv*, *453*(3), 333–351.
- He, L., Wang, X., Tang, H. L., & Montell, D. J. (2010). Tissue elongation requires oscillating contractions of a basal actomyosin network. *Nature cell biology*, *12*(12), 1133.
- Heilbrunn, L. (1928). The colloid chemistry of protoplasm, protoplasmamonographien i. *Berlin, Gebirder Borntraeger*.
- Herrgen, L., Voss, O. P., & Akerman, C. J. (2014). Calcium-dependent neuroepithelial contractions expel damaged cells from the developing brain. *Developmental cell*, *31*(5), 599–613.
- Hodgkin, A. L., & Huxley, A. F. (1952). A quantitative description of membrane current and its application to conduction and excitation in nerve. *The Journal of physiology*, *117*(4), 500–544.
- Hunter, G. L., Crawford, J. M., Genkins, J. Z., & Kiehart, D. P. (2014). Ion channels contribute to the regulation of cell sheet forces during drosophila dorsal closure. *Development*, *141*(2), 325–334.
- Iino, M., & Endo, M. (1992). Calcium-dependent immediate feedback control of inositol 1, 4, 5-trisphosphate-induced  $ca^{2+}$  release. *Nature*, *360*(6399), 76.
- Kaouri, K., Maini, P. K., Skourides, P., Christodoulou, N., & Chapman, S. J. (2019). A simple mechanochemical model for calcium signalling in embryonic epithelial cells. *Journal of mathematical biology*, *78*(7), 2059–2092.
- Kashir, J., Heindryckx, B., Jones, C., De Sutter, P., Parrington, J., & Coward, K. (2010). Oocyte activation, phospholipase c zeta and human infertility. *Human reproduction update*, *16*(6), 690–703.
- Keener, J., & Sneyd, J. (2009). *Mathematical physiology 1: Cellular physiology*. Springer.

- Kühl, M., Sheldahl, L. C., Malbon, C. C., & Moon, R. T. (2000). Ca<sup>2+</sup>/calmodulin-dependent protein kinase II is stimulated by wnt and frizzled homologs and promotes ventral cell fates in xenopus. *Journal of Biological Chemistry*, *275*(17), 12701–12711.
- Kühl, M., Sheldahl, L. C., Park, M., Miller, J. R., & Moon, R. T. (2000). The wnt/ca<sup>2+</sup> pathway: a new vertebrate wnt signaling pathway takes shape. *Trends in genetics*, *16*(7), 279–283.
- Lam, P. Y., Webb, S. E., Leclerc, C., Moreau, M., & Miller, A. L. (2009). Inhibition of stored ca<sup>2+</sup> release disrupts convergence-related cell movements in the lateral intermediate mesoderm resulting in abnormal positioning and morphology of the pronephric anlagen in intact zebrafish embryos. *Development, growth & differentiation*, *51*(4), 429–442.
- Landau, L., Lifshitz, E., Sykes, J., Reid, W., & Dill, E. H. (1960). Theory of elasticity: Vol. 7 of course of theoretical physics. *Phys. Today*, *13*, 44.
- Lane, Murray, J. D., & Manoranjan, V. (1987). Analysis of wave phenomena in a morphogenetic mechanochemical model and an application to post-fertilization waves on eggs. *Mathematical Medicine and Biology: A Journal of the IMA*, *4*(4), 309–331.
- Lane, M. C., Koehl, M., Wilt, F., & Keller, R. (1993). A role for regulated secretion of apical extracellular matrix during epithelial invagination in the sea urchin. *Development*, *117*(3), 1049–1060.
- Lechleiter, J. D., & Clapham, D. E. (1992). Molecular mechanisms of intracellular calcium excitability in *X. laevis* oocytes. *Cell*, *69*(2), 283–294.
- Lecuit, T., & Lenne, P.-F. (2007). Cell surface mechanics and the control of cell shape, tissue patterns and morphogenesis. *Nature reviews Molecular cell biology*, *8*(8), 633–644.
- Lecuit, T., Lenne, P.-F., & Munro, E. (2011). Force generation, transmission, and integration during cell and tissue morphogenesis. *Annual review of cell and developmental biology*, *27*, 157–184.
- Leung, C. F., Miller, A. L., Korzh, V., Chong, S.-W., Sleptsova-Freidrich, I., & Webb, S. E. (2009). Visualization of stochastic ca<sup>2+</sup> signals in the formed somites during the early segmentation period in intact, normally developing zebrafish embryos. *Development, growth & differentiation*, *51*(7), 617–637.

- Li, Y.-X., & Rinzel, J. (1994). Equations for inositol 3 receptor-mediated  $[Ca^{2+}]_i$  oscillations derived from a detailed kinetic model: a Hodgkin-Huxley like formalism. *Journal of Theoretical Biology*, 166(4), 461–473.
- Luby-Phelps, K. (1999). Cytoarchitecture and physical properties of cytoplasm: volume, viscosity, diffusion, intracellular surface area. In *International review of cytology* (Vol. 192, pp. 189–221). Elsevier.
- Lynch, S. (2004). *Dynamical systems with applications using matlab*. Springer.
- Mak, D.-O. D., McBride, S., & Foskett, J. K. (1998). Inositol 1, 4, 5-tris-phosphate activation of inositol tris-phosphate receptor  $Ca^{2+}$  channel by ligand tuning of  $Ca^{2+}$  inhibition. *Proceedings of the National Academy of Sciences*, 95(26), 15821–15825.
- Markova, O., & Lenne, P.-F. (2012). Calcium signaling in developing embryos: focus on the regulation of cell shape changes and collective movements. In *Seminars in cell & developmental biology* (Vol. 23, pp. 298–307).
- MathWorks. (2020). *Matlab® r2020a*. The MathWorks Inc., Natick, Massachusetts.
- Meyer, T., & Stryer, L. (1988). Molecular model for receptor-stimulated calcium spiking. *Proceedings of the National Academy of Sciences*, 85(14), 5051–5055.
- Miyazaki, S. (2006). Thirty years of calcium signals at fertilization. In *Seminars in cell & developmental biology* (Vol. 17, pp. 233–243).
- Moore, S. W., Roca-Cusachs, P., & Sheetz, M. P. (2010). Stretchy proteins on stretchy substrates: the important elements of integrin-mediated rigidity sensing. *Developmental cell*, 19(2), 194–206.
- Moran, D., & Rice, R. W. (1976). Action of papaverine and ionophore A23187 on neurulation. *Nature*, 261(5560), 497.
- Mouillac, B., Balestre, M.-N., & Guillon, G. (1990). Positive feedback regulation of phospholipase C by vasopressin-induced calcium mobilization in wrk1 cells. *Cellular signalling*, 2(5), 497–507.
- Murray, & Oster. (1984). Generation of biological pattern and form. *Mathematical Medicine and Biology: A Journal of the IMA*, 1(1), 51–75.
- Murray, J. (2001). *Mathematical biology ii: spatial models and biomedical applications*. Springer New York.

- Murray, J. D. (1989). *Mathematical biology, vol. 19 of biomathematics*. Springer, Berlin, Germany.
- Murray, J. D., Maini, P. K., & Tranquillo, R. T. (1988). Mechanochemical models for generating biological pattern and form in development. *Physics Reports*, *171*(2), 59–84.
- Narciso, Contento, N. M., Storey, T. J., Hoelzle, D. J., & Zartman, J. J. (2017). Release of applied mechanical loading stimulates intercellular calcium waves in drosophila wing discs. *Biophysical journal*, *113*(2), 491–501.
- Narciso, C., Wu, Q., Brodskiy, P., Garston, G., Baker, R., Fletcher, A., & Zartman, J. (2015). Patterning of wound-induced intercellular  $ca^{2+}$  flashes in a developing epithelium. *Physical biology*, *12*(5), 056005.
- NIH. (2019). *Spina bifida. genetics home reference*. <https://ghr.nlm.nih.gov/condition/spina-bifida#statistics>. U.S. National Library of Medicine. ([Online; accessed 06-November-2019])
- Nikolopoulou, E., Galea, G. L., Rolo, A., Greene, N. D., & Copp, A. J. (2017). Neural tube closure: cellular, molecular and biomechanical mechanisms. *Development*, *144*(4), 552–566.
- Okuda, S., Inoue, Y., Eiraku, M., Sasai, Y., & Adachi, T. (2013). Apical contractility in growing epithelium supports robust maintenance of smooth curvatures against cell-division-induced mechanical disturbance. *Journal of biomechanics*, *46*(10), 1705–1713.
- Oster, G., & Odell, G. (1984). The mechanochemistry of cytogels. *Physica D: Nonlinear Phenomena*, *12*(1-3), 333–350.
- Parker, I., & Ivorra, I. (1990). Inhibition by  $ca^{2+}$  of inositol trisphosphate-mediated  $ca^{2+}$  liberation: a possible mechanism for oscillatory release of  $ca^{2+}$ . *Proceedings of the National Academy of Sciences*, *87*(1), 260–264.
- Parker, I., & Yao, Y. (1991). Regenerative release of calcium from functionally discrete subcellular stores by inositol trisphosphate. *Proceedings of the Royal Society of London. Series B: Biological Sciences*, *246*(1317), 269–274.
- Parys, J. B., Sernett, S. W., DeLisle, S., Snyder, P. M., Welsh, M. J., & Campbell, K. P. (1992). Isolation, characterization, and localization of the inositol 1, 4, 5-trisphosphate receptor protein in xenopus laevis oocytes. *Journal of Biological Chemistry*, *267*(26), 18776–18782.

- Piechór, K. (2013). Calcium waves in thin visco-elastic cells. *Mathematical Modelling of Natural Phenomena*, 8(3), 206–226.
- Popgeorgiev, N., Bonneau, B., Ferri, K. F., Prudent, J., Thibaut, J., & Gillet, G. (2011). The apoptotic regulator nrz controls cytoskeletal dynamics via the regulation of ca<sup>2+</sup> trafficking in the zebrafish blastula. *Developmental cell*, 20(5), 663–676.
- Qi, L., Li, N., Huang, R., Song, Q., Wang, L., Zhang, Q., ... Cheng, G. (2013). The effects of topographical patterns and sizes on neural stem cell behavior. *PLoS One*, 8(3), e59022.
- Reed, P. W., & Lardy, H. A. (1972). A23187: a divalent cation ionophore. *Journal of Biological Chemistry*, 247(21), 6970–6977.
- Rohrschneider, M. R., & Nance, J. (2009). Polarity and cell fate specification in the control of caenorhabditis elegans gastrulation. *Developmental Dynamics*, 238(4), 789–796.
- Sahu, S. U., Visetsouk, M. R., Garde, R. J., Hennes, L., Kwas, C., & Gutzman, J. H. (2017). Calcium signals drive cell shape changes during zebrafish midbrain–hindbrain boundary formation. *Molecular biology of the cell*, 28(7), 875–882.
- Sanderson, M., & Sleight, M. (1981). Ciliary activity of cultured rabbit tracheal epithelium: beat pattern and metachrony. *Journal of Cell Science*, 47(1), 331–347.
- Sanderson, M. J., Charles, A., & Dirksen, E. R. (1990). Mechanical stimulation and intercellular communication increases intracellular ca<sup>2+</sup> in epithelial cells. *Cell regulation*, 1(8), 585–596.
- Sanderson, M. J., Chow, I., & Dirksen, E. R. (1988). Intercellular communication between ciliated cells in culture. *American Journal of Physiology-Cell Physiology*, 254(1), C63–C74.
- Sawyer, J. M., Harrell, J. R., Shemer, G., Sullivan-Brown, J., Roh-Johnson, M., & Goldstein, B. (2010). Apical constriction: a cell shape change that can drive morphogenesis. *Developmental biology*, 341(1), 5–19.
- Scholey, J., Taylor, K., & Kendrick-Jones, J. (1980). Regulation of non-muscle myosin assembly by calmodulin-dependent light chain kinase. *Nature*, 287(5779), 233.
- Slusarski, D. C., Corces, V. G., & Moon, R. T. (1997). Interaction of wnt and a frizzled homologue triggers g-protein-linked phosphatidylinositol signalling. *Nature*, 390(6658), 410.

- Slusarski, D. C., Yang-Snyder, J., Busa, W. B., & Moon, R. T. (1997). Modulation of embryonic intracellular  $ca^{2+}$  signaling by wnt-5a. *Developmental biology*, *182*(1), 114–120.
- Smrcka, A. V., Brown, K., Sternweis, P., et al. (1991). Regulation of polyphosphoinositide-specific phospholipase c activity by purified gq. *Science*, *251*(4995), 804–807.
- Sneyd, J. (2007). Models of calcium dynamics. *Scholarpedia*, *2*(3), 1576. (revision #137198) doi: 10.4249/scholarpedia.1576
- Sneyd, J., LeBeau, A., & Yule, D. (2000). Traveling waves of calcium in pancreatic acinar cells: model construction and bifurcation analysis. *Physica D: Nonlinear Phenomena*, *145*(1-2), 158–179.
- Sneyd, J., Tsaneva-Atanasova, K., Reznikov, V., Bai, Y., Sanderson, M., & Yule, D. (2006). A method for determining the dependence of calcium oscillations on inositol trisphosphate oscillations. *Proceedings of the National Academy of Sciences*, *103*(6), 1675–1680.
- Steinhardt, R. A., & Epel, D. (1974). Activation of sea-urchin eggs by a calcium ionophore. *Proceedings of the National Academy of Sciences*, *71*(5), 1915–1919.
- Steinhardt, R. A., Epel, D., Jun, E. J. C., & Yanagimachi, R. (1974). Is calcium ionophore a universal activator for unfertilised eggs? *Nature*, *252*(5478), 41.
- Stricker, S. A. (1999). Comparative biology of calcium signaling during fertilization and egg activation in animals. *Developmental biology*, *211*(2), 157–176.
- Suzuki, M., Sato, M., Koyama, H., Hara, Y., Hayashi, K., Yasue, N., . . . others (2017). Distinct intracellular  $ca^{2+}$  dynamics regulate apical constriction and differentially contribute to neural tube closure. *Development*, *144*(7), 1307–1316.
- Swann, K., & Ozil, J.-P. (1994). Dynamics of the calcium signal that triggers mammalian egg activation. In *International review of cytology* (Vol. 152, pp. 183–222). Elsevier.
- Takano, K., Obata, S., Komazaki, S., Masumoto, M., Oinuma, T., Ito, Y., . . . Asashima, M. (2011). Development of  $ca^{2+}$  signaling mechanisms and cell motility in presumptive ectodermal cells during amphibian gastrulation. *Development, growth & differentiation*, *53*(1), 37–47.
- Taylor, S. J., & Exton, J. H. (1987). Guanine-nucleotide and hormone regulation of polyphosphoinositide phospholipase c activity of rat liver plasma membranes. bivalent-cation and phospholipid requirements. *Biochemical Journal*, *248*(3), 791–799.

- Tsutsumi, M., Inoue, K., Denda, S., Ikeyama, K., Goto, M., & Denda, M. (2009). Mechanical-stimulation-evoked calcium waves in proliferating and differentiated human keratinocytes. *Cell and tissue research*, *338*(1), 99.
- Vijayraghavan, D. S., & Davidson, L. A. (2017). Mechanics of neurulation: From classical to current perspectives on the physical mechanics that shape, fold, and form the neural tube. *Birth defects research*, *109*(2), 153–168.
- Von Dassow, M., Strother, J. A., & Davidson, L. A. (2010). Surprisingly simple mechanical behavior of a complex embryonic tissue. *PLoS One*, *5*(12).
- Wallingford, J. B., Ewald, A. J., Harland, R. M., & Fraser, S. E. (2001). Calcium signaling during convergent extension in xenopus. *Current Biology*, *11*(9), 652–661.
- Watras, J., Ehrlich, B. E., et al. (1991). Bell-shaped calcium-response curves of  $I_{\text{ns}}$  (1, 4, 5) p 3-and calcium-gated channels from endoplasmic reticulum of cerebellum. *Nature*, *351*(6329), 751–754.
- Webb, S. E., & Miller, A. L. (2007).  $\text{Ca}^{2+}$  signalling and early embryonic patterning during zebrafish development. *Clinical and experimental pharmacology and physiology*, *34*(9), 897–904.
- Wilkins, M., & Sneyd, J. (1998). Intercellular spiral waves of calcium. *Journal of theoretical biology*, *191*(3), 299–308.
- Yang, W., Chen, J.-Y., & Zhou, L. (2009). Effects of shear stress on intracellular calcium change and histamine release in rat basophilic leukemia (rbl-2h3) cells. *Journal of Environmental Pathology, Toxicology and Oncology*, *28*(3).
- Young, S., Ennes, H., McRoberts, J., Chaban, V., Dea, S., & Mayer, E. (1999). Calcium waves in colonic myocytes produced by mechanical and receptor-mediated stimulation. *American Journal of Physiology-Gastrointestinal and Liver Physiology*, *276*(5), G1204–G1212.
- Zhang, J., Webb, S. E., Ma, L. H., Chan, C. M., & Miller, A. L. (2011). Necessary role for intracellular  $\text{Ca}^{2+}$  transients in initiating the apical-basolateral thinning of enveloping layer cells during the early blastula period of zebrafish development. *Development, growth & differentiation*, *53*(5), 679–696.

Zhou, J., Kim, H. Y., & Davidson, L. A. (2009). Actomyosin stiffens the vertebrate embryo during crucial stages of elongation and neural tube closure. *Development*, 136(4), 677–688.

# Appendix A1

## Model parameters

Parameter values	
Parameter	Value
$b$	0.111
$k_1$	$0.7\mu M$
$k_f$	$16.2\mu M/s$
$k_\mu$	$0.7\mu M$
$\gamma$	$2\mu M/s$
$k_\gamma$	$0.1\mu M$
$\beta$	$0 - 0.02\mu M/s$
$k_2$	$0.7\mu M$
$\tau_h$	$2s$
$D_c$	$20(\mu m)^2/s$

Table A1.1: Parameter values for the dimensional Atri model. Source: Atri et al. (1993)

# Appendix A2

## MATLAB codes

Listing A2.1: Atri Model without Diffusion

```
1 % ----- ATRI MODEL -----
2
3 [t CH] = ode45(@atri,[0 50], [1 1]);
4 c = CH(:,1);
5 h = CH(:,2);
6
7 figure(1)
8 plot(t,c);
9 hold on; grid on;
10 %title('Atri Model: c(t) and h(t)');
11 xlabel('\it t')
12 plot(t,h,'--');
13 legend('\it c : Ca^{2+} concentration', '\it h : Fraction of active ...
        IPRs');
14 hold off;
15
16 function A = atri(t,ch)
17
18 kf = 16.2;
19 th = 2;
20 k1 = 0.7;
21 y = 2;
22 ky = 0.1;
23 k2 = 0.7;
24 b = 0.111;
25
```

```

26 mu = 0.3;
27 K1 = (kf*th)/k1;
28 T = (y*th)/k1;
29 K = ky/k1;
30 K2 = k2/k1;
31
32 Fch = ((b+ch(1))*mu*K1*ch(2)/(1+ch(1)))-(T*ch(1)/(K+ch(1)));
33 Gch = (K2^2/(K2^2+ch(1)^2))-ch(2);
34
35 A = [Fch; Gch];
36
37 end

```

Code used to generate the plots in Chapter 2.

#### Listing A2.2: Mechanochemical Model without Diffusion

```

1  % ----- MECHANOCHEMICAL ODE MODEL -----
2
3  [t CHO] = ode45(@atri,[0 50], [1 1 1]);
4  c = CHO(:,1);
5  h = CHO(:,2);
6  o = CHO(:,3);
7
8  set(0, 'DefaultFigureRenderer', 'painters');
9
10 figure(1)
11 set(gcf, 'DefaultAxesFontSize', 16);
12 plot(t, c);
13 hold on; grid on;
14 % title('Mechanochemical Model: {\it c}, {\it h} and \theta');
15 xlabel('\it t', 'FontSize', 18);
16 plot(t, h, '--');
17 plot(t, o, '-.m', 'LineWidth', 1);
18 lgd = legend('\it c : Ca^{2+} concentration', '\it h : Fraction of ...
           active IPRs', '\theta : Tissue dilation');
19 set(lgd, 'FontSize', 16);
20 hold off;
21
22 function A = atri(t, ch)
23
24 kf = 16.2;
25 th = 2;

```

```

26 k1 = 0.7;
27 y = 2;
28 ky = 0.1;
29 k2 = 0.7;
30 b = 0.111;
31 ko = 1;
32
33 lm = 0.5;
34 mu = 0.3;
35
36 K1 = (kf*th)/k1;
37 T = (y*th)/k1;
38 K = ky/k1;
39 K2 = k2/k1;
40
41 M = 0.2;
42 n = 4; % only for even n
43 W = 2;
44 rs = (ch(1)^n/(M^n+ch(1)^n));
45 de = 1-((ch(1)-W)^n/(M^n+(ch(1)-W)^n))*heaviside(-(ch(1)-W));
46 pl = rs - de ;
47
48 Fch = ((b+ch(1))*mu*K1*ch(2)/(1+ch(1)))-(T*ch(1)/(K+ch(1)))+lm*ch(3);
49 Gch = (K2^2/(K2^2+ch(1)^2))-ch(2);
50 Och = -ko*ch(3)+pl;
51
52 A = [Fch; Gch; Och];
53
54 end

```

Code used to generate the plots in Chapter 4.

The code above simulates the model for the traction term  $\hat{T}(c) = T_1(W, c)$  (see Equation (4.10)).

Listing A2.3: Mechanochemical Model with Diffusion

```

1 %-----
2 % --- MECHANOCHEMICAL PDE MODEL ---
3 %-----
4
5 m = 0;
6 x = linspace(-25,25,5000);
7 t = linspace(0,50,500);

```

```

8
9 mu_lm;
10
11 sol = pdepe(m,@atripde,@atriic,@atribc,x,t);
12 u1 = sol(:,:,1);
13 u2 = sol(:,:,2);
14 u3 = sol(:,:,3);
15
16 set(0, 'DefaultFigureRenderer', 'painters');
17
18 figure(1);
19 set(gcf, 'DefaultAxesFontSize', 16);
20 imagesc(x,t,u1); colormap jet; axis xy;
21 colorbar
22 caxis([0 5]);
23 xlabel('\it x', 'FontSize', 18);
24 ylabel('\it t', 'FontSize', 18);
25
26 figure(2);
27 set(gcf, 'DefaultAxesFontSize', 16);
28 pcolor(x,t,u3); colormap autumn; shading interp;
29 colorbar
30 caxis([0 1]);
31 xlabel('\it x', 'FontSize', 18);
32 ylabel('\it t', 'FontSize', 18);
33
34 %% -----LINE GRAPHS-----
35
36 figure(3);
37 set(gcf, 'DefaultAxesFontSize', 16);
38 plot(x,u1(500,:), 'LineWidth', 1);
39 hold on; grid on;
40 plot(x,u3(500,:), 'm', 'LineWidth', 1);
41 xlabel('\it x', 'FontSize', 18);
42 lgd = legend('{\it c}', ' \theta');
43 set(lgd, 'FontSize', 16, 'LineWidth', 1);
44 axis([-25 25 0 6]);
45 hold off;
46
47 figure(4);
48 set(gcf, 'DefaultAxesFontSize', 16);
49 plot(t,u1(:,2500), 'LineWidth', 1);
50 hold on; grid on;

```

```

51 plot(t,u3(:,2500),'m','LineWidth',1);
52 xlabel('\it t','FontSize',18);
53 lgd = legend('{\it c}',' \theta');
54 set(lgd,'FontSize',16,'LineWidth',1);
55 axis([0 50 0 6]);
56 hold off;
57
58 %% -----
59
60 function P = mu_lm()
61
62 global mu;
63 global lm;
64 global W;
65 global cSt;
66 global hSt;
67 global oSt;
68
69 mu = 0.3;
70 lm = 0.5;
71 W = 1.5;
72
73 R = AtriMechSteadyStateSolver_Vex(mu,lm,W)
74
75 cSt = R(1);
76 hSt = R(2);
77 oSt = R(3);
78
79 end
80
81 function [c, f, s] = atripde(x,t,u,dudx)
82
83 kf = 16.2;
84 th = 2;
85 k1 = 0.7;
86 y = 2;
87 ky = 0.1;
88 k2 = 0.7;
89 b = 0.111;
90 ko = 1;
91 Dc = 20*(10^-12);
92 l = 20*(10^-6);
93

```

```

94 % declaring global parameters within function
95 %-----
96 global mu;
97 global lm;
98 global W;
99 %-----
100
101 K1 = (kf*th)/k1;
102 T = (y*th)/k1;
103 K = ky/k1;
104 K2 = k2/k1;
105 D = Dc*th/l^2;
106
107
108 M = 0.2;
109 n = 4; % only for even n
110 rs = (u(1)^n/(M^n+u(1)^n));
111 de = 1-((u(1)-W)^n/(M^n+(u(1)-W)^n))*heaviside(-(u(1)-W));
112 pl = rs - de ;
113 TH = pl;
114
115 F = ((b+u(1))*mu*K1*u(2)/(1+u(1)))-(T*u(1)/(K+u(1)))+lm*u(3);
116 G = (K2^2/(K2^2+u(1)^2))-u(2);
117 O = -ko*u(3)+TH;
118
119 c = [1; 1; 1];
120 f = [D; 0; 0] .* dudx;
121 s = [F; G; O];
122
123 end
124
125 function u0 = atriic(x)
126
127 % declaring global parameters within function
128 %-----
129 global cSt;
130 global hSt;
131 global oSt;
132 %-----
133
134 S = 10;
135 sig = 0.01;
136

```

```

137 u0 = [ cSt+4*exp(-0.5*(x^2)/(S*sig)^2); hSt; oSt];
138
139 end
140
141 function [pl,ql,pr,qr] = atribc(xl,ul,xr,ur,t)
142
143 % declaring global parameters within function
144 %-----
145 global cSt;
146 global hSt;
147 global oSt;
148 %-----
149
150 % NO FLUX CONDITION
151 pl = [0; 0; 0];
152 ql = [1; 1; 1];
153 pr = [0; 0; 0];
154 qr = [1; 1; 1];
155
156 end

```

Code used to generate the plots in Chapter 5.

The code above simulates the model for the traction term  $\hat{T}(c) = T_1(W, c)$ .

Listing A2.4: Finding the steady state values of the mechanochemical model

```

1 % --- MECHANOCHEMICAL PDE MODEL: STEADY STATE (IC) ---
2
3 function R = AtriMechSteadyStateSolver.Vex(mu, lm, W)
4
5 kf = 16.2;
6 th = 2;
7 k1 = 0.7;
8 y = 2;
9 ky = 0.1;
10 k2 = 0.7;
11 b = 0.111;
12
13 K1 = (kf*th)/k1;
14 T = (y*th)/k1;
15 K = ky/k1;
16
17 syms c h TH(c)

```

```

18
19 deg = 5;
20
21 syms rs(c) de(c) pl(c)
22
23 M = 0.2;
24 n = 4; % only for even n
25
26 rs(c) = (c^n/(M^n+c^n));
27 de(c) = 1-(c^n/(M^n+c^n))*heaviside(-c);
28 pl(c) = rs(c) - de(c-W) ;
29
30 TH(c) = pl(c);
31
32 %-----
33
34 digits(16);
35 eqnC = mu*K1*(1/(1+c^2))*(b+c)/(1+c)-(T*c/(K+c))+lm*TH == 0;
36 solC = vpasolve(eqnC, c, 1)
37
38 % THE FOLLOWING CODE RETURNS ONLY ONE REAL ROOT
39 %% --- Root Selector ---
40
41 rt = zeros([1 deg]);
42 ct = 0;
43 pv = 0;
44 rn = size(solC,1);
45
46 for j=1:rn
47     z = double(solC(j));
48     REC = log10(abs(real(z)));
49     IMC = log10(abs(imag(z)));
50
51     if (isreal(z))
52         if(z ≥ 0)
53             ct = ct + 1;
54             rt(ct) = z;
55             if (ct == 1)
56                 pv = j;
57             end
58         end
59
60     elseif (real(z) > 0)

```

```

61     if((REC-IMC) > 3)
62         ct = ct + 1;
63         rt(ct) = real(z);
64         if (ct == 1)
65             pv = j;
66         end
67     end
68 end
69
70 end
71
72 R(1) = vpa(rt(1),16);
73 R(2) = 1/(1+R(1)^2);
74 R(3) = TH(R(1))/1;
75
76 if (ct == 0)
77     Out = "No suitable real roots"
78     R(1) = 0;
79     R(2) = 0;
80     R(3) = 0;
81 else
82     Out = "Real root extracted"
83 end
84
85 end

```

Code used to compute the steady state values of  $c$ ,  $h$  &  $\theta$ , which are then used to set the initial conditions for the mechanochemical PDE model.

For traction term  $\hat{T}(c) = T_1(W, c)$ .